Universität Zürich[UZH]

Geographisches Institut

A century of large rock slope failures in the European Alps: Influencing factors & climate change effects

GEO 511 Master's Thesis

Author: Dominik Metzger, 19-742-485

Supervised by: Prof. Dr. Christian Huggel

Faculty representative: Prof. Dr. Christian Huggel

16.03.2026

Abstract

Large rock slope failures represent significant geomorphological processes and natural hazards in the European Alps. Their occurrence is controlled by a combination of geological, topographic, and environmental factors, many of which are currently undergoing rapid change due to climate warming. This thesis investigates the spatial and temporal distribution of large rock slope failures ($>10^5$ m^3) across the European Alps and evaluates the relative influence of topography, lithology, cryospheric processes, and climatic variables on their occurrence. To address these objectives, an updated Alps-wide inventory of large rock slope failures since 1925 was compiled by integrating previously published datasets with newly identified events. The inventory was combined with regional datasets on elevation, slope angle, aspect, lithology, glacier extent, permafrost distribution, air temperature, freeze–thaw cycles, and precipitation. Frequency distribution and spatial overlays were used to identify patterns in the environmental conditions associated with failure locations. The results show that large rock slope failures predominantly occur in steep, high-elevation terrain where geological structure and topographic relief create predisposing conditions for instability. Many failures occur in recently deglaciated areas or within zones of probable permafrost occurrence, indicating that cryospheric processes play an important conditioning role. In addition, climatic variables such as temperature patterns, freeze-thaw activity, and precipitation appear to act as potential triggers or contributing factors that may influence the timing of failures. By expanding the existing inventory and analyzing large-scale environmental controls, this study contributes to a better understanding of rock slope failure processes in a changing mountain environment and provides a basis for future research and hazard assessment.

Contents

1 Introduction

Slope failures in mountainous areas present a serious hazard, especially in densely populated regions like the European Alps, where alpine landscapes play a crucial role in daily life (Huggel et al., 2012). Rock slope failures shape mountain morphology while posing persistent threats to infrastructure and settlements. Large-volume failures (>10^5 m^3) are of particular concern because they can trigger secondary debris flows that amplify downstream hazards, particularly as human activities increasingly encroach on mountain valleys (Fischer et al., 2012; Michoud et al., 2012; McColl, 2012).

In recent decades, rock slope instabilities in alpine environments have attracted growing scientific and public attention, driven by observations of increasing event frequency and their potential linkage to rapid environmental change (Huggel et al., 2012; Fischer et al., 2012; Knoflach et al., 2021). High-profile failures such as those at Pizzo Cengalo (Walter et al., 2020), Piz Scerscen (Pierhöfer et al., 2024), or very recently Kleines Nesthorn/Blatten (Lambiel et al., 2025) illustrate the scale and consequence of these processes, with volumes frequently surpassing 1 million cubic meters and runouts extending deep into inhabited valleys. While static factors like lithology, topography, and discontinuity orientation establish baseline susceptibility (Fischer & Huggel, 2008; Stoffel et al., 2014), dynamic cryospheric changes, such as glacial debuttressing, permafrost thaw, and shifting freeze-thaw regimes, appear to accelerate destabilization in preconditioned slopes (Kenner et al., 2021; McColl, 2012; Haeberli & Beniston, 1998; Knoflach et al., 2021).

In this context, spatially and temporally explicit inventories of large rock slope failures provide a crucial basis for understanding how predisposing factors and environmental forcings interact (Fischer et al., 2012). Detachment zones and associated attributes, such as elevation, aspect, lithology and cryospheric setting, can be used as proxies to identify preferential conditions for failure and to separate relatively static controls (e.g. geology, long-term topography) from more rapidly evolving drivers (e.g. glacier coverage, permafrost state, temperature trends) (Fischer et al., 2012; Stoffel et al., 2014). Such inventories therefore not only support analysis of slope processes but also inform hazard assessment, land-use planning and risk management in mountain regions.

Fischer et al. (2012) provided the most comprehensive analysis to date, documenting over 50 rock slope failures across the Alps through 2007. Their work demonstrated that ∼40-50% of events occurred in recently deglaciated terrain and highlighted elevation banding tied to the historical permafrost limit. However, the study faced inherent limitations: its temporal scope ended before the most recent acceleration of glacier mass loss (∼15% area reduction since 2003; Paul et al., 2020), the sample size constrained robust statistical inference, the focus on the central Alps left adjacent regions underrepresented, and their volume threshold included failure down to 10^3 m^3.

Subsequent work has addressed aspects of these issues, but often in a fragmented way. Several regional studies investigated rock slope failures in specific massifs or valleys, such as the Mont Blanc Massif (Ravanel et al., 2010) or the Dolomites (Bonometti et al., 2026). Others examined rock slope failures over limited time periods (Paranunzio et al., 2016) or focused on small to medium-sized events (Fey et al., 2025). As a result there is still no consistent, Alps-wide inventory that (i) covers the full mountain chain, (ii) focuses specifically on large rock slope failures, and (iii) extends into the most recent decades of rapid climatic and cryospheric change. This gap limits our ability to detect large-scale spatial patterns, to assess long-term temporal trends, and to robustly quantify how static and dynamic controls combine to produce large failures.

At the same time, climate and cryosphere research points to continued and accelerating environmental change in the Alps region. Mean air temperatures have risen markedly since the late 19th century, with a pronounced warming signal since the 1980s (Gobiet et al., 2014; Auer et al., 2007). Glacier area and volume have decreased dramatically, with about half of the glacier area lost since the Little Ice Age maximum and a substantial share of this shrinkage occurring in recent decades (Zemp et al., 2015; Paul et al., 2020). Permafrost monitoring shows widespread warming, deepening active layers and shifts in permafrost distribution towards higher elevations (Haeberli & Beniston, 1998; Haberkorn et al., 2021; Kenner et al., 2021). Projections consistently indicate further warming of 1-4 °C in the 21st century, accompanied by changes in precipitation intensity and snow cover, implying continued glacier retreat and permafrost degradation (Gobiet et al., 2014; MeteoSwiss & ETH Zurich, 2025b). Against this backdrop, updated inventories of large rock slope failures are essential for evaluating whether observed and projected environmental changes are reflected in the frequency, spatial distribution and timing of such events.

This thesis addresses these gaps by developing an expanded, Alps-wide inventory of large rock slope failures ($>10^5$ m^3) spanning from 1925 to the present. The study focuses exclusively on large-volume events to minimize historical reporting bias and capture failures with highest hazard potential. By incorporating post-2007 events and previously undocumented cases, it enables analysis of three core questions: (i) How has the frequency and spatial distribution of large failures evolved over the past century, particularly in recent decades? (ii) How do topographic (elevation, slope angle, aspect) and geological (lithology, faults/fractures) factors control the likelihood and magnitude of large rock slope failures? (iii) What signatures of climate-driven processes (glacial retreat, permafrost degradation, freeze-thaw cycles, temperature extremes, precipitation events) emerge in failure timing and environmental context? Finally, the work evaluates how inventory expansion enhances statistical robustness for trend detection compared to prior datasets, providing implications for hazard assessment under 21st-century climate scenarios. These analyses distinguish persistent geological controls from emerging climatic signals, establishing an updated foundation for rock slope stability research in a warming Alpine environment.

2 Background

2.1 Topography

Elevation influences slope stability mainly through its role as a proxy for other environmental variables, such as permafrost occurrence, glacier coverage, or snow cover. In the Alps, large rock slope failures cluster between approximately 2600-3400 m a.s.l., coinciding with the lower limit of permafrost and the elevation range where alpine glaciers are most dynamic (Kenner et al., 2021; Fischer et al., 2012; Noetzli et al., 2003). At the highest elevations (>4000 m a.s.l.), large failures become rare despite the presence of steep slopes, mainly due to the dominance of glacier cover. Frost cracking intensity shows a non-monotonic relationship with elevation, peaking around 3000 m a.s.l. Higher up it decreases again, due to lack of liquid water (Draebing et al., 2022).
Steep slopes are associated with higher instability and failure potential, as increased slope angle raises shear stress along failure planes and promotes planar and wedge failures (McColl, 2012). As a result, slopes exceeding a critical threshold angle are far more prone to large failures. Studies indicate that the majority of documented rock slope failures occur on slopes steeper than approximately 30-35°, with maximum frequency in the 40-60° range (Fischer et al., 2012; Noetzli et al., 2003). This threshold effect reflects the fundamental mechanics of slope stability: at steep angles, the driving gravitational force exceeds the frictional and cohesive resistance along potential failure planes, even without additional environmental triggers.
Slope aspect modulates the effects of solar radiation and thus controls ground and near-surface rock temperatures. North-facing slopes are therefore characteristically colder, maintain permafrost at lower elevations, and sustain snow cover longer, promoting freeze-thaw weathering and limiting water infiltration. South-facing slopes on the other hand experience larger diurnal and seasonal temperature cycles, enhanced thermal stress, and more rapid snow melt (Boeckli et al., 2012a; Phillips et al., 2017b). Laboratory experiments demonstrate higher frost cracking efficacy on colder north-facing slopes compared to warmer south-facing exposures, with highest efficacy between -9 and -7°C (Draebing & Krautblatter, 2019; Mayer et al., 2023). While many frost cracking models indicate that frost weathering is highest on south-facing slopes, in situ measurements reveal the contrary. This likely results from overestimation of rock moisture availability (Draebing & Mayer, 2021a).
Topographic characteristics change only slowly on human timescales, barring large failures themselves, so changes in failure patterns cannot be attributed to topographic change. However, climate-driven shifts in permafrost distribution, snow cover, and glacier extent will effectively alter which elevations and aspects experience the most intense weakening processes (Kenner et al., 2021; Hugonnet et al,. 2021). Topographic factors mainly serve as proxies for other processes, such as elevation as a frost cracking proxy or slope angle as a shear stress proxy.

2.2 Lithology

Lithology and geological structure are fundamental controls that condition rock slope stability in alpine environments. The stability of a rock mass is largely determined by the type and composition of the rock, its internal structure and layering, and the orientation of these layers relative to the slope face (Gruner et al., 2018; Fischer & Huggel, 2008). Failures commonly occur along pre-existing discontinuity systems such as joints, bedding planes, and fractures that control the mechanical behaviour of the slope (Stoffel et al., 2014; Stead & Wolter, 2015). In this sense, lithology and geological structure act primarily as predisposing factors that define the long-term susceptibility of a rock slope (Fischer & Huggel, 2008; Stoffel et al., 2014). Across the European Alps, these factors create spatially heterogeneous hazard patterns tied to distinct tectonic domains, with ongoing climate change poised to redistribute instability zones without altering the underlying geological framework (Fischer et al., 2012; Stoffel et al., 2014).

Tectonic preconditioning further contributes to slope instability. Ancient faults, fracture zones, and shear surfaces formed during mountain-building phases can significantly reduce rock mass strength. These structures often become prone to failure when combined with long-term processes such as glacial unloading, erosion, and stress release associated with valley deepening or glacier retreat (Gruner et al., 2018; McColl, 2012). In formerly glaciated Alpine valleys, this tectonic inheritance is amplified by glacial oversteepening and debuttressing, so that large rock slopes often evolve towards failure through a long phase of progressive fracture propagation and strength loss rather than by a single catastrophic trigger (Oswald et al., 2021; McColl, 2012). As rock bridges progressively break and shear strength declines, slope stability decreases until a critical threshold is reached, allowing failure to occur even without an immediate external trigger (Gruner et al., 2018).

Some rock types are inherently weaker/more fractured and fail more readily. However, even within the same lithology, stability varies due to stress history, slope height, and orientation. Lithology sets the background susceptibility, but local conditions trigger and shape failures (Blondeau et al., 2021). Regional inventories suggest that while lithology clearly constrains the typical failure volume and mechanism, the overall occurrence of rock slope failures is more strongly governed by topography and cryospheric condition than by rock type alone (Fischer et al., 2012).

Some analyses of large rock slope failures (>1000k m^3) in the European Alps at all elevations show that approximately two-thirds have occurred in sedimentary rocks (particularly limestone and dolomite), while about one-third involve crystalline lithologies, such as gneiss and granite. In contrast, large-scale failures in schist are relatively rare (Gruner, 2006). More recent inventories suggest that a majority of high-elevation large rock slope failures occur in crystalline lithologies (Fischer et al., 2012; Paranunzio et al., 2016).

The lithological composition of steep rock walls continues to evolve as glaciers erode, retreat, and expose new bedrock, and these newly deglaciated terrains begin to record post-glacial erosion almost immediately (Elkadi et al., 2022). Detailed erosion measurements in recently deglaciated rockwalls indicate that paraglacial, frost-cracking and permafrost degradation processes jointly drive high initial erosion rates, particularly in high-elevation walls affected by bedrock permafrost (Draebing et al., 2022). Since the Late Quaternary, high-elevation, glacier-proximal regions have increasingly revealed crystalline lithologies such as granite, diorite, and gneiss, while lower-elevation zones remain dominated by sedimentary formations (Fischer et al., 2012).

Looking forward, continued glacier retreat will expose additional steep rock faces in crystalline terrain (Paul et al., 2020; Hugonnet et al., 2021). Although the inherent strength properties of these rocks remain largely constant, their exposure to degradation processes, such as permafrost thaw, freeze-thaw cycling, and water infiltration, will increase under a warming climate, as the cryosphere shrinks. Observations and models predict increased rockfall and small-to-medium failure activity from these enhanced degradation processes (Kenner et al., 2021; Hartmeyer et al., 2020).

2.3 Cryosphere

2.3.1 Glaciers

Glaciers strongly influence slope stability in alpine environments through three primary mechanisms: (1) eroding and oversteepening valley walls, (2) modifying stress field through ice loading and unloading, and (3) controlling thermal/hydrological boundary conditions at rock surfaces (Kenner et al., 2021; McColl, 2012).
Glacial oversteepening weakens slope bases through erosion, increasing shear/self-weight stresses that initiate instabilities, including rockfall (Kenner et al., 2021). However, rock mass strength often prevents immediate failure, making oversteepening primarily a preparatory factor that requires additional weakening processes, such as frost cracking or hydro-mechanical weakening, before large failures occur (McColl, 2012). Glacier retreat and glacial debuttressing are also frequently linked to slope failure, but mechanical analyses indicate that glaciers provide only limited structural support because of the ductile behaviour of ice (Grämiger et al., 2017). Instead, stress redistribution from glacial rebound and basal erosion appears more influential for long-term rock slope damage (Kenner et al., 2021; Grämiger et al., 2017). Numerical simulations show that mechanical loading and unloading by ice alone produces relatively little new damage and rarely generates new joints, whereas glacial erosion at the slope foot substantially increases rock mass damage and can induce joints through high horizontal stresses (Grämiger et al., 2017; McColl, 2012). Thermo- and hydromechanical processes associated with glacier retreat, such as thermal expansion of bedrock, first-time exposure to annual temperature cycles, and changes in groundwater regimes, also promote fracture propagation and help prepare slopes for failure (Grämiger et al., 2017; Haeberli & Beniston, 1998). Ice aprons, thin ice bodies frozen to steep bedrock (∼45-60°), represent another glacier-related landform that strongly modifies near-surface thermal and hydrological conditions. Although they exert little influence on mean annual rock temperatures, they damp temperature amplitudes and effectively insulate the rock surface from water infiltration. Their degradation is expected to trigger enhanced freeze–thaw cycling and infiltration into previously protected bedrock, thereby decreasing rock slope stability (Kenner et al., 2021; Hasler et al., 2012; Phillips et al., 2017a).
Contemporary glacier retreat has intensified many of these processes. Deglaciation exposes steep rockwalls to “paraglacial thermal shock” as they transition from near ∼0 °C conditions beneath temperate ice to daily and seasonal temperature cycles, inducing thermo-mechanical stresses and new active layers that drive rapid, shallow damage (Grämiger et al., 2017; Kenner et al., 2021). Detailed monitoring of steep glacier-proximal rock faces indicates that many rockfalls detach from within the zone immediately above current glacier surfaces, consistent with an immediate paraglacial response of deglaciating headwalls to ice loss (Kenner et al., 2021; Hartmeyer et al., 2020). Debuttressing plays only a minor direct role, and the observed rockfall activity near retreating glacier margins is better explained by frost weathering, thermal strain, and hydrological changes in the newly exposed rock (Grämiger et al., 2017; McColl, 2012). Glacier retreat also affects sediment slopes and moraine ridges, where loss of ice support, changes in pore-water pressures, and the breakdown of suction can trigger slides and debris flows, adding to the spectrum of paraglacial mass movements (McColl, 2012; Kenner et al., 2021). In high-alpine faces formerly protected by long-lived ice aprons, recent ice loss has been followed by marked increases in rockfall rates, as newly exposed rock experiences water infiltration and freeze–thaw for the first time in millennia (Kenner et al., 2021; Phillips et al., 2017a). Overall, modern glacier changes act less as a single trigger and more as a set of

boundary-condition shifts (thermal, hydraulic, mechanical) that accelerate ongoing damage in already predisposed rock masses (McColl, 2012; Grämiger et al., 2017; Kenner et al., 2021).
Across the Alps, glaciers have lost approximately 50% of their area since the Little Ice Age maximum (∼1850), with ∼1900 glaciers disappearing entirely and volume reduced by ∼60-65% from ∼280 km^3 to ∼100 km^3 (Reinthaler & Paul, 2025; Zemp et al., 2015). Over the past 20-30 years, area loss has accelerated up to 2% per year, concentrated around 3000 m a.s.l. but affecting all elevations (Paul et al., 2020; Sommer et al., 2020; Hugonnet et al., 2021). Recent inventories confirm ∼15% area reduction since 2003 alone, indicating sustained high shrinkage rates under current climate conditions (Paul et al., 2020). Slope failure inventories ($\geq 10^4$ m^3) show ∼40-50% of failures occur in recently deglaciated terrain, linking retreat to elevated instability in high-elevation periglacial belts (Fischer et al., 2012; Noetzli et al., 2003). These patterns mean paraglacial processes increasingly affect high-elevation slopes that remained ice-covered since the Last Glacial Maximum, destabilizing slopes predisposed to large rock slope failures as glacier surfaces lower (Kenner et al., 2021; Grämiger et al., 2017).
Climate warming will drive further glacier retreat over coming decades, with small glaciers disappearing and large valley glaciers fragmenting substantially, progressively exposing steep high-elevation rockwalls to paraglacial destabilisation and shifting zones of strongest glacial conditioning upslope (Paul et al., 2020; Sommer et al., 2020). This continued exposure of previously ice-shielded bedrock to thermal, hydrological, and mechanical boundary-condition changes will intensify preconditioning of slopes for large rock slope failures, even where timescales between deglaciation and collapse remain long (Grämiger et al., 2017; McColl, 2012; Kenner et al., 2021). Considerable uncertainties remain due to limited long-term in situ monitoring, but converging evidence from glacier and rock slope failure inventories, numerical models, and detailed monitoring of steep glacier-proximal rockwalls indicates that glacier retreat will continue to act as a key amplifier of both small, rapid rockfalls and progressive large-scale slope instabilities in the European Alps (Paul et al., 2020; Hartmeyer et al., 2020; Grämiger et al., 2017; Kenner et al., 2021).

2.3.2 Permafrost

Thawing permafrost has been identified as a major driver of enhanced rock slope instability in high-alpine environments by altering rock mass strength, fracture propagation, and hydro-mechanical behavior through thermal, cryostatic, and hydrological processes (Lindner et al., 2021; Haeberli & Beniston, 1998). In the European Alps, permafrost occurs discontinuously above roughly 2200-2800 m a.s.l. (ice-rich rock glaciers at lower limits; bedrock permafrost dominating >3000 m a.s.l.), typically as warm (near 0 °C) permafrost with meter-scale active layers sensitive to meteorological forcing (Gruber et al., 2004a; Kenner et al., 2019; Kenner et al., 2021; Haberkorn et al., 2021; Haeberli & Beniston, 1998). Permafrost can be categorized into ice-rich sediments (e.g., rock glaciers), ice-poor sediments, and fractured bedrock types, each influencing slope stability differently based on ice content, deformation potential, and interaction with bedrock discontinuities (Kenner et al., 2021).
In cold conditions, ice in fractures can contribute to the mechanical stability of steep rock slopes, whereas warming and thawing permafrost reduce resisting forces and favour instability (Kenner et al., 2021; Gruber & Haeberli, 2007). Ice bonding, thermal cracking, and water pressures, with effects varying by ice content and strain rate, modulate failure mechanisms (Kenner et al., 2021; Krautblatter et al., 2013). In ice-rich permafrost near lower limits, creep deformation occurs under self-weight but rarely triggers large rock failures. Ice-poor sediments can stabilize steep

slopes by resisting active-layer thaw, though deepening active layers under warming increase shear stresses and may detach entire slabs. In fractured bedrock, most relevant for steep rock walls, permafrost consists of ice and sub-zero temperature liquid water (Kenner et al., 2021). Freeze-thaw cycles and ice segregation drive near-surface cracking, while warming opens ice-sealed fractures to infiltration, raising hydrostatic pressures and reducing shear strength at rock-ice and rock-rock interfaces (Draebing & Mayer, 2021a; Kenner et al., 2021). Shallow rockfalls spike in summer heatwaves as warming weakens interfaces rapidly, whereas deep-seated instabilities evolve year-round as ice loses cohesion (Kenner et al., 2021; Phillips et al., 2025).

Permafrost warming and thaw reduce resisting forces through enhanced hydraulic conductivity and mechanical fatigue, acting as a preparatory factor that amplifies geological predispositions (Kenner et al., 2021; McColl, 2012). Warming permits water penetration into previously sealed fractures, where it accumulates behind intact deeper ice, refreezes in winter (adding cryostatic stress), or generates transient high pressures during rain/snowmelt (Kenner et al., 2021; Krautblatter et al., 2013). Thermo-mechanical models confirm highest frost-cracking intensity in permafrost rockwalls due to water availability, matching observed patterns of fracture density and strength loss, while purely thermal models underestimate this (Draebing & Mayer, 2021a). While attribution of individual large failures remains challenging due to sparse monitoring and limited understanding of the exact mechanisms, the surge in small-to-medium rockfalls since the 2000s correlates strongly with documented permafrost degradation (Gruber & Haeberli, 2007; Gruber et al., 2004b; Fischer et al., 2012; Noetzli et al., 2003).

Swiss and broader monitoring since the 1980s reveals widespread warming (0.5-1 °C), thicker active layers, and longer thaw periods, especially at ice-poor, snow-free sites (Haberkorn et al., 2021; Haeberli & Beniston, 1998). Warm near 0 °C permafrost zones are expanding, enhancing hydraulic conductivity (Kenner et al., 2021; Haberkorn et al., 2021). Evolution since the Last Ice Age shows partial thaw-readvance cycles, but recent decades indicate upslope shifts in typical rockfall detachment elevations, linking permafrost extents to failure hotspots in crystalline massifs (Fischer et al., 2012).

Warming projections expect the lower limit of permafrost to rise by several hundred meters, increasing the area no longer affected by permafrost, and the active zones increasing in depth (Haeberli & Beniston, 1998; Kenner et al., 2021). Projections consistently point to increased rockfall activity driven by enhanced frost-cracking intensity and greater water infiltration, with hybrid ice-debris hazards becoming more frequent (Draebing & Mayer, 2021a; Stoffel et al., 2014). However, substantial uncertainties remain due to scarcity of in-situ measurements and the reliance on laboratory-based studies for much of the current understanding of permafrost-rock-slope interactions, although monitoring expansions and thermo-hydro-mechanical models point to intensified small, rapidly responding events in summer and progressive large-scale failures year-round (Kenner et al., 2021; Gruber & Haeberli, 2007).

2.4 Climatology

2.4.1 Air temperature

Air temperature is a primary control on cryospheric components (snow cover, glaciers, permafrost, and ice aprons) that govern thermal, hydrological, and mechanical conditions critical to alpine rock slope stability (Kenner et al., 2021; McColl, 2012; Beniston et al., 2018). Rising mean temperatures drive long-term shifts in these components, progressively preconditioning slopes through changes in snow cover duration, glacier retreat, permafrost thaw, and altered frost-cracking regimes, as detailed in previous sections (Durand et al., 2009; Paul et al., 2020; PERMOS, 2016; Draebing & Mayer, 2021a). In contrast, short-term extremes, particularly high daily maximum temperatures and clusters of unusually warm days, can act as immediate triggers by rapidly melting surface and near-surface ice. This produces meltwater pulses that destabilize slopes pre-weakened by long-term warming (Allen & Huggel, 2013). Thus, sustained temperature increases act as slow preconditioning forces over decades, while daily or weekly extremes create acute thermal and hydraulic stresses that can initiate failure in critically weakened rock masses.

Episodes of extreme heat have particularly strong effects on steep, ice-influenced rockwalls. Rapid thawing of snow patches, ice aprons, and ice-filled joints generate short bursts of meltwater infiltration into fractures (Scherler et al., 2010; Offer et al., 2025). This process rapidly increases pore-water pressures, melts ice-bonded rock bridges, and reduces shear strength along critical discontinuities, promoting both gradual deformation and sudden failure in preconditioned slopes (Kenner et al., 2021; Preisig et al., 2016). Observations from permafrost sites, such as the Matterhorn north face, confirm that warm periods coincide with accelerated crack dilation and displacement, as meltwater penetrates previously isolated fracture systems (Hasler et al., 2012). Extremely warm days and heatwaves also drive rapid surface warming of rockwalls, inducing thermal expansion stresses capable of opening existing joints (Draebing, 2021b). Inventories link many large rock slope failures ($>10^4$ m^3) to such warm periods, underscoring that extreme temperatures can trigger collapse when long-term thermal weakening has already reduced rock mass strength (Fischer et al., 2012; Allen & Huggel, 2013; Paranunzio et al., 2016).

These temperature–driven processes align with observed long-term climatic trends across the European Alps. Long-term climate observations across the European Alps reveal sustained and accelerating warming over the past century. Alpine air temperatures have risen ∼1-2 °C on average since ∼1900, with a marked acceleration since the 1970s and 1980s onward at both low and high elevations (Gobiet et al., 2014; Auer et al., 2007; Begert et al., 2005). At high-elevation stations such as Jungfraujoch (3580 m a.s.l.), mean annual temperature rose by 1.8 °C between 1937 and 2005 (Appenzeller et al., 2008). Seasonal patterns show significant warming in all seasons, though the magnitude varies with elevation. Higher elevation stations display the strongest trends in autumn (0.8-1.3 °C per century), while lower stations show greater increases in winter (Begert et al., 2005). Maximum daily temperatures at high altitudes warm most significantly during spring and summer, whereas winter and autumn trends are smaller and statistically insignificant (Allen & Huggel, 2013). In addition, the frequency of extremely hot days has tripled since 1900 (Scherrer et al., 2016).

Building on these historical observations, climate projections indicate continued and intensified warming across the Alps throughout the 21st century. By mid-century, annual mean air temperatures are expected to rise by approximately 1-4 °C relative to 1991-2000, depending on emission scenarios (MeteoSwiss & ETH Zurich, 2025b; Gobiet et al., 2014). In addition to mean warming, the frequency and duration of heatwaves and warm extremes, such as the 2003 European heatwave, are projected to increase markedly (Gobiet et al., 2014). Events of this kind, already associated with several large alpine rock slope failures, may become up to four times more frequent by mid-century (Huggel et al., 2010). These effects are expected to intensify particularly at high altitudes, where reduced snow cover and declining albedo amplify warming, although the significance of the high-altitude albedo feedback is still under debate (Gobiet et al., 2014; Rottler et al., 2018). Although uncertainties remain, evidence from long-term monitoring, rock slope failure inventories, and case studies consistently indicates that both short-lived warm extremes and sustained temperature increases can compromise rock-slope stability (Allen & Huggel, 2013; Gobiet et al., 2014). Future climate conditions, characterized by higher mean temperatures and more frequent heatwaves, are therefore expected to further elevate the hazard potential of alpine rock slopes.

2.4.2 Freeze-thaw cycles

Freeze-thaw processes have already been introduced partly in the previous sections as a key driver of near-surface rock weathering and fracture propagation, particularly in permafrost-affected and recently deglaciated rockwalls (McColl, 2012; Kenner et al., 2021). They act mainly as preparatory mechanisms that progressively weaken rock masses rather than as isolated, immediate triggers. Repeated crossing of the freezing point causes water in fractures and pores to freeze, expand, and migrate, which widens joints, damages rock bridges, and reduces overall rock mass strength over seasonal to decadal timescales (Draebing & Mayer, 2021a; Kenner et al., 2021). The efficiency of freeze-thaw cycling depends strongly on both temperature regime and water availability. Frost-cracking intensity peaks where temperatures frequently oscillate around freezing and liquid water is available, though prolonged snow cover reduces effectiveness by insulating rock surfaces (McColl, 2012; Kellerer-Pirklbauer, 2017). Permafrost presence and snow cover modulate these conditions. In permafrost conditions, north-facing slopes and ice-poor, snow-free rockwalls can experience particularly effective frost cracking due to favourable temperature ranges and moisture conditions (Draebing & Mayer, 2021a; Kellerer-Pirklbauer, 2017). On the other hand, outside permafrost conditions, frost cracking is more common on south-facing rock walls (Kellerer-Pirklbauer, 2017). In combination with permafrost warming and glacier retreat, freeze-thaw cycles thus contribute to progressive damage that lowers the threshold for rock slope failures rather than acting as an isolated process.

Freeze-thaw activity shows complex altitudinal and seasonal patterns across the Alps. In Switzerland (1961-2005), thawing days increased by approximately 50% across all altitudes, with strongest relative increases between 1500-2500 m in inner-alpine regions during spring/autumn, and at high elevations (>3000 m) in summer (Appenzeller et al., 2008). Winter shows the largest absolute increases at 1000-1600 m. However, eastern Italian Alps analyses reveal contrasting trends, with freeze-thaw cycle days decreasing ∼7.3 days/decade at lower altitudes, supported by rock temperature monitoring showing shorter, less severe freeze events (Bonometti et al., 2026; Kellerer-Pirklbauer, 2017).

Projected warming will shift freeze-thaw activity upward, reducing cycles below ∼2200 m while increasing them above ∼2600 m, particularly in spring/winter (Migała et al., 2025; Appenzeller et al., 2008). Snow cover duration will shorten due to warmer, snow-poor winters, reducing time in the optimal frost-cracking temperature range, though permafrost sites may see enhanced cracking windows due to reduced snow insulation (Kellerer-Pirklbauer, 2017). Overall, intermediate/high-alpine belts face intensified freeze-thaw preparation of rock slopes despite site-specific variations.

2.4.3 Precipitation

Rainfall and prolonged wet periods are well-established triggers of rock slope failures as they elevate pore-water pressures through infiltration into fractures and discontinuities (McColl, 2012; Allen & Huggel, 2013). The hydrological response of a slope depends on its mechanical strength, hydraulic conductivity, and internal flow regime (McColl, 2012). Shallow failures typically react to short, high-intensity rainfall events, whereas deeper failures require sustained wet conditions to develop sufficient pore pressure (McColl, 2012). In high-mountain terrain, rainfall interacts strongly with permafrost and subsurface ice. The active layer in ice-poor permafrost lacks a latent heat buffer in the form of ice, making it especially sensitive during intense or prolonged wet periods (Kenner et al., 2021). In rock cleft systems, rainwater can fill open fractures, producing hydrostatic pressures of several megapascals, which reduce the shear strength of rock-rock and rock-ice interfaces and may eventually lead to rock-bridge failure (Kenner et al., 2021; Fischer et al., 2010). Through advective heat transport, infiltrating water also raises subsurface temperatures and accelerates permafrost thaw, thereby altering stress conditions and weakening rock bonds (Phillips et al., 2016). At high elevations, infiltration can be limited by thin basal ice layers, but as these layers thaw under warmer conditions, water penetration becomes easier, making summer rainfall more efficient in reducing stability (Phillips et al., 2016). Over longer timescales, cyclic hydrostatic loading from repeated wetting and drying promotes fracture propagation, while short-term pressure peaks during extreme rainfall can directly trigger rockfalls (Weber et al., 2017; Haeberli et al., 1997). Studies and inventories regularly attribute large rock slope failures to intense precipitation events or heavy snowmelt in alpine regions (Paranunzio et al., 2016; Crosta et al., 2004; PERMOS, 2025).

Precipitation across the European Alps shows strong spatial variability due to orography. Wet zones occur along the northern rim and in southern sectors, such as around Lago Maggiore and northeastern Italy, whereas inner-alpine zones like the Valais and the Aosta Valley remain comparatively dry (Frei & Schär, 1998). Seasonal patterns reveal winter as the driest and summer as the wettest period, with roughly twice the average precipitation amounts (Frei & Schär, 1998). Over the 20th century, precipitation intensity in Switzerland increased, especially along the northern and southern slopes, whereas inner-alpine areas showed smaller or statistically insignificant changes (Scherrer et al., 2016; Begert et al., 2005). The frequency of extreme precipitation events has also risen, particularly in summer due to more frequent thunderstorms (Scherrer et al., 2016). Other analyses, for partly different periods and stations, suggest that the greatest increases in precipitation intensity occurred in winter and autumn, whereas spring and summer exhibited minor or non-significant changes (Schmidli & Frei, 2005). Overall annual precipitation amounts within the Alps have remained relatively stable, with significant upward trends mainly in winter and in recent decades (Begert et al., 2005).

Climate projections indicate further seasonal and intensity-related shifts in Alpine precipitation patterns. Winter precipitation is projected to increase, while summer totals decline (Gobiet et al., 2014; Estermann et al., 2025). At higher elevations, heavy precipitation events are expected to become more frequent, and the return periods of extremes shorter (Gobiet et al., 2014; Scherrer et al., 2016). For short-duration convective extremes, events are projected to become less frequent but more intense, particularly for short-duration extremes in summer, whereas winter and autumn are expected to experience both higher frequency and greater intensity (Estermann et al., 2025). The strongest intensifications are anticipated in mountainous regions and for the most extreme percentiles of precipitation (Peleg et al., 2025; Rajczak et al., 2013). Overall, these changes indicate a shift toward shorter but more severe precipitation episodes (Estermann et al., 2025), which, together with ongoing permafrost degradation and glacier retreat, are likely to amplify hydrological and thermal stresses on alpine rock slopes and increase instability throughout the 21st century.

3 Data and Methods

To identify potential influencing factors and assess the possible influence of climate change on the frequency and magnitude of rock slope failures, a quantitative analysis based primarily on descriptive statistics was conducted. Given the limited number of documented events (n=68) available for analysis, the focus was placed on exploratory and descriptive approaches rather than on inferential statistical testing. The overall methodological workflow comprised the compilation of multiple spatial and non-spatial datasets, their preprocessing and harmonization, and the subsequent statistical and spatial analysis. This section provides an overview of the data sources used in the study and outlines the main steps taken to prepare and analyze the data. The statistical analyses were performed mainly using descriptive measures to characterize patterns and relationships within the data. Spatial analyses were carried out using a geographic information system (GIS). Statistical metrics were calculated for two spatial extents: first, for the detachment zones of the documented rock slope failures, and second, for the entire study area. This allows for a comparison between failure-prone locations and the general background conditions, thereby supporting the identification of potential controlling factors.

3.1 Study Area

The study area covers approximately 35'000 km^2 across the Alpine arc, primarily covering the French, Italian, Swiss and Austrian Alps, but extending into Alpine regions of seven countries in total. It is restricted to regions with a minimum elevation of 2000 m. This was done using

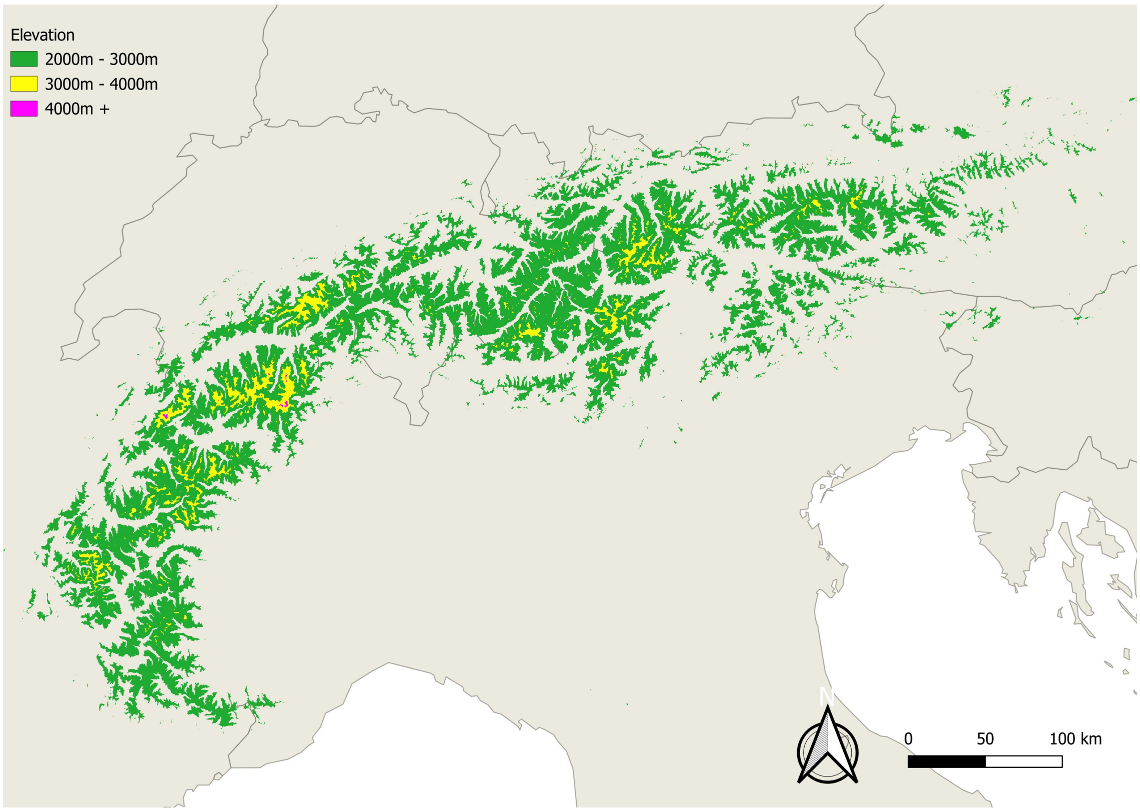

Figure 1: Map of the study area

a digital elevation model (DEM) by applying an elevation threshold of 2000 m, which was consistently used for all spatial datasets. Of this area, ∼94% lies between 2000 m and 3000 m, while ∼6% is above 3000 m. The spatial extent of the study area is shown in Figure 1.
As this study focuses on the potential changes in the glacial and periglacial environment due to climate change, only rock slope failures with a detachment zone at elevations of 2000 m a.s.l. or higher were considered. Furthermore, only rock slope failures with an estimated volume exceeding 10^5 m^3 and that occurred within the past 100 years (1925-2025) were included, in order to ensure sufficient data availability and comparability across events. All spatial datasets were processed within the same spatial extent to ensure methodological consistency. This definition of the study area provides the spatial basis for the comparison between detachment zones and background conditions presented in the subsequent analyses.

3.2 Inventory

The inventory presented here is an extension of existing inventories in terms of both the number of events and the aspects examined. It builds upon previously published datasets while systematically incorporating events that were either omitted in earlier compilations or that have occurred more recently. The rockfall database maintained by the Swiss Permafrost Monitoring Network (PERMOS) served as the primary starting point (PERMOS, 2025). This dataset was subsequently expanded with events from other established inventories, namely those compiled by Noetzli et al. (2003), Fischer et al. (2012) and Paranunzio et al. (2016).
Furthermore, additional events were identified through an extensive review of the scientific literature and individual case studies, including documented rock slope failures from Austria (Fuchs et al., 2018; Zangerl et al., 2019), the Vallon d'Etache rock slope failure (Cathala et al., 2024) and the events in the vicinity of the Miage Glacier (Deline, 2009), among others. All events included in the inventory meet the selection criteria defined in Section 3.1 with respect to elevation, volume, and time period.
Overall, a total of 68 rock slope failures were compiled in this inventory, which forms the basis for the subsequent statistical and spatial analyses. The complete list of events and their main characteristics is provided in Table 1. Despite efforts to ensure consistency across sources, the inventory is not assumed to be exhaustive, particularly for earlier decades, and potential reporting biases are considered in the interpretation of the results.
All events were harmonized as far as possible with respect to names, coordinates, date, and volume estimates. Furthermore, volume classes were defined, to facilitate subsequent analyses. These classes are: Class 1: 100'000 to 500'000 m^3, Class 2: 500'000 to 1'000'000 m^3, and Class 3: ≥1'000'000 m^3. These classes were defined based on the distribution of events across volume ranges and to broadly coincide with different levels of environmental impact.

3.3 Topography

For the analysis of topography a pan-European digital terrain model (DTM) was used (Hengl et al., 2022). The model has a spatial resolution of 30 m and covers the entire European Alps. This dataset was selected to ensure consistent spatial coverage and comparability across the full extent of the multinational study area. In addition to elevation, the DTM also includes derivatives for both slope gradient and aspect. For each documented rock slope failure, three topographic characteristics were determined for the detachment zone: elevation, slope gradient,

Table 1: List of documented large rock slope failures

No	Name	Date	X coord.	Y coord.	Volume (m^3)	Mean elevation
1	Kleines Nesthorn (CH)	19 May 2025	46.3968	7.8410	$6 \cdot 10^6$	3260
2	Dent de Pro (CH)	02 November 2024	45.9017	7.2420	$1.3 \cdot 10^5$	3487
3	Tschingelhorn (CH)	03 October 2024	46.8984	9.2215	10^5	2800
4	Portalet/Ravines Rousses (CH)	21 June 2024	45.9897	7.0695	10^5	2700
5	Piz Scerscen II (CH)	14 April 2024	46.3792	9.8964	$5.5 \cdot 10^6$	3640
6	Piz Scerscen I (CH)	15 October 2023	46.3816	9.8957	$5 \cdot 10^5$	3535
7	Fluchthorn (AT/CH)	11 June 2023	46.8932	10.2269	10^6	3396
8	Piz Umur (CH)	10 February 2023	46.3888	9.8891	$5.2 \cdot 10^5$	3250
9	Ritzlihorn/Mattenlimmi (CH)	30 September 2020	46.6414	8.2522	$1.5 \cdot 10^5$	2625
10	Grosser Graben St. Niklaus (CH)	29 June 2020	46.1523	7.8225	$2 \cdot 10^5$	2680
11	Vallon d'Etache (FR)	18 June 2020	45.1686	6.8462	$2.3 \cdot 10^5$	3120
12	Steingletscher II (CH)	21 February 2020	46.7044	8.4387	10^5	2500
13	Steingletscher I (CH)	17 November 2019	46.7044	8.4387	$1.9 \cdot 10^5$	2500
14	Flüela Wisshorn (CH)	19 March 2019	46.7614	9.9648	$2.5 \cdot 10^5$	3022
15	Cengalo VI (CH)	15 September 2017	46.2975	9.6027	$4 \cdot 10^5$	2970
16	Cengalo V (CH)	23 August 2017	46.2971	9.6028	$3 \cdot 10^6$	3075
17	Cengalo IV (CH)	21 August 2017	46.2980	9.6024	$1.5 \cdot 10^5$	2900
18	Trajo Glacier (IT)	14 July 2017	45.6001	7.2677	$5 \cdot 10^5$	3500
19	Cengalo III (CH)	11 September 2016	46.2987	9.6014	$1.6 \cdot 10^5$	3020
20	Picola Croda Rossa (IT)	18 August 2016	46.6482	12.1226	$1.6 \cdot 10^6$	2770
21	Punta Tre Amici II (IT)	16 December 2015	45.9268	7.9085	$2 \cdot 10^5$	3400
22	Sölden/Schartlaskogel (AT)	02 October 2015	47.0051	10.9728	$1.7 \cdot 10^5$	2720
23	Mulets de la Lia (CH)	09 December 2014	45.9918	7.3352	$3 \cdot 10^5$	2677
24	Piz Kesch (CH)	February 2014	46.6236	9.8767	$1.5 \cdot 10^5$	3107
25	Cengalo II (CH)	24 September 2013	46.2967	9.6064	10^5	2740
26	Crast'Agüzza (IT)	28 February 2013	46.3694	9.9160	$1.1 \cdot 10^5$	3850
27	Wasenhorn (CH)	11 August 2012	46.7577	8.4446	$2.2 \cdot 10^5$	2700
28	Taschachtal (AT)	29 May 2012	46.9180	10.8188	$1.5 \cdot 10^5$	2460
29	Hochwand/Alpl (AT)	22 March 2012	47.3535	11.0041	$1.5 \cdot 10^5$	2250
30	Cengalo I (CH)	27 December 2011	46.2958	9.6022	$1.5 \cdot 10^6$	3170
31	Sass Maor (IT)	19 December 2011	46.2349	11.8511	$1.8 \cdot 10^5$	2200
32	Birghorn (CH)	18 November 2011	46.4534	7.7789	$5 \cdot 10^5$	2996
33	Punta Tre Amici I (IT)	26 September 2010	45.9294	7.9074	10^5	3200
34	Punta Thurwieser II (IT)	05 September 2010	46.4950	10.5260	10^5	3630
35	Mont Crammont (IT)	24 December 2008	45.7665	6.9394	$5.4 \cdot 10^5$	2600
36	Punta Patri Nord (IT)	18 September 2008	45.5417	7.3628	10^5	3330
37	Bliggspitze (AT)	29 June 2007	46.9216	10.7835	$4.1 \cdot 10^6$	3250
38	Monte Rosa II (IT)	21 April 2007	45.9323	7.8780	$1.5 \cdot 10^5$	4130
39	Dents Blanches (CH)	08 November 2006	46.1329	6.8322	10^6	2517
40	Dent du Midi (CH)	29 October 2006	46.1636	6.9184	10^6	2793
41	Cima Dodici (IT)	20 July 2006	46.6183	12.3603	10^5	3094
42	Drus (FR)	29 June 2005	45.9300	6.9500	$2.7 \cdot 10^5$	3410
43	Punta Thurwieser I (IT)	18 September 2004	46.4950	10.5260	$3 \cdot 10^6$	3630
44	Gruben (CH)	2002	46.1644	7.9902	10^5	3520
45	Mättenberg/Ankenbaelli (CH)	08 September 2000	46.6035	8.0825	10^5	2873
46	Zuetribistock III (CH)	31 March 1998	46.8518	8.9477	10^5	2300
47	Brenva (FR)	18 January 1997	45.8371	6.8822	$2 \cdot 10^6$	3872
48	Zuetribistock II (CH)	03 March 1996	46.8508	8.9483	$1.8 \cdot 10^6$	2200
49	Zuetribistock I (CH)	24 January 1996	46.8520	8.9490	$4.7 \cdot 10^5$	2300
50	Miage III (IT)	May 1991	45.7990	6.8516	$3 \cdot 10^5$	3000
51	Randa (CH)	18 April 1991	46.1132	7.7745	$3 \cdot 10^7$	2300
52	Piz Morteratsch/Tschierva (CH)	29 October 1988	46.4000	9.8943	$3 \cdot 10^5$	3180

No	Name	Date	X coord.	Y coord.	Volume (m^3)	Mean elevation
53	Miage II (IT)	May 1988	45.8129	6.8558	$2 \cdot 10^5$	3350
54	Val Pola (IT)	28 July 1987	46.3772	10.3325	$3.3 \cdot 10^7$	2320
55	Fiernaz (IT)	17 January 1982	45.8333	7.5847	$5 \cdot 10^5$	2000
56	Monte Rosa I (IT)	1980	45.9343	7.8785	$10^5 - 10^6$	3940
57	Chli Spannort (CH)	28 December 1961	46.7801	8.5141	10^6	2934
58	Garde de Bordon II (CH)	22 July 1954	46.1151	7.6092	$10^5 - 10^6$	2900
59	Feegletscher (CH)	07 July 1954	46.1032	7.9042	$1.5 \cdot 10^6$	2330
60	Becca de Luseney (IT)	08 June 1952	45.8689	7.4854	10^6	3054
61	Garde de Bordon I (CH)	17 July 1948	46.1151	7.6092	$10^5 - 10^6$	2900
62	Rawilhorn (CH)	30 May 1946	46.3465	7.4130	$6 \cdot 10^6$	2527
63	Miage I (IT)	1945	45.7991	6.8253	$4 \cdot 10^5$	3400
64	Matterhorn (IT)	09 July 1943	45.9745	7.6613	$2.4 \cdot 10^5$	4150
65	Piz Beverin (CH)	11 July 1938	46.6544	9.3579	$7 \cdot 10^5$	2797
66	Jungfrau (CH)	06 October 1937	46.5449	7.9706	$1.5 \cdot 10^5$	3809
67	Chli Windgällen (CH)	10 August 1936	46.7955	8.7160	$1.5 \cdot 10^5$	2700
68	Felikhorn (IT)	04 August 1936	45.8991	7.7900	$2 \cdot 10^5$	3585

and aspect. For events where the spatial extent of the detachment zone was available from the literature, mean values calculated over the detachment area were used for elevation. Otherwise, elevation was extracted at the reported coordinates provided in the literature. To allow direct comparison between individual events and the overall study area, elevation values were classified into 200-m elevation bands ranging from 2000-2200 m to >4400 m.
Slope gradient was derived using the slope gradient layer of the DTM. For events where slope gradient values were reported in the literature (e.g., Noetzli et al., 2003), those values were preferentially adopted, given the limited spatial resolution of the DTM. Slope gradients were categorized into eight classes ranging from 0-10° to >70°, to reduce uncertainty and ensure methodological consistency across all events and spatial scales.
Aspect was determined using the aspect derivative of the DTM and complemented with published information where available (e.g., Fischer et al., 2012). For comparability, aspect values were grouped into eight directional classes corresponding to the main cardinal and intercardinal directions: N, NE, E, SE, S, SW, W, NW.
Detailed topographic variables for each rock slope failure are provided in Table 4 in the Appendix.

3.4 Lithology

The lithology of each detachment zone was determined using geological or lithological maps, supplemented with information from the literature where necessary. For Switzerland and areas close to the border, the Geological Atlas of Switzerland at a scale of 1:25’000 was used (Swisstopo, 2024). For Austria, provisional geological maps at a scale of 1:50’000 were consulted (Geofast, 2024). In the Valle d’Aosta region, the geotechnical map of Valle d’Aosta at 1:150’000 scale was used (De Giusti et al., 2004), while for Trentino, the lithological map of Trentino at a scale of 1:200’000 was used (Bosellini et al., 1999). Where no suitable map was available, lithology was determined directly from literature sources.
To facilitate comparison between events, lithology was simplified into six classes following Fischer et al. (2012): *granit/diorit*, *mafic metamorphic*, *limestone/dolomite*, *conglomerate*, *schist*, and *gneiss*. The overall distribution of lithological classes across the study area was obtained

from Fischer et al. (2012), whose geological setting is derived from the Geotechnical Environmental Atlas of Switzerland (1:200'000). Since the study area of Fischer et al. (2012) is considerably smaller than the full study area of this work, two separate comparisons were performed with the documented rock slope failures. First, the comparison considered only failures occurring within the area covered by Fischer et al. (2012), and second, all documented failures were included, even those outside this area.
Additionally, for each event it was recorded whether a tectonic fault or fracture was present in proximity to the detachment zone. This assessment refers exclusively to faults or fractures of tectonic origin that could act as a preconditioning factor for slope instability, and does not include fractures related to weathering or other non-tectonic processes. This information was derived from the geological maps or literature and assessed qualitatively. No explicit distance threshold was applied, but a fault or fracture was considered relevant if it could have plausibly affected the stability of the slope in the detachment zone.
Detailed lithological characteristics for each rock slope failure are provided in Table 5 in the Appendix.

3.5 Cryosphere

3.5.1 Glaciers

To assess the potential influence of glaciers and changes in glaciation since the Last Ice Age (LIA; 1850), the glaciation history of each detachment zone was evaluated qualitatively. The influence of glaciers was examined for each detachment zone at the time of failure and categorized into four classes: (1) no glaciation, (2) glaciation within the slope, (3) glaciation at the base of the slope, and (4) slope recently deglaciated.
Rock slope failures were classified as not influenced by glaciers when neither surface ice within the slope nor a glacier at its base was present at any time since the end of the LIA (1850). Glaciation within the slope denotes cases where surface ice is, or has been since 1850, located in the immediate vicinity of the detachment zone. Glaciation at the base of the slope refers to the presence of a glacier at the foot of the slope at any time since 1850. The fourth class, recently deglaciated, includes detachment zones that remained glacier-covered in or after 1850 and were exposed only following subsequent glacier retreat.
As the primary data sources, national glacier inventories were used, as they provide the highest level of detail and temporal resolution. For Switzerland, glacier inventories produced by the Glacier Monitoring Service Switzerland (GLAMOS) were used. The datasets relevant for this study include inventories from 1931 (Mannerfelt et al., 2022), 1973 (Müller et al., 1976; Maisch et al., 2000; Paul, 2004), 2010 (Fischer et al., 2014), and 2016 (Linsbauer et al., 2021). The first dataset from 1931 is based on terrestrial photographs and topographic maps, whereas all the newer inventories are based on aerial imagery.
For Austria, the official Austrian glacier inventory was used (Fischer et al., 2015a), comprising datasets from 1969, 1998, and 2006 (Fischer et al., 2015b). The 1969 and 1998 inventories are based on orthophoto maps, while the 2006 dataset additionally incorporates high-resolution LiDAR-derived digital elevation models. In addition, the most recent update from 2015, based on Google Earth imagery, was included (Buckel et al., 2018a; Buckel et al., 2018b).
For France, glaciation history was derived from the work of Gardent et al. (2014), based on topographic maps, aerial photographs, and satellite imagery, with glacier extents available for 1867/1971, 1985/1986, 2003, and 2006/2009.

For Italy, several historical glacier inventories exist; however, most do not provide spatially explicit glacier outlines, complicating the assessment of glacier changes at individual detachment zones. Nevertheless, using a dataset representing glacier extent at the LIA (Reinthaler & Paul, 2025) together with modern Italian glacier inventories (Salvatore et al., 2015; Smiraglia et al., 2015), a qualitative evaluation of glaciation conditions was possible.
For the spatial analysis of glacier extent and change across the entire study area since the LIA, two datasets were used: glacier extent at the LIA (Reinthaler & Paul, 2025) and the most recent glacier extent dataset for the Alps available (Paul et al., 2020). Glacier change was assessed for the entire study area as well as across different elevation zones, allowing for a comparison of glacier retreat patterns with elevation.
The state of glaciation of each detachment zone is documented in Table 6 in the Appendix.

3.5.2 Permafrost

For the assessment of permafrost distribution, the Alpine Permafrost Index Map (APIM) was used (Boeckli et al., 2012a), together with its supplemented dataset for large-scale analyses (Boeckli et al., 2012b). The APIM covers the entire Alpine arc and therefore ensures spatial consistency and comparability across all documented rock slope failures. Permafrost distribution is modeled using a unified statistical approach for both debris-covered and bedrock surfaces, based on mean annual air temperature, potential incoming solar radiation, and precipitation as primary predictors. Offset terms are included to account for terrain types that were not fully represented in the original calibration dataset (Boeckli et al., 2012a).
The resulting permafrost index is a continuous, qualitative measure that does not define discrete permafrost boundaries. To facilitate comparison between events and with the overall study area, the continuous index was classified using k-means clustering, partitioning the dataset into four distinct classes: (1) no permafrost, (2) permafrost only in very favorable conditions, (3) permafrost mostly in cold conditions, and (4) permafrost in nearly all conditions. This classification approach allows a simplified yet systematic representation of permafrost likelihood while preserving relative differences across the study area.
To determine whether permafrost was present in the detachment zone of each individual rock slope failure, the classified APIM dataset was used to assign a permafrost class to each event. In a subsequent step, these assignments were qualitatively cross-checked using published case studies and independent inventories containing information on permafrost occurrence (e.g. PERMOS, 2025), where available, and also compared with the lower permafrost boundary from the PERMAKART model (Keller, 1992).
The potential use of historical permafrost distributions was explored to assess whether permafrost degradation over the past century could be linked to reduced slope stability. However, spatially explicit permafrost data at a regional scale are only available from the late 20th century onwards, as systematic permafrost research in the Alps intensified mainly after the 1980s. While recent modeling approaches allow the reconstruction of permafrost evolution at individual sites, these methods require detailed local input data and were therefore beyond the scope of this study (e.g. Kenner et al., 2024). The lower permafrost boundary in 1850 was estimated to be roughly 300 m lower than today, based on simulations using mean annual air temperature (Hoelzle & Haeberli, 1995) and estimated warming of 1.8 °C since 1850 (Appenzeller et al., 2008).
Permafrost distribution across the entire study area was assessed using the same dataset as for the event-based analysis. In addition to the overall distribution, permafrost occurrence was

analysed across different elevation zones to enable comparison with the spatial distribution of rock slope failures. Temporal changes in permafrost distribution were not analysed due to the lack of long-term, spatially consistent permafrost datasets at the Alpine scale.
Permafrost occurrence at each detachment zone is documented in Table 6 in the Appendix.

3.6 Climatology

Climatological data were used to assess whether short- and long-term climatic conditions may have contributed to triggering of rock slope failures. Three variables were examined: (a) daily air temperature (mean and maximum), (b) daily precipitation totals, and (c) the occurrence of freeze-thaw cycles (FTCs).
Meteorological data were obtained from automatic and manual weather stations operated by national and regional weather services. For Switzerland, Austria, and France, data were provided by the respective national meteorological agencies (MeteoSwiss, 2025a; GeoSphere Austria, 2025a; Météo-France, 2025). For Italy, data were obtained from regional services in Valle d'Aosta (CFVDA, 2025), South Tyrol (Autonome Provinz Bozen - Südtirol, 2025), and Trentino (Meteotrentino, 2025).
Weather stations were selected based on data availability, elevation, and proximity to documented rock slope failures. Temperature-based analyses relied on four high-elevation stations distributed across the Alps, chosen to ensure long and continuous records. To account for elevation differences between meteorological stations and detachment zones, a standard environmental lapse rate of 0.006 $^{\circ}\mathrm{C}\cdot\mathrm{m}^{-1}$ was applied to all data prior to temperature-based analyses (Rolland, 2003). Precipitation analyses used data from 31 stations, primarily selected based on proximity to failure sites, with preference given to stations with longer time series when multiple stations were available at similar distances. All used weather stations and their characteristics are listed in Table 7 in the Appendix. Additionally the corresponding weather station for each documented rock slope failure is documented in Table 8 in the Appendix.

3.6.1 Air temperature

Daily mean and maximum air temperature were analyzed to characterize thermal conditions preceding rock slope failures. Mean temperature data were available for all events, while maximum air temperature data were limited to records from 1960 onward. For each event, temperature metrics were calculated over four antecedent time windows ending on the day before failure: 1, 7, 30, and 90 days.
For each window, the average mean air temperature and average maximum air temperature were calculated and evaluated relative to a climatological reference period (1961-1990). At the Weissfluhjoch maximum temperature records start in 1971 and at the Col du Grand St-Bernard in 1965. Therefore, the reference period for maximum temperature for those two weather stations is shortened. The reference distribution was constructed using a rolling-window approach, incorporating ± 7 days around the corresponding calendar day to account for short-term seasonal variability. Observed temperatures were expressed as percentile ranks relative to the reference distribution using linear interpolation. Events with mean or maximum temperatures exceeding the 95th percentile of the reference distribution were deemed climatologically relevant, indicating unusually warm conditions preceding failures.
In addition, the occurrence of extremely warm days was quantified. Extremely warm days were defined as days exceeding the 95th percentile of the day-specific reference temperature

distribution. For each rock slope failure, the number of extremely warm days was counted within the same antecedent windows (1, 7, 30, and 90 days), separately for mean and maximum air temperature. Under a binomial null model ($p = 0.05$), statistically extreme thresholds, where $P(X \geq k) \leq 0.05$, were 1 (1d), 2 (7d), 4 (30d), 9 (90d). Events exceeding these thresholds were deemed climatologically relevant.
Detailed data for mean temperature, maximum temperature and number of warm days for each rock slope failure are provided in Tables 9, 10 and 11 in the Appendix.

3.6.2 Freeze-thaw cycles

Freeze-thaw cycles were identified using daily minimum and maximum air temperature records. A freeze-thaw cycle was defined as a day during which temperatures crossed 0 °C. Two complementary analyses were conducted: a long-term trend analysis and an event-based assessment.
Long-term trends in FTC occurrence were analyzed using data from the four high-elevation stations over the period 1961-2024. FTC occurrences were aggregated annually and seasonally, following standard climatological seasons: winter (DJF), spring (MAM), summer (JJA), and autumn (SON). Trends were assessed using the non-parametric Mann-Kendall test, and trend magnitudes were estimated using Sen's slope estimator. Statistical significance was evaluated at $\alpha = 0.05$.
For individual rock slope failures, the number of FTCs preceding each event was quantified over the same antecedent windows used for temperature analysis (1, 7, 30, and 90 days). Observed FTC counts were compared to a climatological baseline derived from the reference period (1961-1990), again using a ±7-day moving window around the event's calendar day. Percentile ranks (except for the 1-day window) were calculated, to quantify each event's relative FTC extremeness against this baseline.
Detailed data for the FTC count and the associated percentiles for each rock slope failure is provided in Table 12 in the Appendix.

3.6.3 Precipitation

Daily precipitation data were quality-checked and standardized prior to analysis. For each rock slope failure, antecedent precipitation was quantified over four look-back windows (1, 7, 30, and 90 days), defined to end on the day immediately preceding the failure.
Within each window, both the total precipitation amount and the number of heavy-precipitation days were calculated. Heavy precipitation was defined as daily totals exceeding 25 mm, following thresholds suggested in Alpine climatological studies (Frei & Schär, 2001; Brönnimann et al., 2018). Across the available station records, this threshold corresponds approximately to the 97.6th percentile of daily precipitation. Under a binomial null model ($p = 0.05$), statistically extreme thresholds, where $P(X \geq k) \leq 0.05$, were 1 (1d), 2 (7d), 4 (30d), 9 (90d). Events exceeding these thresholds were deemed climatologically relevant.
To assess the extremeness of precipitation conditions preceding failures, window totals were compared to empirical distributions derived from the full historical record. Seasonal variability was accounted for by restricting comparisons to historical windows occurring within ±30 days of the event's day of year.
Detailed data for the precipitation sums and the associated percentiles, as well as the number of days with heavy rainfall for each rock slope failure is provided in Tables 13 and 14 in the Appendix.

4 Results

4.1 Spatial distribution

The spatial distribution of the documented rock slope failures is shown in Figure 2, based on the data outlined in Table 1. Of the 68 events, 39 occurred in Switzerland, 21 in Italy, five in Austria, and three in France, while no events were identified in Germany, Slovenia, or Liechtenstein. The failures can be grouped into three main clusters: (i) the largest cluster in the Valais Alps, extending from the Mont Blanc Massif to the Monte Rosa Massif and adjacent valleys, (ii) a second cluster stretching from the Bernese Alps to the Glarner Alps, forming an arc with numerous failures, and (iii) a third cluster centered on the Bernina Massif in the southeastern Swiss Alps. Clustering was identified visually from the spatial distribution rather than using formal clustering metrics. In addition, several isolated failures occurred in the western Austrian Alps, west of the Bozen Valley, and south of the Aosta Valley.
There are also several localized clusters, highlighted in Figure 2, where multiple rock slope failures either occurred on the same slope, in close vicinity, or where new failures developed within the scars of previous ones. These clusters include: (a) the Miage Glacier, where three documented events occurred in close proximity on opposite sides of the glacier; (b) Garde de Bordon, where a second failure occurred within the scarp of a previous event that had occurred six years earlier; (c) Monte Rosa / Punta Tre Amici, where four failures occurred along the same steep flank of the Monte Rosa Massif; (d) Steingletscher, where two failures occurred on a rock step, which was recently deglaciated, in consecutive years; (e) Zuetribistock, where three

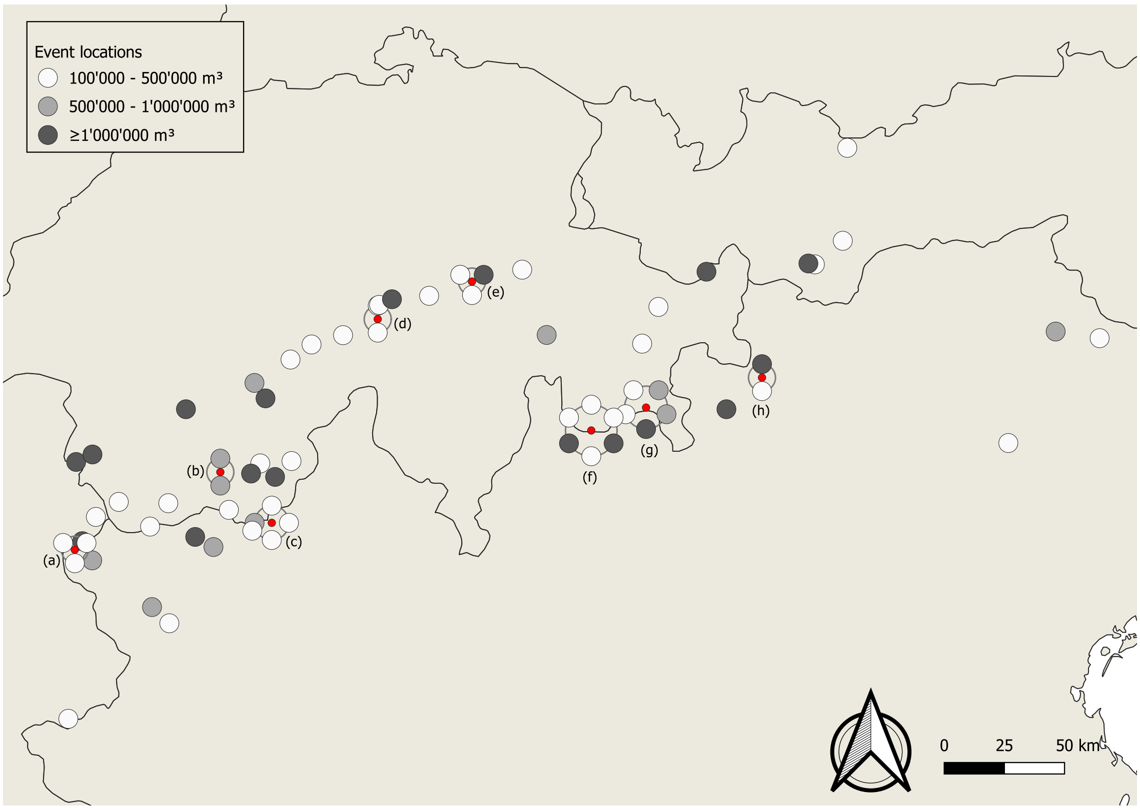

Figure 2: Spatial distribution of the documented rock slope failures, classified by their volumetric class. Rock slope failure clusters are indicated by red points.

failures developed on the same slope within two years; (f) Piz Cengalo, where six failures occurred over a span of six years within the same flank; (g) Piz Scerscen / Piz Umur / Piz Morteratsch / Crast Agüzza, where five failures occurred in close proximity, two of which originated from the same zone (Piz Scerscen); and (h) Punta Thurwieser, where a second failure occurred six years after the first, from the same scarp area.
The main clusters broadly coincide with the highest, most heavily glaciated areas of the Alps. Similarly, some of the local clusters are located close to the highest peaks of the Alps, such as the Mont Blanc Massif, the Monte Rosa Massif and the Bernina Massif. Relationships between the spatial distribution of failures and controlling factors are outlined in later sections.
When considering the estimated failure volumes, grouped into three volume classes as defined in section 3.2, no distinct large-scale spatial pattern emerges, as large events are distributed across all regions. In some areas, very large failures, such as those at Piz Scerscen and Piz Cengalo, occur alongside one or multiple smaller events, whereas others appear more spatially isolated. Particularly noteworthy are the regions where no rock slope failures are recorded, such as the south-western Alps, where only one event is documented, and the eastern Austrian Alps (east of Innsbruck), where no events are included in the inventory.
These apparent gaps may indicate genuinely lower occurrence rates, but they could also reflect spatial biases in documentation and mapping completeness or language barriers.

4.2 Temporal distribution

The documented rock slope failures in the study area show an uneven distribution over time (Figure 3a). The temporal pattern can be divided into three distinct phases. From the 1930s to the 1950s, only 11 events in total (approximately four events per decade) were documented, indicating a low and relatively stable activity level. This period is followed by two decades (1960s-1970s) with very few documented events (1 event in total), representing a pronounced minimum in the record. It is unclear whether this low level of activity reflects a true reduction in occurrence or simply stochastic variability given the small sample size. After 1980, the number of documented rock slope failures increases gradually from about 5 events per decade in the 1980s to over 20 events per decade in the 2010s, marking a shift toward higher activity. While activity levels in the 1980s and 1990s remain similar to earlier decades, a pronounced change occurs after 2000, when event frequencies increased noticeably and culminate in the 2010s and early 2020s. Over the entire observation period, 12 events were documented before 1980 compared to 56 after 1980, underscoring the increase in frequency in recent decades. In addition to the decadal view, the annual event rate (Figure 3b) shows that the high number of events in the 2010s is not an outlier, as in the current decade a similar number of events were documented per year.
When considering event volume, a noticeable change can be observed after 2000. Before 2000, the number of events in the smallest volumetric class was smaller than the number of events in the two higher volume classes combined (10 events vs. 13 events). After 2000, this ratio changes to 30 events vs. 15 events, indicating that while failures of all classes increased in frequency, this trend is most pronounced for the smallest volumetric class. Before 2000, there were only about 1 or 2 events per decade in the smallest volumetric class, while after 2000 this increases to over 10 events per decade. Although smaller events dominate numerically in the most recent decades, the number of events larger than 500'000 m^3 also increased slightly.

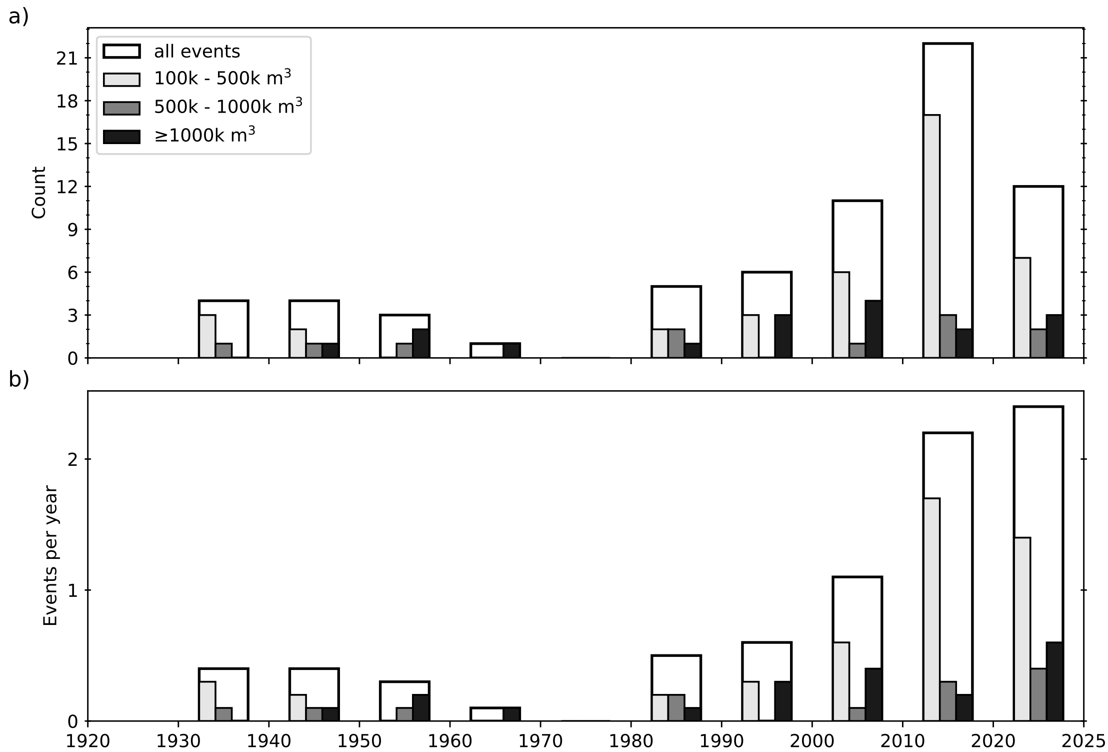

Figure 3: Number of documented rock slope failures per decade, subdivided by volumetric class. (a) shows the total count and (b) count per year.

Before 2000, about 1 or 2 large events were documented per decade, which increases to roughly 5 events per decade after 2000. Failures of the larger volume classes (> 500'000 m^3) are likely to have been documented even in earlier decades, so the temporal pattern in this volume range is probably less affected by reporting bias.
Overall, the data suggest a marked increase in the frequency of rock slope failures in recent decades across all volume classes. Increased development and human presence in alpine areas, including more infrastructure and better communication, likely contribute to higher recording rates, particularly for smaller events. This potential reporting bias needs to be considered when interpreting the apparent trend in frequency. At the same time, the apparent increase in the larger volume classes, which are less sensitive to under-reporting, may also reflect changing environmental conditions, which are analyzed and discussed in later sections.
When looking at the seasonal distribution of the rock slope failures (Figure 4), the frequency is highest in summer and fall, with 21 and 19 events respectively. Together, these two season account for nearly 60% of all documented events. In winter and spring, only 13 events are documented in each season, corresponding to about 19% per season. An additional two events fall into the "unknown" category, for which the exact failure date could not be determined.
Seasonal distribution for the smallest volumetric class (100'000 to 500'000 m^3) shows a clear peak in autumn with 14 events. In the other seasons the failure activity is comparatively lower but still considerable. For the two larger volume classes, similar numbers of rock slope failures

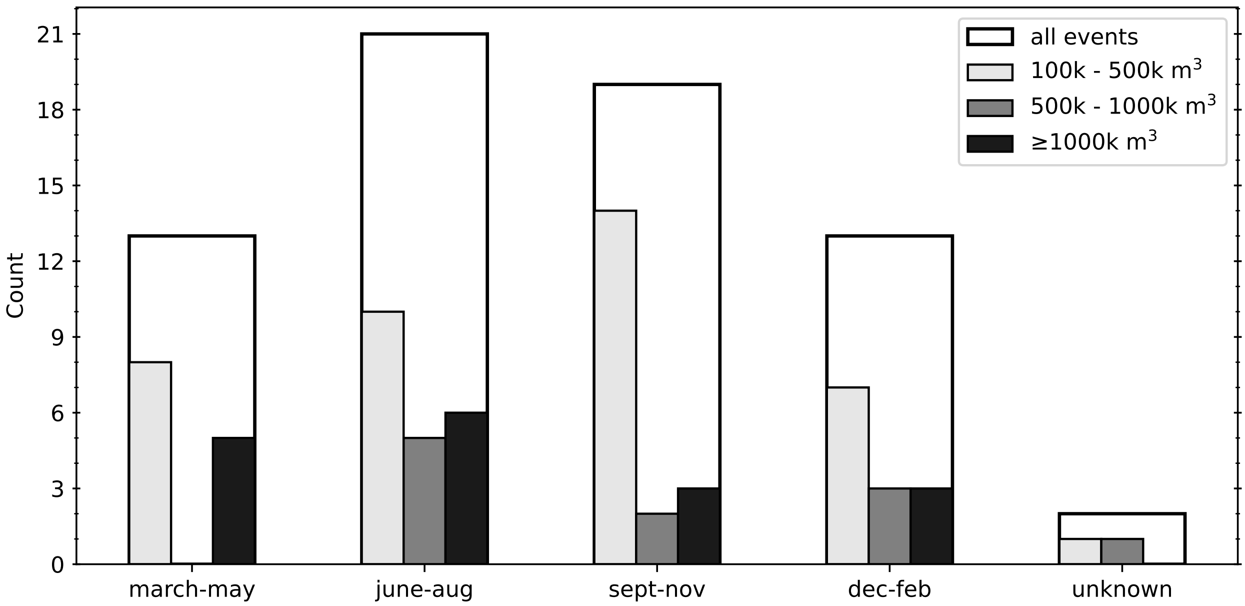

Figure 4: Number of documented rock slope failures per season, subdivided by volumetric class.

occur in winter, spring and autumn (6, 5, and 5 events respectively), whereas there is a clear peak in summer (11 events). Notably, in spring there are no events of the intermediate volume class, but instead a similar number of events of the largest volume class as in summer. Overall, seasonal distribution indicates that events of the smallest volumetric class show a autumn peak, while events of the two larger volume classes show a summer peak.
The increased frequency of rock slope failures in summer and autumn suggests that seasonal conditions influence rock slope failure activity. The observed peaks are consistent with processes such as increased meltwater infiltration and permafrost degradation during the warm season, as well as more intense rainfall events in late summer and autumn, all of which can decrease slope stability. Given the limited sample size, these patterns should be interpreted cautiously.

4.3 Topography

4.3.1 Elevation

When comparing the elevation of the detachment zones with the elevation distribution of the entire study area (Figure 5), clear differences emerge. The relative area of the study area decreases with increasing elevation, starting at roughly 28% between 2000 and 2200 m and declining to almost 0% above 4000 m. The elevation distribution of the detachment zones, on the other hand, is much more even.
Most detachment zones are located between 2600 and 3600 m, accounting for almost two thirds of all events. In contrast, the area between 2600 and 3600 m accounts for only 27% of the study area, showing that detachment zones are clearly overrepresented in this elevation band. If failures occurred proportionally to area, far fewer events would be expected there. Conversely, the 2000-2600 m band comprises 73% of the study area but hosts only 27% of the failures, indicating an underrepresentation of events at lower elevations. Above 3600 m, 13% of failures were recorded, even though this elevation range accounts for only 0.2% of the total area. These patterns show that rock slope failures do not occur randomly with respect to elevation but are

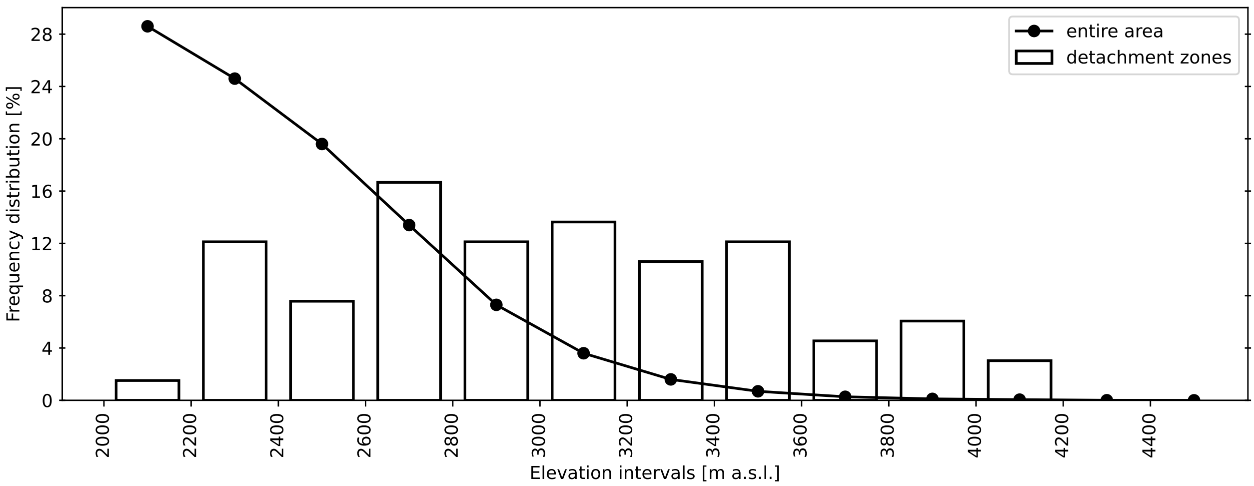

Figure 5: Frequency distribution of documented rock slope failures in the study area per 200 m elevation interval. The line indicates the relative proportion of the study area within each elevation band.

guided by controlling factors. While a clear elevation dependence is evident, it is likely linked to other elevation-dependent conditions such as glacier coverage, permafrost occurrence and slope steepness, which are explored in later sections.
Looking at failure volumes in relation to elevation (Figure 6), no distinct trend is apparent. Failures of the smallest volumetric class were recorded in almost every elevation interval, and the larger volumetric classes are also present in most elevation bands. The largest failures (> 1'000'000 m^3) do not show a clear elevation dependence either, occurring both at relatively low elevations (2200-2600 m) and at elevations up to 4000 m. Therefore, there is no clear evidence that volume is dependent on elevation in this dataset, suggesting that failure magnitude is more strongly controlled by other factors, such as slope geometry or lithology.

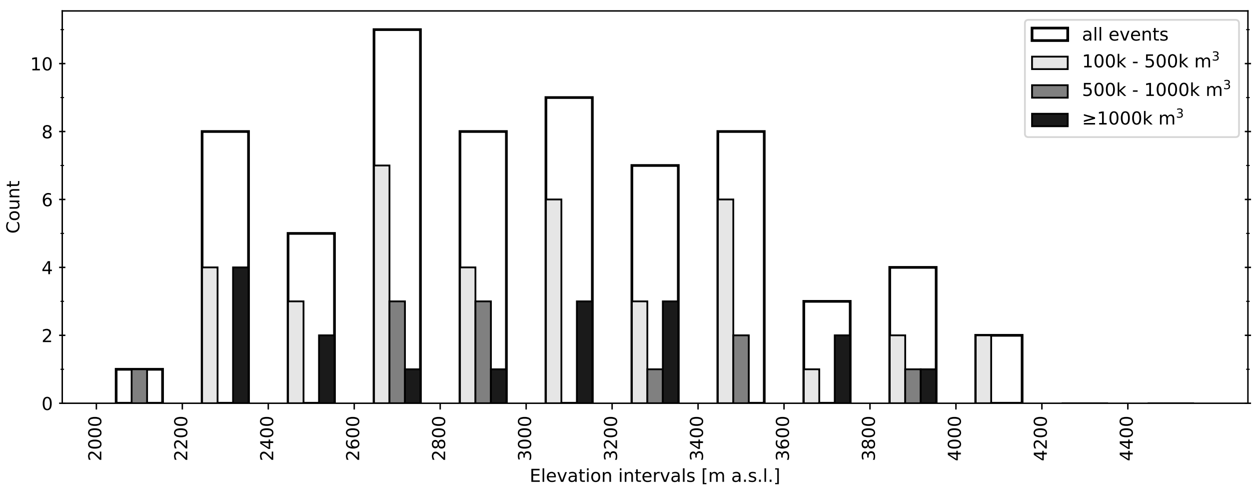

Figure 6: Number of documented rock slope failures per 200 m elevation interval, subdivided into three volume classes. White bars represent the total number of events and shaded bars show the contributions of individual volume classes.

4.3.2 Slope

Slope gradient is an important controlling factor for slope stability. Figure 7 shows the frequency distribution of documented rock slope failures by slope gradient, together with the relative extent of the study area across the same slope classes. The distribution reveals that most documented failures occurred between 40 and 60°, with 56 of 68 events falling within this range. Below 40°, only four events occurred, all between 30 and 40°. No events were documented below 30°, suggesting a lower threshold for rock slope failures in this setting around 30-35°. This lower threshold coincides with observations from other inventories, which estimate a critical slope angle of around 35° (Fischer et al., 2012, Noetzli et al., 2003). Rock slope failures also occur on very steep rockwalls (> 60°), although they are less frequent than at intermediate steepness. Only seven events were recorded at such steep slopes, which may reflect the limited areal extent of extremely steep rockwalls, the fact that many of these slopes are already strongly depleted or continuously shedding smaller volumes rather than producing large failures or that they are particularly stable.
The slope gradient distribution of the entire study area shows that most terrain has a gradient between 0 and 40°, accounting for 87% of the area, while slopes steeper than 40° represent only 13%. However, 93% of all failures occurred on slopes steeper than 40°, indicating a clear spatial

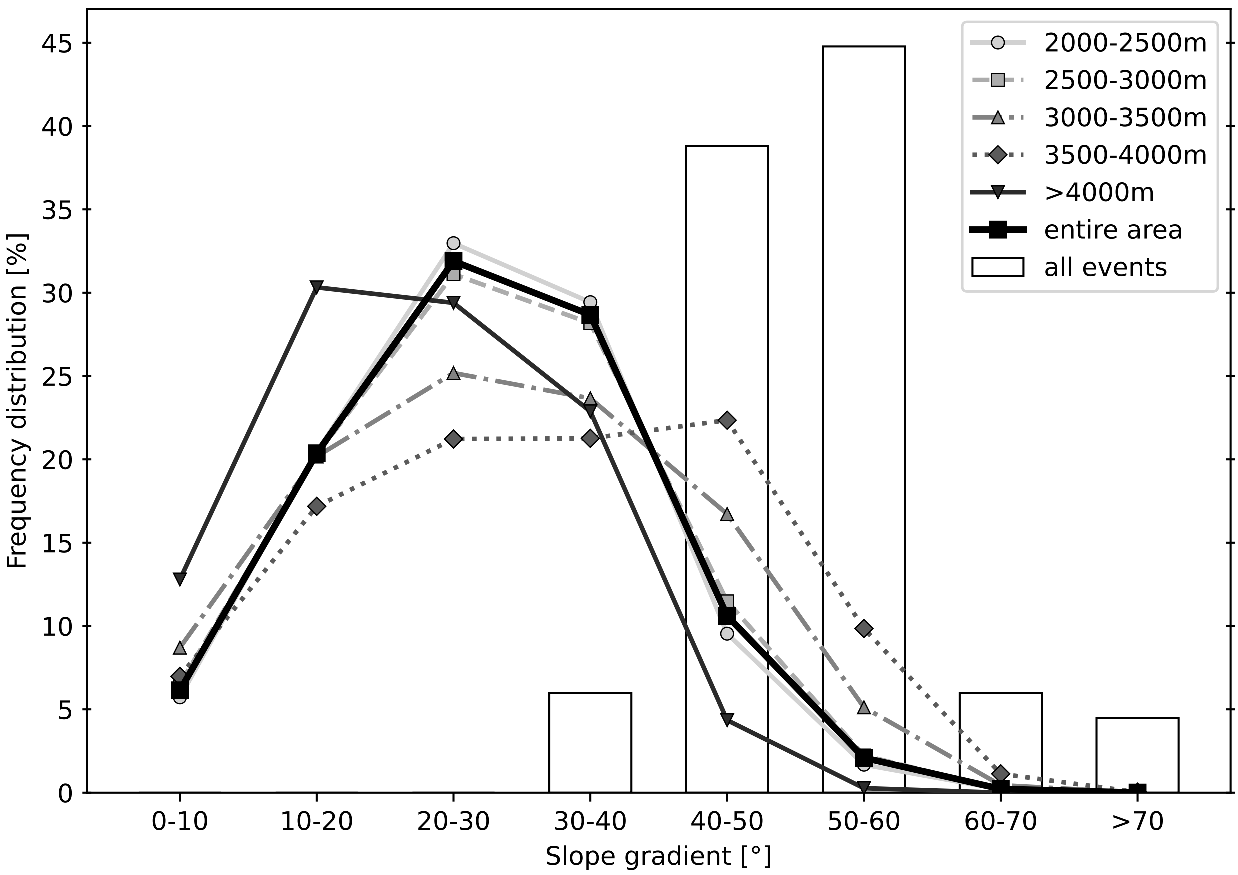

Figure 7: Frequency distribution of documented rock slope failures by slope gradient, compared with the relative extent of the study area across the same slope classes, shown as gray lines for individual elevation bands and a bold dashed black line for the entire study area.

mismatch between the study area and the detachment zones. This demonstrates that steep slopes, despite their limited areal extent, host a disproportionately large share of rock slope failures. This confirms that slope gradient is a primary control on detachment.
When examining slope gradient distributions for different elevation bands, the 2000-2500 m and 2500-3000 m intervals closely resemble the overall distribution, which reflects the fact that 93% of the study area lies below 3000 m. In contrast, the 3000-3500 m and 3500-4000 m elevation bands show fewer low-gradient areas and a higher frequency of steep slopes, with the 3500-4000 m band even peaking in the 40-50° class. This indicates that steep terrain becomes more prevalent at higher elevations, providing favorable conditions for rock slope failures. Nearly 50% of all documented rock slope failures occur between 3000 and 4000 m, where steep slopes are most frequent. Above 4000 m, slope gradients tend to be lower again, which can be explained by flatter, glacier-covered surfaces that provide fewer steep rock faces suitable for large detachment zones.
Figure 8 shows in which (a) elevation band and (b) volume class the documented rock slope failures occur. The relative contribution of different elevation bands within each slope class indicates no systematic relationship between the slope gradient of a detachment zone and its elevation. Rock slope failures with high and low slope gradients occur across all elevation bands. The only thing that stands out is that rock slope failure on very steep slopes (60-70°) seem to occur frequently at high altitudes.
The distribution by volume class suggests that the largest failures (> 1'000'000 m^3) are restricted to slope up to about 60° (with one exception), although the small sample size limits robust interpretation. Rock slope failures in the smallest volumetric class (100'000 - 500'000 m^3) predominantly occur at slopes steeper than 40°, whereas failures below 40° tend to involve larger volumes. This pattern may indicate that moderately steep slopes (30-40°) require larger failure volumes to reach instability, while steeper slopes (> 40°) can fail with smaller volumes. However, due to the small sample size these relationships remain weak and should be interpreted with caution.

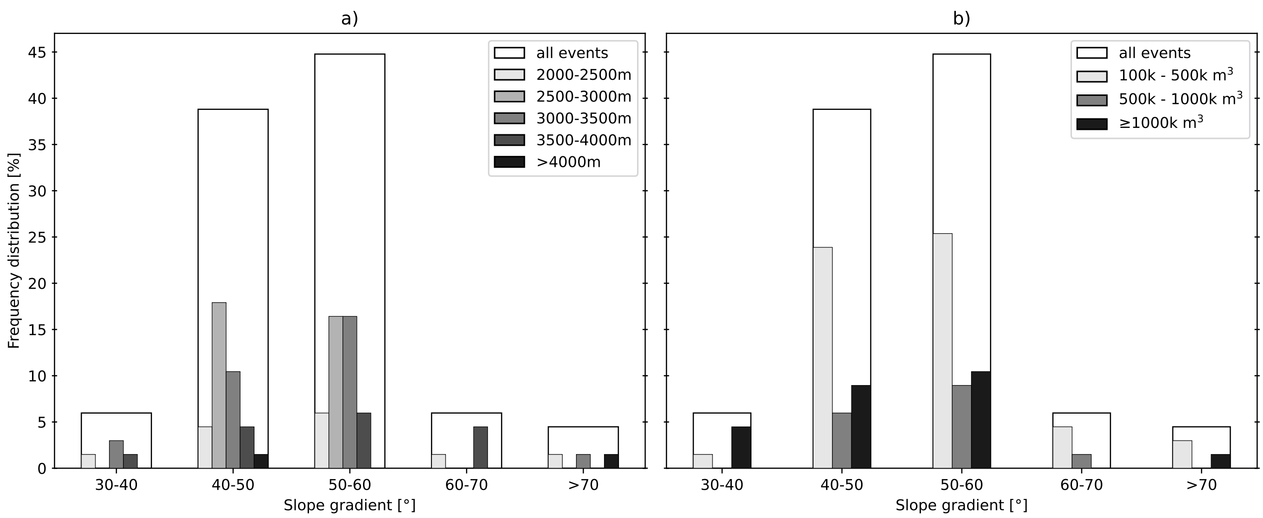

Figure 8: Frequency distribution of documented rock slope failures per slope gradient, subdivided by (a) elevation band and (b) volumetric class.

4.3.3 Aspect

The third topographic characteristic examined is aspect. The frequency distribution of documented rock slope failures (Figure 9) shows that failures occur on slopes of all aspects. However, the largest contribution comes from north-facing slopes, where a quarter of all failures occurred. North-eastern and north-western slopes account for another quarter, so that exactly half of all events are located on slopes with a northerly component (NW, N, NE). A notable number of failures also occurred on east- and west-facing slopes, whereas only three and two failures were documented on south-facing and south-west-facing slopes, respectively. This distribution suggests that rock slope failures do not occur randomly with respect to aspect, but tend to avoid south- and south-west-facing slopes and preferentially occur on slopes with a northerly component.
In comparison, aspects in the entire study area are approximately evenly distributed, with similar areal extents for all aspect classes (Figure 9). There is therefore a clear spatial mismatch between terrain aspect and the documented failures: north-facing slopes are overrepresented in the failure inventory, while south- and south-west-facing slopes are underrepresented. Failures on the remaining aspects occur with frequencies broadly consistent with their areal proportion. This pattern could reflect a combination of aspect-controlled factors, such as differences in solar radiation, permafrost occurrence and glacier extent, rather than aspect alone.
Figure 10 further illustrates the lack of failures on south-facing and south-west-facing slopes and the clustering on slopes with a northerly component, but also reveals patterns with elevation. At the highest elevations, failures predominantly occur on east-facing slopes (NE, E, SE). Similarly, failures at the lowest-elevation also predominantly cluster on east- and south-east facing slopes. Failures between 2500 and 3500 m occur predominantly on north-facing slopes (NW, N, NE) and, to a similar extent, on west-facing slopes. These patterns could suggest a relationship with the occurrence and degradation of permafrost and are discussed in more detail in section 4.5.2.

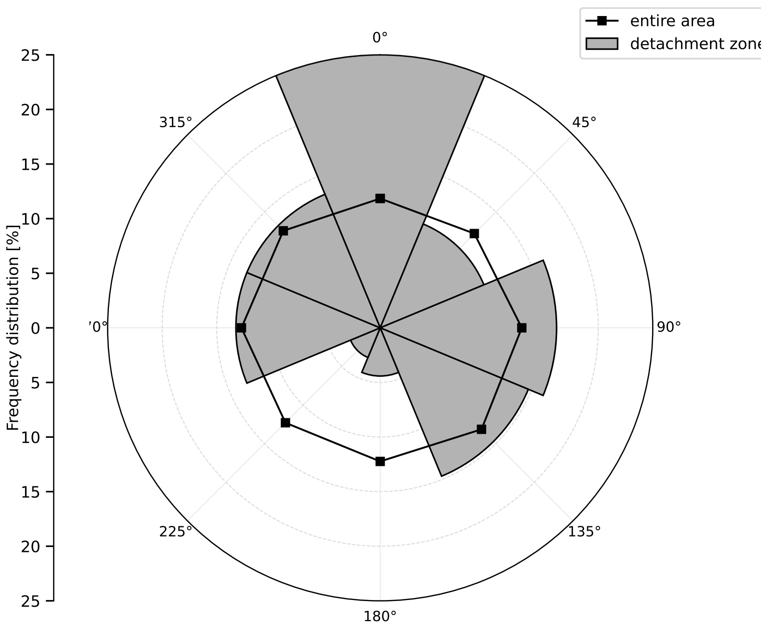

Figure 9: Aspect frequency distribution of detachment zones and entire study area

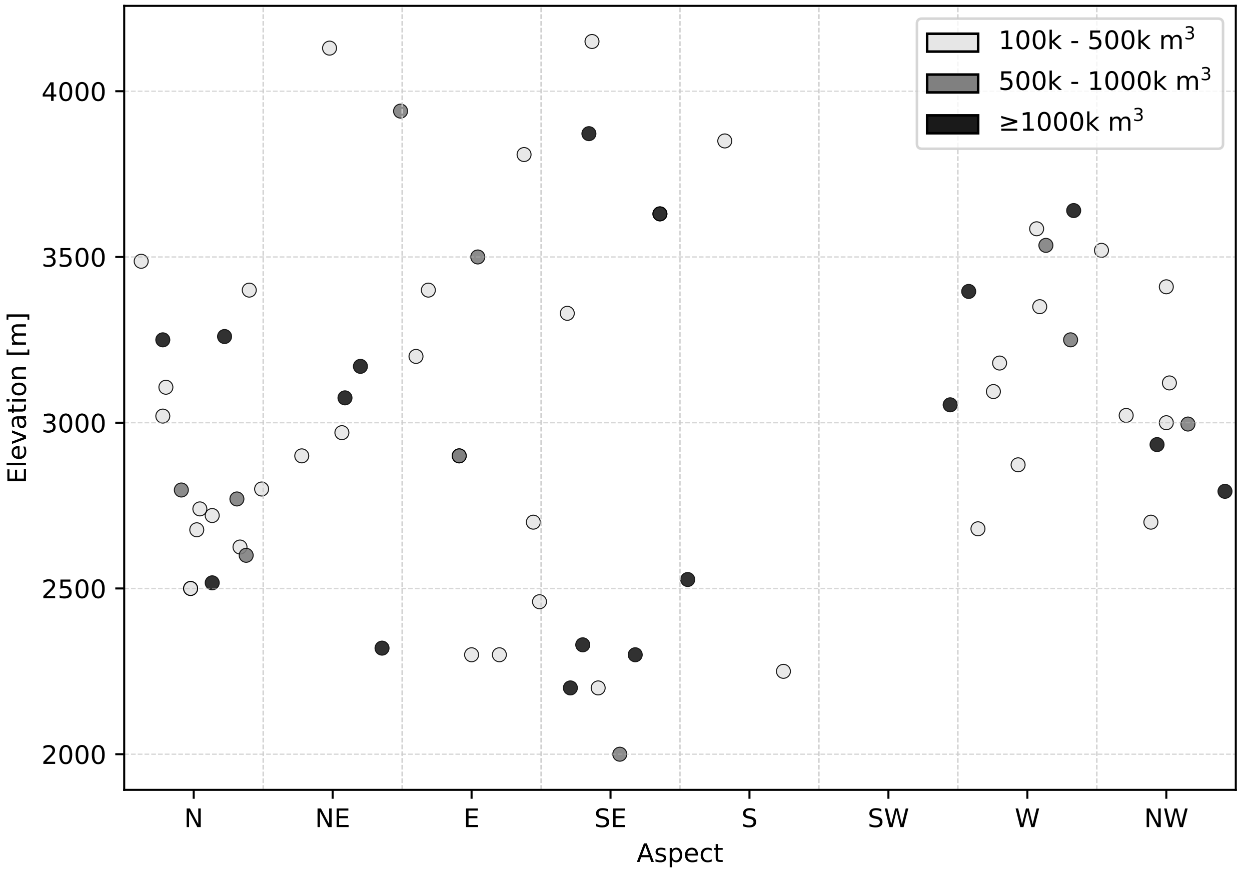

Figure 10: Elevation of detachment zones related to slope aspect, in relation to the failure volume.

The aspect of the detachment zones does not appear to influence failure volume. Rock slope failures of both the smallest and the largest volumetric classes occur on slopes of all orientations, and no systematic clustering of small or large events on particular aspects is evident (Figure 10). This suggests that, in this dataset, aspect primarily affects the likelihood of failure occurrence rather than the magnitude of the resulting rock slope failures.

4.4 Lithology

As mentioned in section 3.4, the overall distribution of lithological classes was obtained from Fischer et al. (2012). The fact that their lithological map does not cover the entire study area must be taken into account when interpreting the results.
Lithological analysis of the study area (from Fischer et al. (2012)) shows that the different classes are not equally distributed, either across the entire area or across different elevation bands (Figure 11). Across the entire area, lithology is dominated by *gneiss* (~39%), *limestone/dolomite* (~27%) and *schist* (~16%), whereas the classes *granit/diorit* (~9%), *mafic metamorphic* (~7%) and *conglomerate* (~2%) are less frequent. The distribution of lithological classes below 3000 m is very similar to the overall distribution, with only minor differences, which is expected because most of the study area is below 3000 m. Above 3000 m, however, the proportions change considerably: the relative share of *gneiss* and *mafic metamorphic* rocks

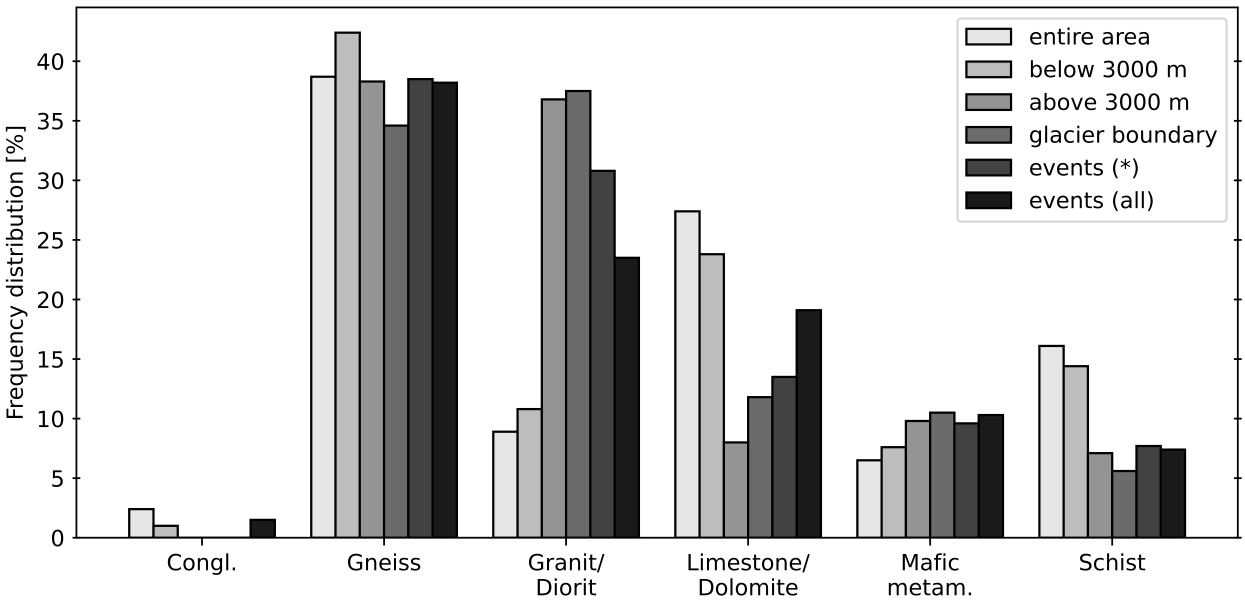

Figure 11: Frequency distribution of lithological classes in the study area, at different elevation bands and along glacier boundaries, compared to the distribution of rock slope detachment zones, where (*) refers to only the rock slope failures inside the study area of Fischer et al., 2012, and (all) refers to the documented rock slope failures in this study.

remains similar to that of the entire area, but the proportion of *granit/diorit* increases to nearly 37%, while *limestone/dolomite* and *schist* decrease to ∼8% and ∼7%, respectively. The distribution of lithological classes along glacier boundaries (defined as within 100 m of the glacier edge) closely resembles the >3000 m distribution, with only minor deviations, such as a slightly lower proportion of *gneiss* and a slightly higher proportion of *limestone/dolomite*. This indicates that high-elevation and glacier-proximal terrain is distinctly more granitic and less carbonate- and *schist*-dominated than the study area as a whole.

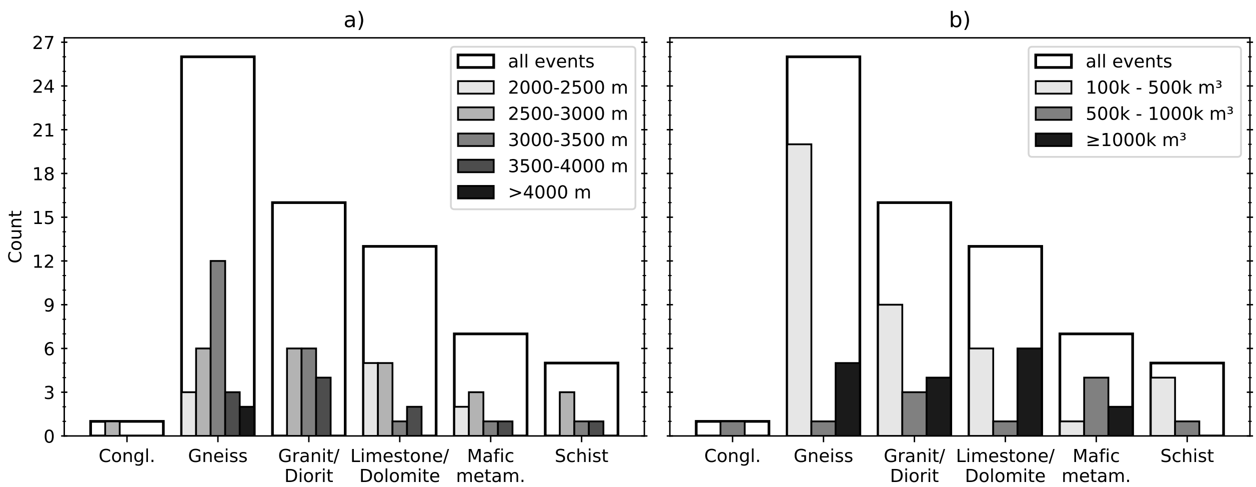

Figure 12: Number of documented rock slope failures per lithological class, subdivided by (a) elevation band and (b) volumetric class.

The distribution of detachment zones inside the study area (from Fischer et al. (2012)) shows that most documented failures occurred in *gneiss* (∼38%), followed by *granit/diorit* (∼30%) and *limestone/dolomite* (∼13%). Events in the other lithologies are less frequent, with each of the remaining classes representing <10% of all failures. Comparing this distribution to the areal proportions reveals that *granit/diorit* slopes are overrepresented among failures (∼30% failures versus ∼9% area), whereas *limestone/dolomite* (∼13% failures versus ∼27% area) and *schist* (∼8% failures verus ∼16% area) are underrepresented. Including the documented rock slope failures outside the area covered by the Fischer et al. (2012) lithology map does not change this pattern significantly, apart from a slight decrease in the relative share of failures of *granit/diorit* (− ∼6%) and a slight increase in *limestone/dolomite* (+ ∼6%).
The joint analysis of lithology and elevation (Figure 12a) shows that failures across all elevation bands occur in almost all lithological classes. The elevation distribution of failures in *limestone/dolomite* and *schist* tends toward lower elevations, consistent with their predominance below 3000 m, whereas *granit/diorit* failures occur more frequently at higher elevations and less often at lower elevations, reflecting the strong increase of *granit/diorit* above 3000 m. Overall, these patterns largely mirror the underlying lithological zonation with elevation, suggesting that lithology-elevation trends in failures mainly reflect the distribution of rock types rather than a distinct elevation control within individual lithologies.
Comparing failure volumes across lithological classes (Figure 12b) suggests no systematic relationship between lithology and failure size. Most lithological classes (*gneiss*, *granit/diorit*, *schist*) are dominated by smaller failures (100'000-500'000 m^3), and all classes include events from multiple volume ranges. Failures with *limestone/dolomite* and *mafic metamorphic* lithology exhibit relatively higher proportions of large-volume failures, which might hint at a tendency for these lithologies to host larger instabilites. However, the small number of events in these classes limits robust interpretation.

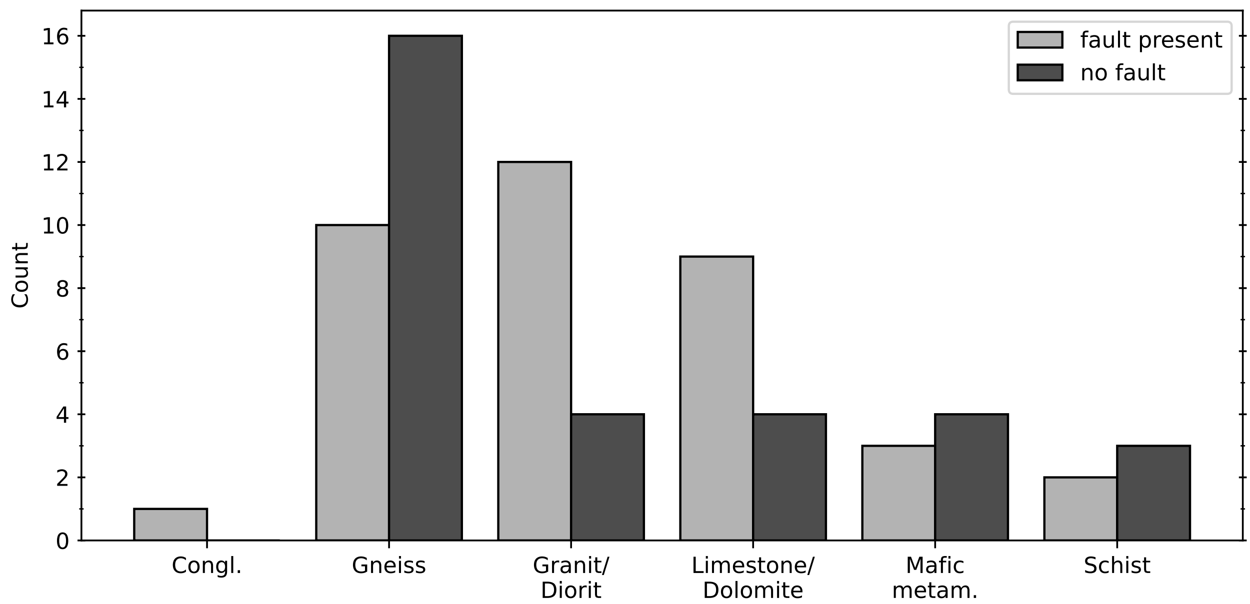

Figure 13: Number of documented rock slope failures per lithological class with a tectonic fault in proximity and without a mapped fault in proximity.

Figure 13 shows the number of failures with and without a known fault in proximity for each lithological class. Across all lithologies, 37 failures (∼54%) have a fault present and 31 (∼46%) do not. This proportion varies between lithological class: *gneiss*, *mafic metamorphic* and *schist* more often host failures without a nearby known fault, whereas *granit/diorit* and *limestone/-dolomite* more frequently show a fault in proximity than the overall distribution would suggest. As no information is available on the spatial density of tectonic faults across the entire study area and within each lithological class, these patterns cannot be directly translated into fault-related susceptibility differences. Nevertheless, the frequent coincidence of failures and faults in certain lithologies is consistent with the role of major discontinuities and fracture zones as important preconditioning factors and potential triggers for large rock slope failures.

4.5 Cryosphere

4.5.1 Glaciers

Large areas above 2000 m have been affected by changes in glacier extent since the Little Ice Age (LIA). Analysis of glacier extent at 1850 (Reinthaler & Paul, 2025) and 2015 (Paul et al., 2020) reveals that over the entire study area, glacier cover decreased drastically: while glaciers covered ∼4190 km^2 at the LIA, they occupied only ∼1799 km^2 in 2015, corresponding to a relative glacier loss of ∼57%. Glaciers covered nearly ∼12% of the study area at the LIA and now cover only about ∼5%. Figure 14 shows, that glacier retreat was proportionally largest at lower elevations between 2000 and 3000 m, with relative losses between ∼84% (2000-2200 m) and ∼59% (2800-3000 m). At higher elevations, relative glacier loss was less pronounced but still relevant, with reductions between ∼36% (3000-3200 m) and ∼5% (4200-4400 m). Above

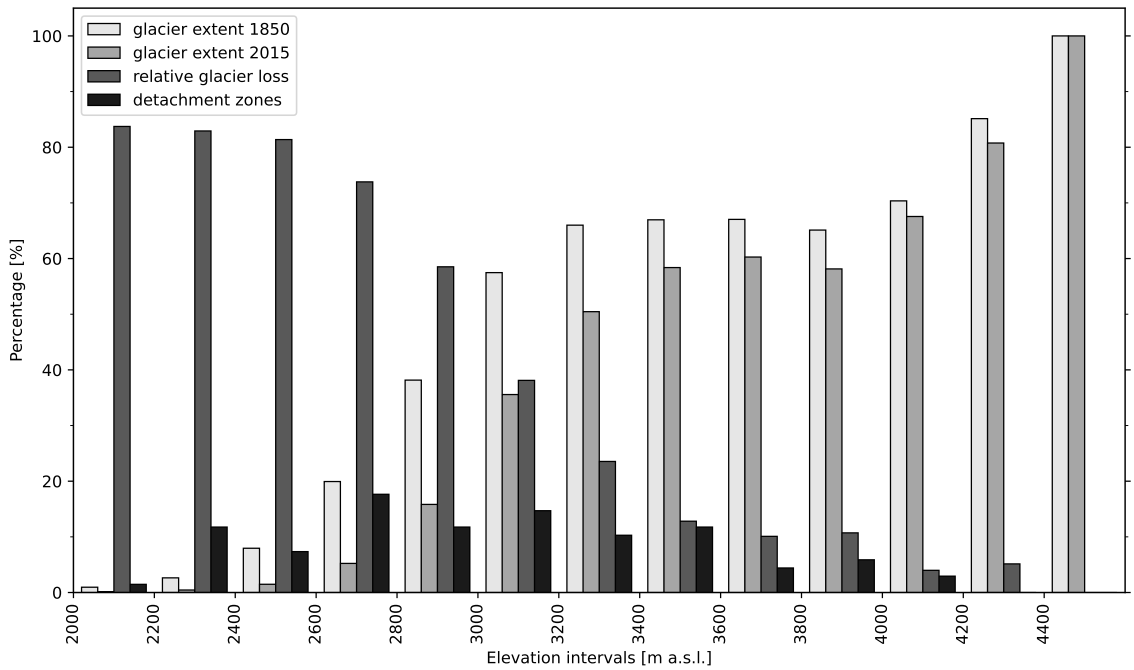

Figure 14: Glacier cover in 1850 (LIA) and 2015, relative glacier loss, and relative frequency of detachment zones by elevation bands.

4400 m, no glacier loss was recorded, with glacier extent remaining at 100% both in 1850 and 2015. As this corresponds to a very small area (~0.018 km^2), changes may be below the mapping resolution. Overall, it can be stated that proportional glacier loss decreases with elevation, with the inverse being true for relative glacier cover. Furthermore, due to the spatial extent of the different elevation intervals, as shown in figure 5, the absolute extent of glacier losses, was highest below 3000 m, with losses of nearly 2000 km^2, while above 3000 m only ~400 km^2 of area was lost, equivalent to 83% and 17% of the total glacier area loss respectively.
If we compare the elevation distribution of glacier loss with the elevation of the detachment zones (Figure 14), there is no clear evidence for a simple relationship. The highest relative and absolute glacier losses occur below 3000 m, whereas glacier cover at higher elevations has decreased less strongly. Despite this, 50% of failures occurred below and 50% above 3000 m, indicating that detachment zones are not concentrated in the elevation bands with the strongest glacier retreat. This suggests that glacier retreat alone does not control the elevation distribution of rock slope failures and that other factors, such as slope gradient, aspect and permafrost conditions, play a more important role.
The influence of glaciers at each detachment zone was classified into four classes. Figure 15 shows the glaciation state of the detachment zones and the relative contribution of the three volumetric classes. Of the 68 documented events, 25 events (~37%) were classified as not influenced by glaciers and 43 events (~63%) as influenced by glaciation or deglaciation. Despite glaciers covering only about 11% of the study area around 1850 and about 5% in 2015, a majority of documented rock slope failures show some form of glacier influence. Detachment zones affected by glaciation were further subdivided into sites with a glacier at the base of the slope (26 events, ~38%), sites with a glacier within the slope (13 events, ~19%) and detachment zones that were recently exposed following glacier retreat (4 events, ~6%).
The distribution of volumetric classes across the four glaciation states indicates no strong re-

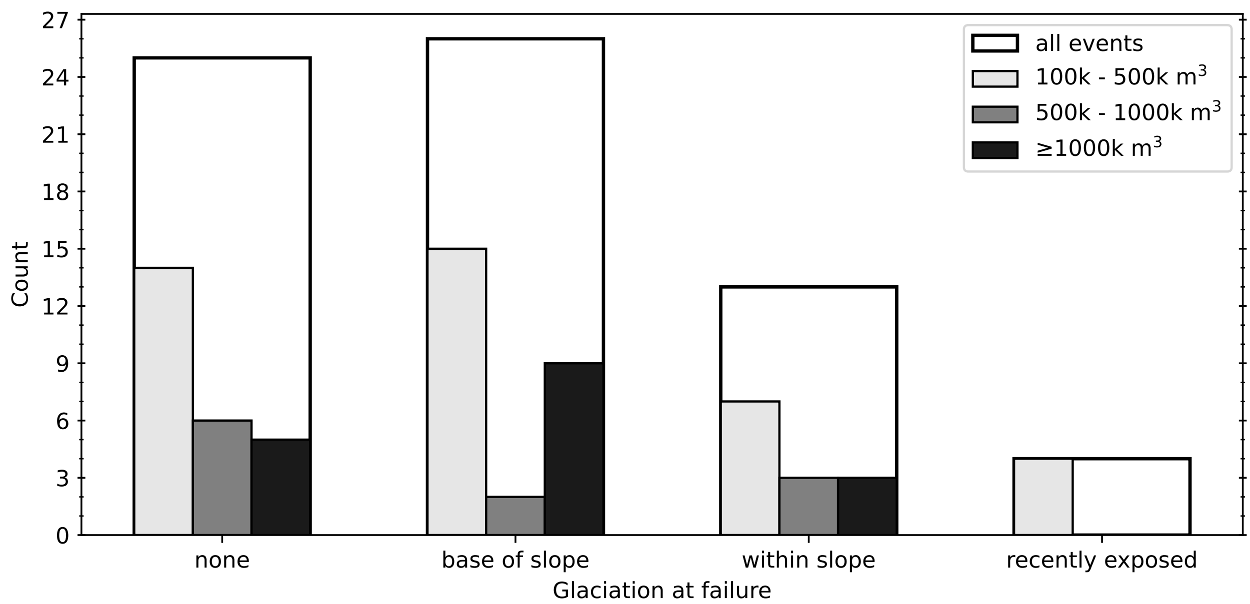

Figure 15: Number of documented rock slope failures per glaciation class, subdivided by volumetric class.

lationship between failure volume and glacier adjacency. For failures both with and without glacier influence, all volumetric classes are represented, suggesting that glacier presence or recent retreat does not systematically control failure size in this dataset (Figure 15). Only detachment zones that were recently exposed show exclusively failures of the smallest volumetric class, which may indicate that these slopes are still in an early adjustment phase and have not yet developed larger-scale instabilities. However, given the small number of events in this category, this interpretation remains tentative.

Including the lithological setting into the glacier influence analysis (Figure 16) reveals that glacier-related instabilities are not uniformly distributed across the lithological classes. While *gneiss* and *granit/diorit* are dominated by glacier-adjacent failures, with a large proportion of events occurring on slopes that are or were in contact with ice, the other lithological classes show a higher share of failures without direct glacier influence. This indicates that *gneiss* and *granit/diorit* may be particularly sensitive to glacial erosion and debuttressing, whereas the other lithologies may accommodate glacial loading and unloading more effectively, resulting in fewer rock slope failures. However, potential area- and elevation-dependent relationships still need to be explored before drawing firm conclusions, and these aspects will be addressed in the discussion section.

Overall, the results indicate that glaciers and glacier retreat are important in conditioning or triggering rock slope failures, as most events occur on slopes that are or were in contact with ice, even though glaciers occupy only a small fraction of the study area. The absence of a clear link between failure elevation and the strongest bands of glacier loss suggests that the response of rock slopes to deglaciation is modulated by additional factors such as slope gradient, lithology and permafrost degradation, and may involve considerable time lags between ice retreat and failure. Together, the spatial patterns of glacier influence and lithology imply that both rock type and cryospheric history are key in determining which slopes ultimately fail and which remain stable.

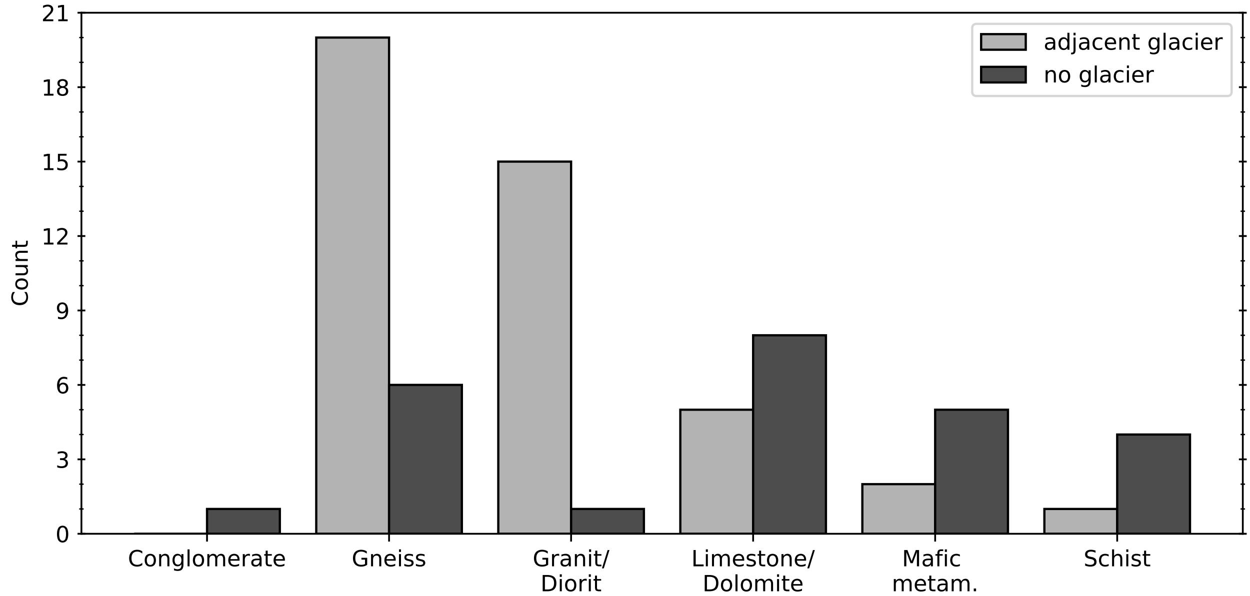

Figure 16: Glaciation situation at failure time of documented rock slope failure for the different lithological classes.

4.5.2 Permafrost

Permafrost conditions at the detachment zones, as derived from the APIM classification and the validation procedure described in the methodology section, are shown in Figure 17. It displays, similarly to Figure 10, altitude versus aspect for each detachment zone and the APIM-based permafrost classification of each failure. Additionally the zones, where permafrost is probable in 1980, according to the PERMAKART model are indicated. Furthermore, the estimated lower permafrost boundary at the LIA (1850) is indicated, estimated from the PERMAKART model, estimating a ∼2 °C increase in temperature. Detachment zones classified as "no permafrost" by APIM are all located below the 1980 PERMAKART lower boundary, and cross-checking with the literature supports this assessment for most of these failures. Only two events, Val Pola and Rawilhorn (PERMOS, 2025), show indications of permafrost in the literature despite being classified as "no permafrost". For failures below the PERMAKART boundary but classified as permafrost-affected by APIM, literature information supports the presence of permafrost in two out of three cases. This suggests that permafrost can be present locally even below the lower limit predicted by PERMAKART. In addition, all failures located above the PERMAKART lower boundary are classified as permafrost-affected in APIM, indicating good consistency between the two models. Together, these comparisons suggest that both models tend to underestimate permafrost presence in some cases. Moreover, for events that occurred outside 1980 permafrost conditions, permafrost presence at the time of failure cannot be excluded, as is shown by the 1850 lower boundary. Furthermore, temperature changes at depth, which are not resolved by surface-based permafrost models, could also influence slope stability. Based on this evaluation, detachment zones in the three APIM categories "permafrost in nearly all conditions", "permafrost mostly in cold conditions" and "permafrost only in very favorable conditions" are all treated as permafrost-affected in subsequent analyses.

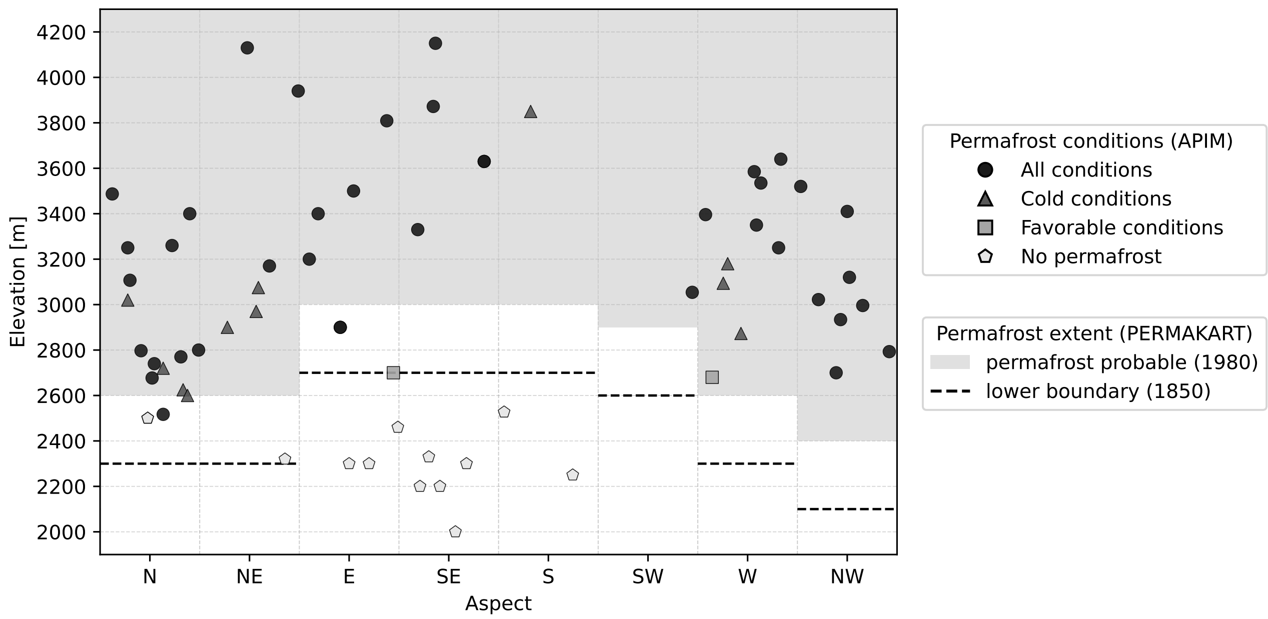

Figure 17: Elevation of detachment zones related to slope aspect, in relation to the modeled permafrost at each individual slope failures and the assumed lower permafrost boundary (Keller, 1992).

The distribution of failures with respect to aspect was discussed in section 4.3.3. The addition of permafrost information shows that events without permafrost predominantly occur on east- and south-east-facing slopes, whereas the cluster of failures on north- and north-east-facing slopes is concentrated near the lower permafrost boundary (Figure 17). Figure 10 indicated that failure volume does not show a clear dependence on aspect or elevation; combined with the permafrost classification, this suggests that large failure volumes occur both with and without permafrost and that, in this dataset, permafrost presence does not systematically control failure size.
The frequency distribution of detachment zones relative to the entire study area shows that most failures occur in permafrost conditions, whereas most of the area is free of permafrost (Figure 18a). Only 13 events (∼20%) occurred outside modern permafrost conditions, while 53 events (∼80%) occurred on permafrost-affected slopes. Over the entire study area, however, ∼63% of the area is classified as having no permafrost and only ∼37% as having permafrost. Thus, failures in permafrost terrain are strongly overrepresented relative to area, whereas failures without permafrost are underrepresented. Because the proportion of area with permafrost increases with elevation, from ∼5% between 2000 and 2200 m to over 95% between 3000 and 3200 m, most of the non-permafrost area is located below 3000 m, whereas almost all terrain above 3000 m is permafrost-affected. Since a large fraction of the documented failures occurs above 3000 m, this elevation dependence of permafrost extent explains part of the spatial mismatch between the distribution of failures and the distribution of permafrost terrain. At the same time, steep rockwalls and glacier-proximal slopes are also more frequent at high elevations, so the elevated failure density in permafrost terrain likely reflects a combination of permafrost presence, slope gradient and glacial conditioning rather than permafrost alone.
Permafrost presence in relation to lithological classes (Figure 18b) shows that, for all lithologies, more failures occur under permafrost conditions than outside them. Only for the *limestone/dolomite* class are nearly as many failures located outside permafrost as within, which is consistent with the tendency of *limestone/dolomite* failures to occur at lower elevations where permafrost is rare (12a). Lithology therefore does not appear to exert a strong additional control on permafrost occurrence at detachment sites, beyond its indirect influence via elevation.

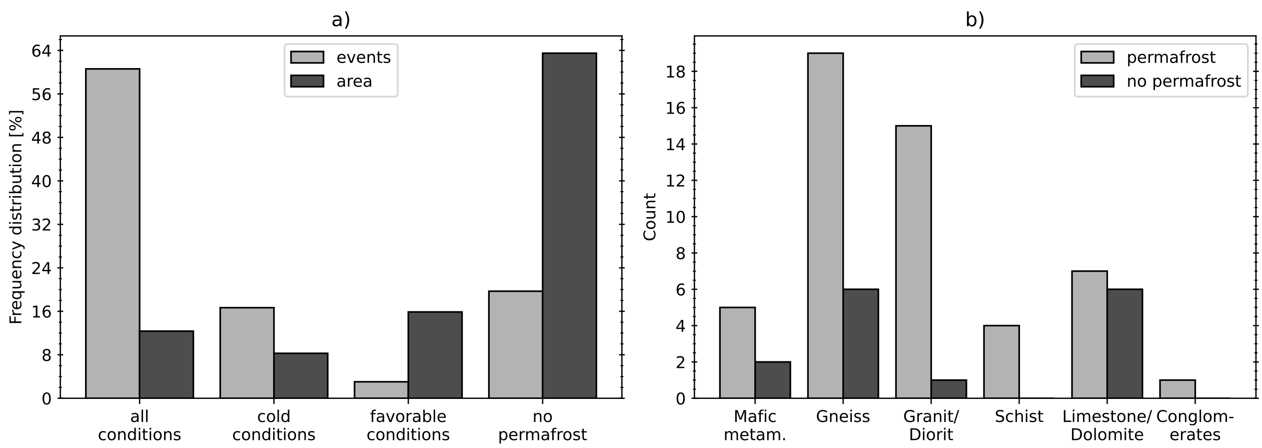

Figure 18: (a) Frequency distribution of permafrost conditions in the study area and at rock slope detachment zones. (b) Permafrost situation of documented rock slope failures for the different lithological classes.

There is also no indication that any particular lithological class is systematically more prone to failure under permafrost conditions than others. Overall, the results highlight that permafrost is an important conditioning factor for rock slope failures in the study area. The data alone are insufficient to demonstrate whether permafrost by itself is a necessary or sufficient cause of failure, but the strong association with elevation, steep slopes and glacier proximity suggests that a combination of these factors, rather than permafrost alone, is the most likely explanation for the observed pattern.

4.6 Climatology

4.6.1 Air temperature

Mean and maximum air temperature metrics exhibit strong similarity in characterizing thermal extremes preceding rock slope failures. Percentile ranks for window-mean temperatures differ minimally between maximum and mean metrics, with maximum-minus-mean differences ranging from -0.002 (1d) to -0.031 (90d). Similarly, counts of extremely warm days (daily temperatures $\geq$95th percentile) are consistently higher for maximum than mean temperatures, reflecting maximum temperature's heightened sensitivity to daily thermal peaks.
The two primary metrics, percentiles (window-mean intensity relative to 1961-1990 climatology)

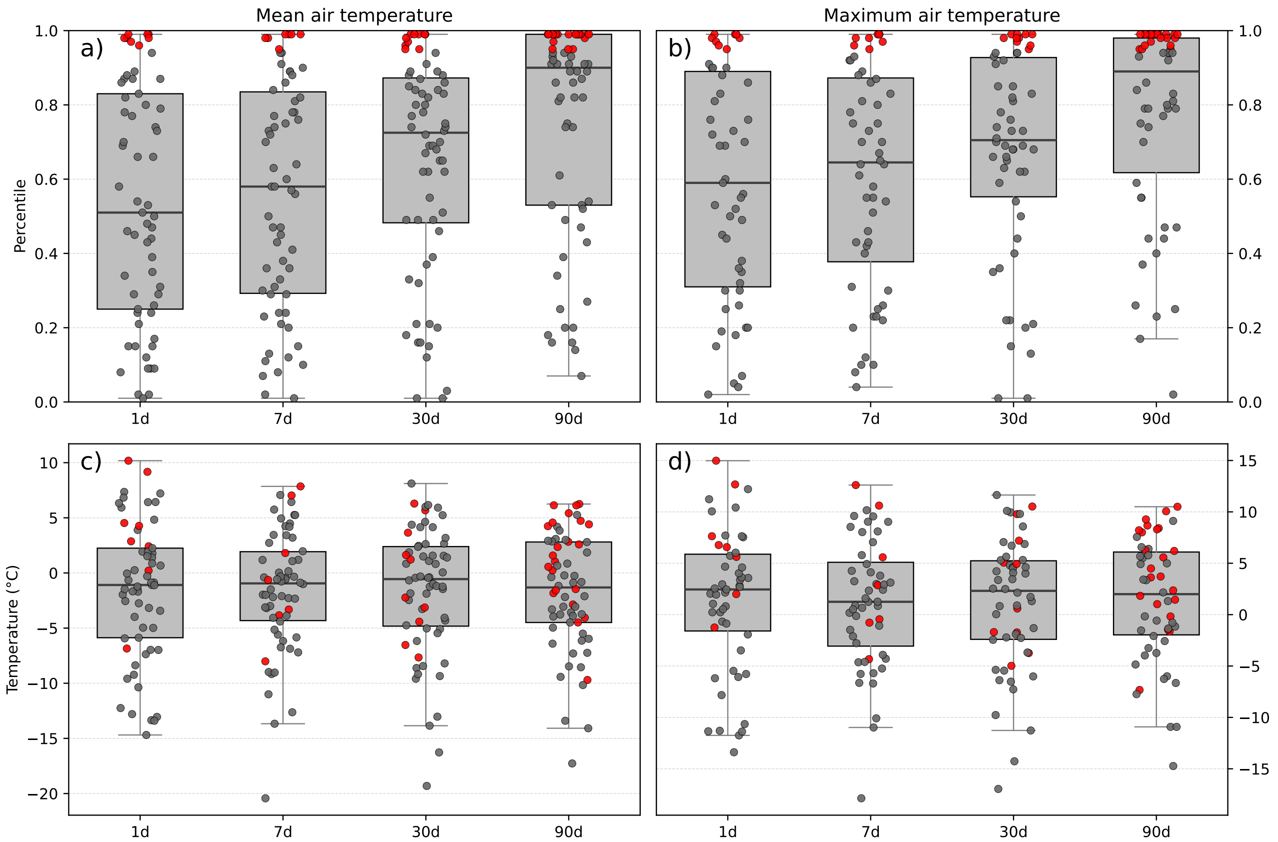

Figure 19: Air temperature percentiles and absolutes in windows before documented slope failures. Events above the 95th percentile are highlighted in red. a) Distribution of mean air temperature percentiles. b) Distribution of maximum air temperature percentiles. c) Distribution of mean absolute air temperatures. d) Distribution of maximum absolute air temperatures.

and warm day counts (frequency of individual extreme days), demonstrate high concordance, with ∼85% overlap in identifying extreme events across all windows and temperature types. Discrepancies (10-15% of events) typically involve warm day thresholds exceeded without the corresponding window-mean temperature reaching the 95th percentile, while the reverse is rarer.

Due to maximum temperature data gaps affecting ∼15% of events, mean temperature was prioritized for primary visualizations and analyses to maximize sample size and statistical robustness, with negligible information loss given the metrics' tight equivalence.

Air temperature percentile distributions shift progressively toward warmer extremes with longer antecedent windows, while remaining broadly comparable between mean and maximum temperatures (Figure 19a,b). For mean temperature, shorter windows exhibit near-random distributions with a median at the ∼50th percentile at 1 day, shifting to the ∼90th percentile median at 90 days. The fraction of extreme events (≥95th percentile) accordingly increases from ∼13% (8/61 events) at 1 day to ∼34% (22/64 events) at 90 days. Maximum temperature displays parallel tendencies (∼18% or 9/51 at 1 day to ∼39% or 21/54 at 90 days), albeit with slightly elevated extreme proportions due to its post-1960 skew.

This marked temporal progression toward extremes in longer windows suggests that prolonged antecedent warmth may precondition slopes for instability, either climatically (post-1980/2000 amid regional warming) or mechanistically (via cumulative thermal stress). Shorter windows show no such signal, likely due to inherent lag times in thermal-permafrost responses or because sustained rather than acute heat is required. Notably, ∼40-60% of events across metrics experience normal or below-median temperatures, underscoring air temperature as a permissive rather than deterministic factor.

Absolute temperature distributions (Figure 19c,d) appear broadly random across windows, with stable medians of ~ -1 °C (mean temperature) and ∼2 °C (maximum temperature). Approximately 40% of mean temperature events and 57-69% of maximum temperature events exceed 0 °C, with fractions holding steady regardless of window length. Distributions narrow for longer periods due to averaging effects, yet prominent negative outliers persist. Of note, ≥95th percentile events, highlighted in red, disperse across both positive and negative values in short windows but increasingly cluster at elevated positives in longer windows, particularly the 90-day window, reinforcing the role of net antecedent warmth.

Warm day counts, visualized using mean temperature for completeness ((Figures 20, 21), echo the percentile trends: exceedance frequency escalates from ∼13% at 1 day (8/61 events) to nearly 50% at 90 days (30/64 events). Temporally, extremes cluster post-2000 (none pre-1980), with exceedance ratios surging from ∼11% pre-2000 to 14% (1d), 24% (7d), 36% (30d), and 67% (90d) post-2000, potentially signaling climatic warming, improved detection in recent decades, or both.

No clear pattern links thermal extremes to failure volumes across windows, as both small (<500k m^3) and large (>1000k m^3) events show exceedances. Intriguingly, the smallest and largest-volume class exhibit unusually high 90-day exceedances, while intermediate classes show lower rates, though small sample sizes preclude firm conclusions for larger volumes.

Seasonally, threshold exceedances occur across all quarters but peak strikingly in spring (∼44% for 7/30-day; ∼67% for 90-day), contrasting winter minima (<20% across windows). Summer and autumn ratios are intermediate (∼20-25% for 7/30-day; ∼50-60% for 90-day), suggesting spring melt-thaw cycles amplify antecedent warmth to critical destabilization, while winter insulation mutes the signal.

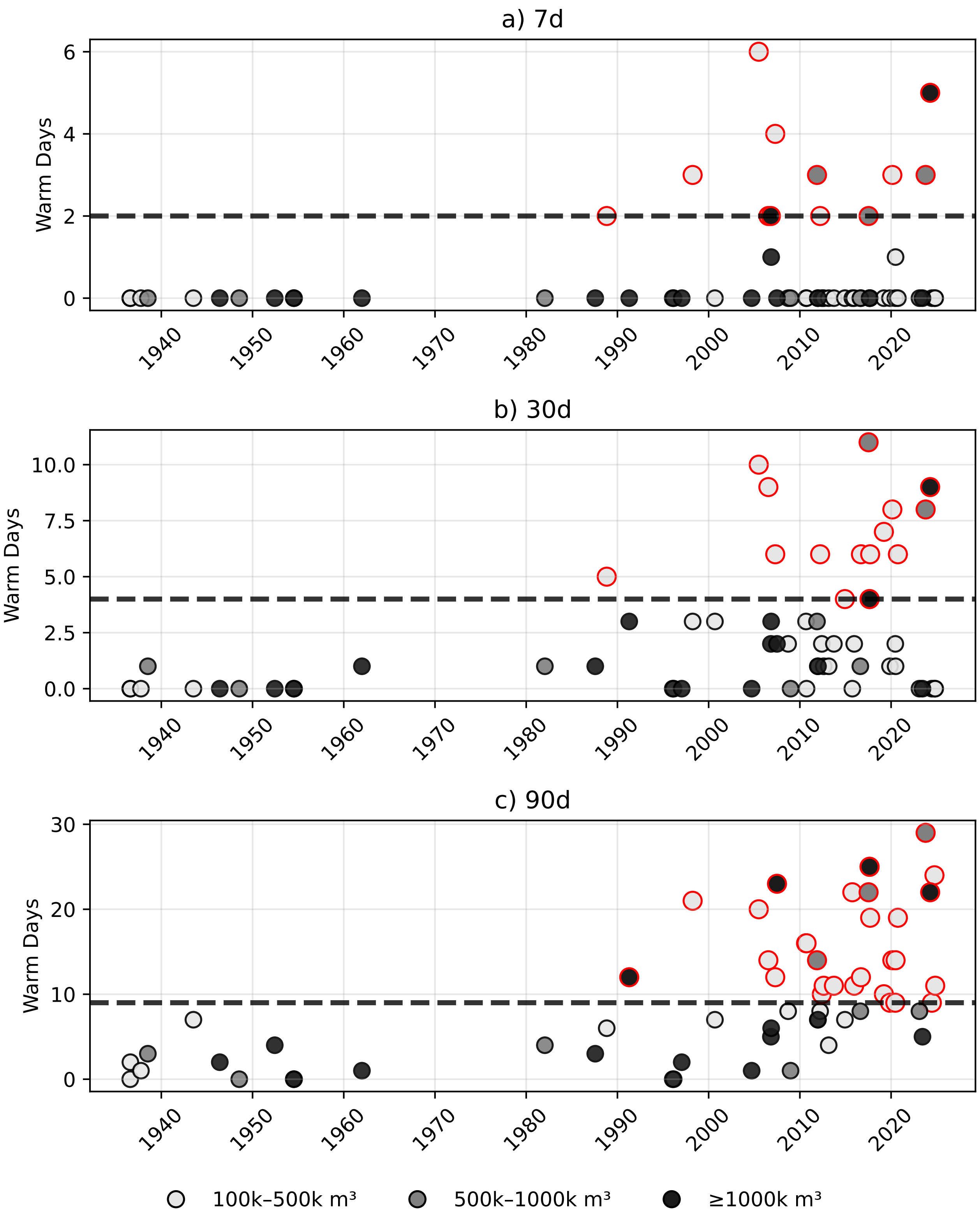

Figure 20: Temporal distribution of warm days (mean air temperature) preceding rock slope failures (7d, 30d, 90d windows). Dashed lines denote thresholds and events exceeding it are highlighted in red.

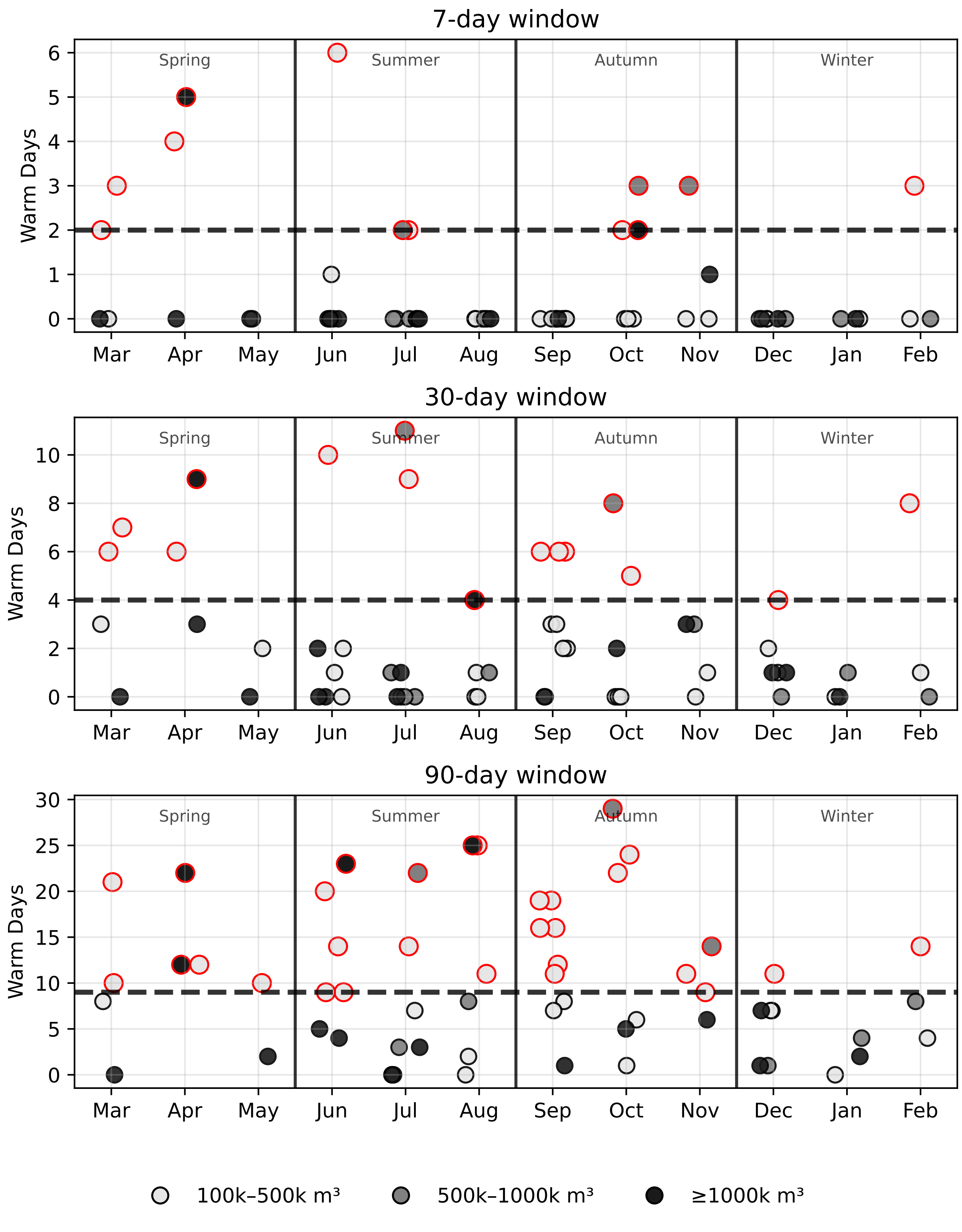

Figure 21: Seasonal distribution of warm days (mean air temperature) preceding rock slope failures (7d, 30d, 90d windows). Dashed lines denote thresholds and events exceeding it are highlighted in red.

Overall, these patterns position antecedent air temperature as a key modulator in cryosphere-proximal failures, likely via prolonged thaw accelerating permafrost degradation or ice-loss weakening, rather than a direct failure trigger.

4.6.2 Freeze-thaw cycles

Table 2 summarizes the observed trends in FTC counts at four high elevation weather stations, both annually and seasonally.
Annually, Jungfraujoch (3571 m) and Col du Grand St-Bernard (2472 m) show statistically significant increases of +0.53 and +0.44 FTC days per year, respectively. At Weissfluhjoch (2691 m) and Andermatt Gütsch (2286 m), no significant trends are detected, with a slight decrease (−0.13 d/yr) at Weissfluhjoch and a weak, statistically non-significant increase (+0.06 d/yr) at Andermatt Gütsch. This trend is also clearly visible in Figure 22, with the yearly FTC magnitude trending upwards for the Jungfraujoch and Col du Grand St-Bernard.
Average annual FTC counts are similar across Col du Grand St-Bernard, Weissfluhjoch, and Andermatt Gütsch (roughly 80-100 days per year). However, only Col du Grand St-Bernard exhibits a marked upward trend, rising from ∼80 days in the 1960s to >100 days in recent decades, while the others remain relatively stable around 90-95 days, respectively. At Jungfraujoch, counts start significantly lower (∼70 days in the early 1960s) but increase to >100 days today, now exceeding Weissfluhjoch and Andermatt Gütsch.
Overall, the annual FTC signal is heterogeneous across stations. This pattern reflects elevation-dependent responses to warming: high-elevation sites, such as the Jungfraujoch, that were previously too cold to cross 0 °C gain FTCs as temperatures rise into a transitional range, while some lower sites experience fewer FTCs as days remain more consistently above freezing. However, elevation alone does not fully explain the trends, as Col du Grand St-Bernard records an increase in FTC days, despite being at a similar elevation as Weissfluhjoch and Andermatt Gütsch. Local climate differences, station exposure and varying observation periods could also contribute to this spatial variability.
Seasonally, distinct patterns emerge both between stations and across seasons (Figure 23.
In autumn (SON), FTC counts remain remarkably stable across all four stations (∼30 days per season), with only a slight, statistically significant increase at Jungfraujoch (+0.17 d/yr). Weissfluhjoch and Andermatt Gütsch show no trend, while Cold du Grand St-Bernard shows a statistically non-significant positive trend (+0.12 d/yr).
In winter (DJF), FTC counts increase at the three lower stations (Weissfluhjoch +0.06, Andermatt Gütsch, +0.14, Col du Grand St-Bernard +0.20 d/yr), whereas Jungfraujoch shows virtually no change and remains near zero FTC days throughout the record. These trends are

Table 2: Linear trends (increase/year) of Freeze-Thaw-Cycles count at the four high elevation weather stations used for temperature analysis. Values in bold indicate significance at the 95% level of confidence.

Station	Annual	DJF	MAM	JJA	SON	period
Jungfraujoch (3571 m)	**0.53**	**0.00**	**0.14**	**0.20**	**0.17**	1961-2024
Weissfluhjoch (2691 m)	−0.13	0.06	0.07	**−0.25**	0.00	1971-2024
Andermatt Gütsch (2286 m)	0.06	**0.14**	0.09	**−0.20**	0.00	1961-2024
Col du Grand St-Bernard (2472 m)	**0.44**	**0.20**	**0.17**	**−0.14**	0.12	1965-2024

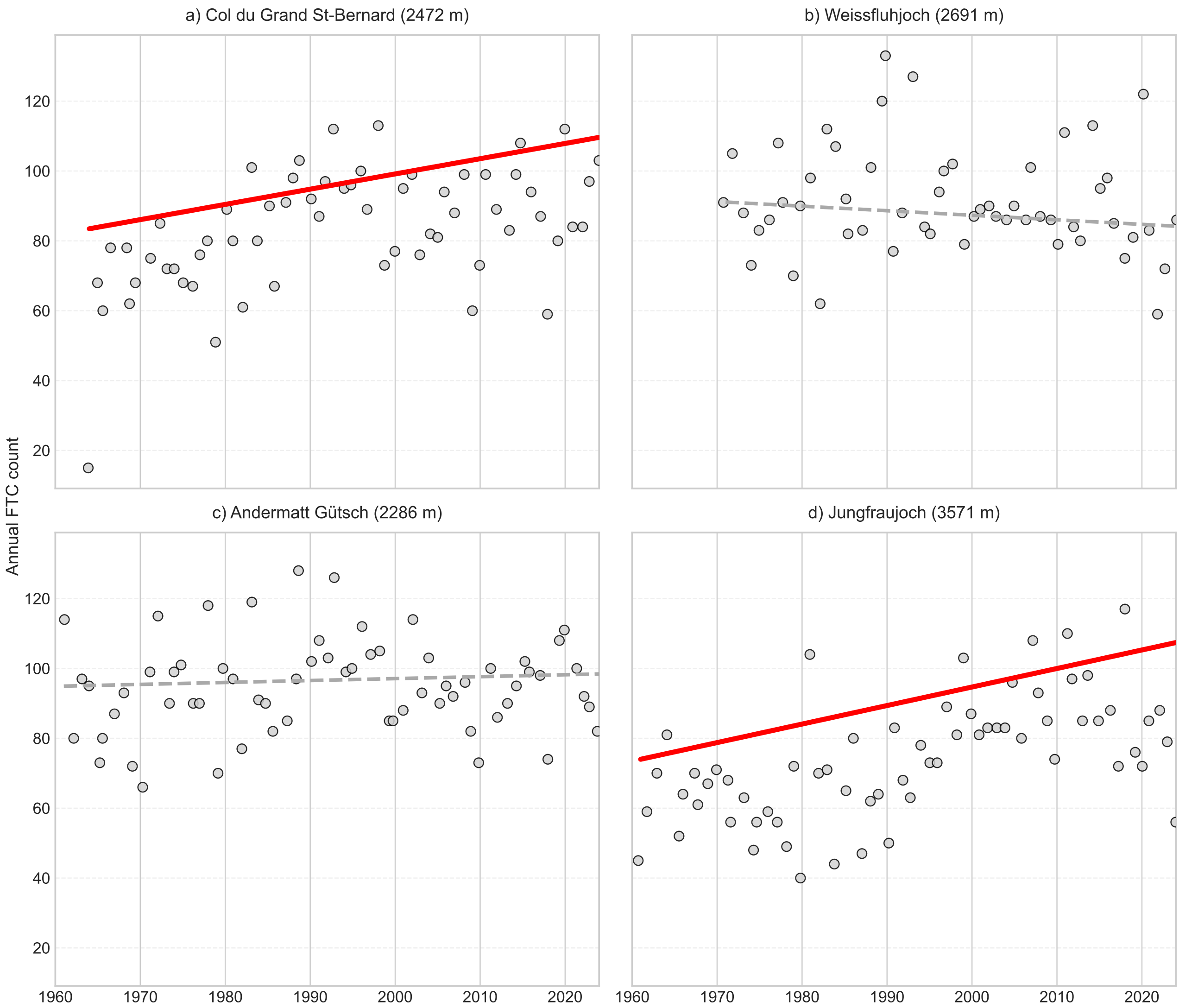

Figure 22: Annual freeze-thaw-cycle (FTC) counts at the four high elevation weather stations. Trend lines indicate direction of change: solid = statistically significant ($p<0.05$), dashed = not significant.

all statistically significant, except at Andermatt Gütsch. This contrast likely reflects elevation-dependent warming: at lower sites, rising winter temperatures more frequently cross 0 °C from below, generating additional FTCs, while Jungfraujoch winter temperatures remain predominantly sub-zero.
In spring (MAM), all stations record increasing FTC counts, most pronounced and statistically significant at Col du Grand St-Bernard (+0.17 d/yr) and Jungfraujoch (+0.14 d/yr). Notably, Jungfraujoch records substantially fewer spring FTC days (7-15 per season) than the lower stations (30-40 days).
In summer (JJA), the three lower stations show statistically significant decreasing FTC counts, dropping from 10-20 days in the 1960s to <10 days today, whereas Jungfraujoch exhibits a marked increase from ∼40 to nearly 60 FTC days per summer. This reversal likely reflects warming pushing lower-elevation summer temperatures more consistently above 0 °C (reducing FTCs), while at high elevations like Jungfraujoch, the same warming creates more days that

oscillate around 0 °C, increasing FTC frequency.
In summary, Jungfraujoch shows increasing FTCs in all seasons except winter, while the three lower stations exhibit decreasing summer FTCs, slight winter/spring increases, and stable autumn counts. At high elevation (Jungfraujoch), most FTC occur in summer and autumn, while winter and autumn show low FTC counts. At the lower stations most FTC occur in spring and autumn, while in winter and summer the count is lower.
Implications for rock slope stability: The opposite evolution of summer FTCs at high versus lower elevations is particularly relevant. Increased summer FTCs at extreme altitudes may enhance frost weathering, crack propagation, and ice segregation in cold rockwalls, while reduced FTCs at lower elevations may shift dominant processes toward purely thermal or hydrological drivers. The heterogeneous spatial patterns, increasing FTCs at the highest station but divergent trends at lower elevations, underscore that freeze-thaw cycling responds complexly to warming and that its influence on slope stability will vary with elevation and local climatic setting.
Overall, the FTC trends can be summarized for the Jungfraujoch as distinctly increasing in all seasons, except winter, and for the other three stations it can be summarized as decreasing in

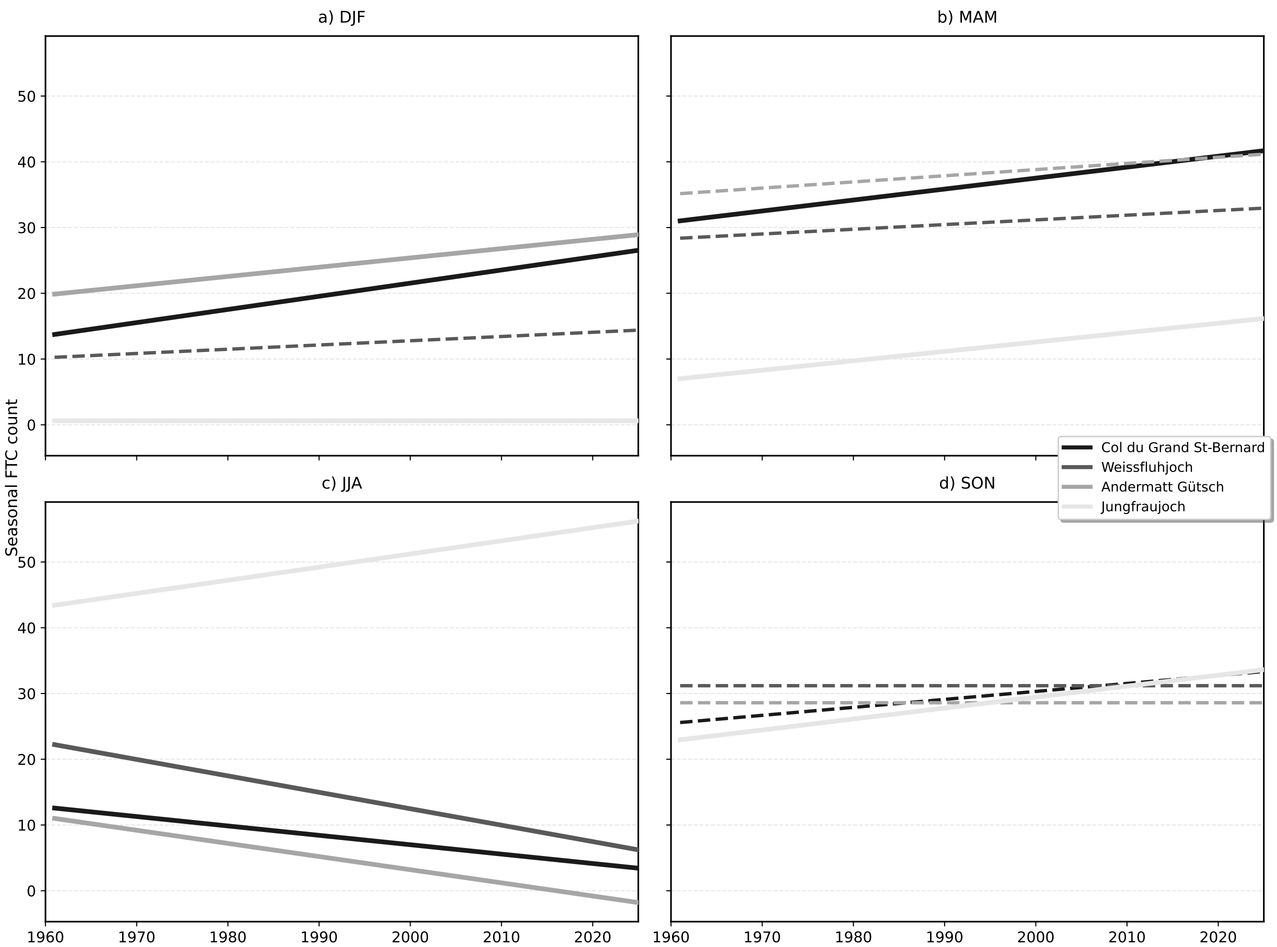

Figure 23: Seasonal freeze-thaw-cycle (FTC) trends across the four high elevation weather stations. Trend lines show direction of change for each station: solid = statistically significant ($p<0.05$), dashed = not significant.

summer and slightly increasing in winter and spring, while staying constant in autumn. However, these results have to be taken with caution, as overall the three lower station show different magnitudes of these trends, leading only to a significant increase at the Col du Grand St-Bernard.

FTC occurrence preceding individual failures was examined for events after 1960, due to limited maximum/minimum temperature data availability (N=51-54).

The temporal distribution of FTC percentiles (Figure 24) shows relatively similar distributions across time windows. Failure with FTC counts above the 95th percentile slightly decrease with increasing window length, from ∼19% (10/52 events) at 7 days to ∼17% (9/54) at 30 days and ∼15% (8/54) at 90 days. Furthermore, extremes appear to increase over time, with the proportion of 95th percentile events roughly doubling post-2000 from around 10% to almost 20% across all windows. However, due to the limited number of events, especially before 1980, this trend is likely not statistically significant. For the 1-day window, no percentiles were calculated, but ∼43% (22/51 events) of failures experienced a freeze-thaw cycle on the day immediately preceding failure. This notably high rate suggests that very short-term FTCs may contribute to final destabilization, as it substantially exceeds climatological expectations of around 25% at these elevations.

When examining the relationship by volumetric class, the two smaller classes show consistently low extreme proportions of around 10% across all windows, whereas the largest volume class (>1000k m^3) reaches 30% extremes (4/13 events). While this pattern is striking and could be consistent with large failures requiring both long-term preconditioning through structural weakening and a final FTC trigger to mobilize the full failure volume, the small sample size for this class (N=13) prevents drawing firm conclusions about FTC as a control on failure volume.

The seasonal distribution of FTC extremes (Figure 25) reveals clear differences between seasons despite the small number of events per season (N<20). In winter, extremes are rarest with only one failure recording FTC extremes, and many winter failures show zero FTC days in the 30 days preceding the failure, consistent with the predominantly sub-zero conditions documented at high-elevation stations. Autumn exhibits the highest proportions of short-window extremes (∼28% for 7-day, ∼22% for 30-day windows), but zero extremes in the 90-day window. Spring shows consistently high extreme proportions across all time windows (25-30%). Summer displays the most variable pattern (∼15% for 7-day, ∼8% for 30-day, ∼31% for 90-day windows). However, all these seasonal rates must be interpreted cautiously given the small sample sizes per season.

The FTC percentile distribution by elevation band (Figure 26) shows extremes across all elevation bands except above 4000 m, where the single failure experienced zero FTC days across all windows, consistent with continuously sub-zero conditions at extreme altitude. The 2500-3000 m band exhibits the strongest 7-day signal, with the highest median percentile (∼0.9) and the largest proportion of extremes (∼26%), coinciding with the lower permafrost boundary where thermal cycling should be most pronounced. For 30-day and 90-day windows, the distributions stabilize across elevation bands, with the 2500-3000 m median dropping to ∼0.6 while maintaining a similar proportion of extremes. This pattern suggests that while short-term FTC extremes are concentrated near the permafrost limit, the longer-window signal is more evenly distributed across the permafrost affected range.

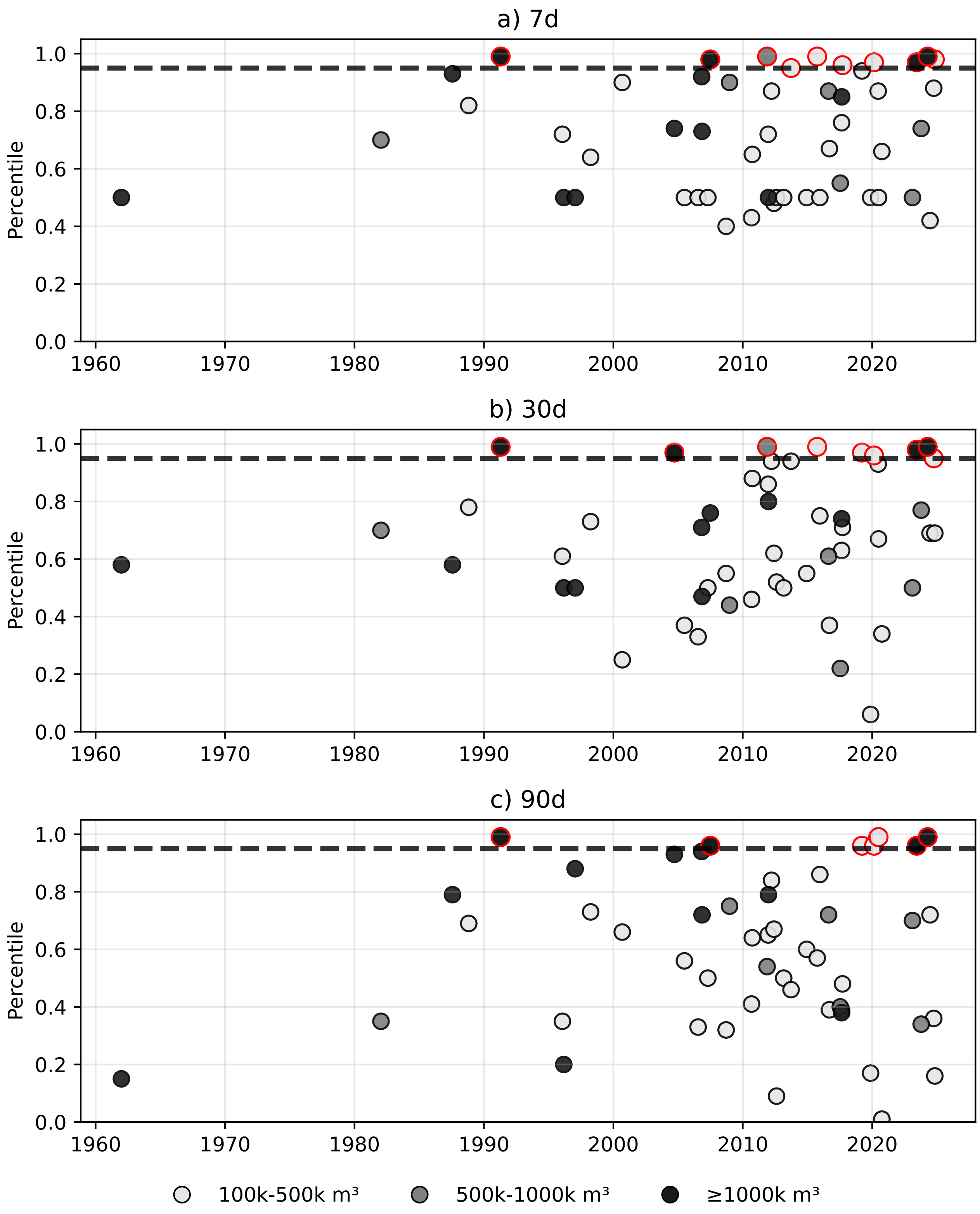

Figure 24: Temporal distribution of FTC percentiles preceding rock slope failures (7d, 30d, 90d windows). Dashed lines denote threshold (p<0.05) and events exceeding it are highlighted in red.

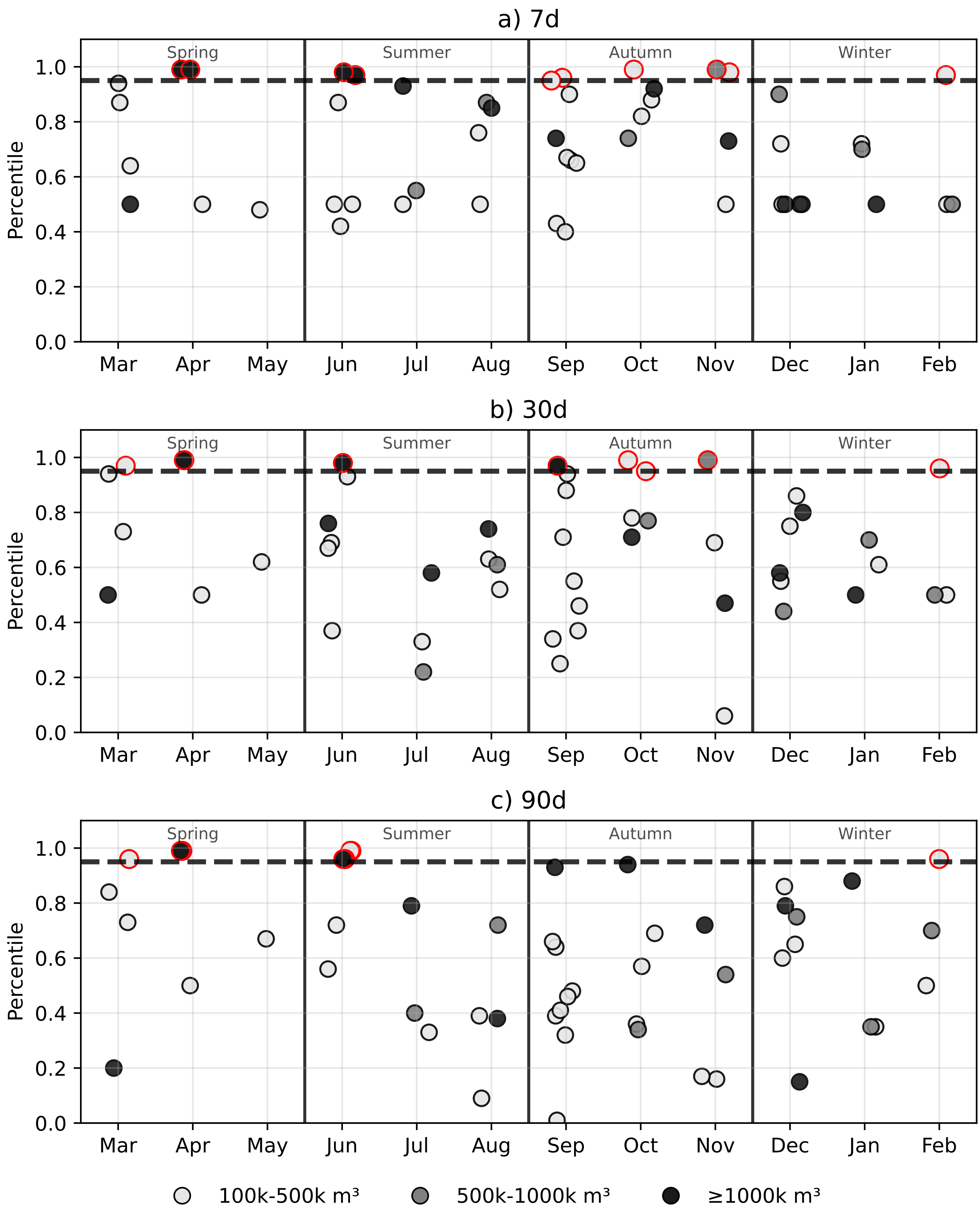

Figure 25: Seasonal distribution of FTC percentiles preceding rock slope failures (7d, 30d, 90d windows). Dashed lines denote threshold ($p<0.05$) and events exceeding it are highlighted in red.

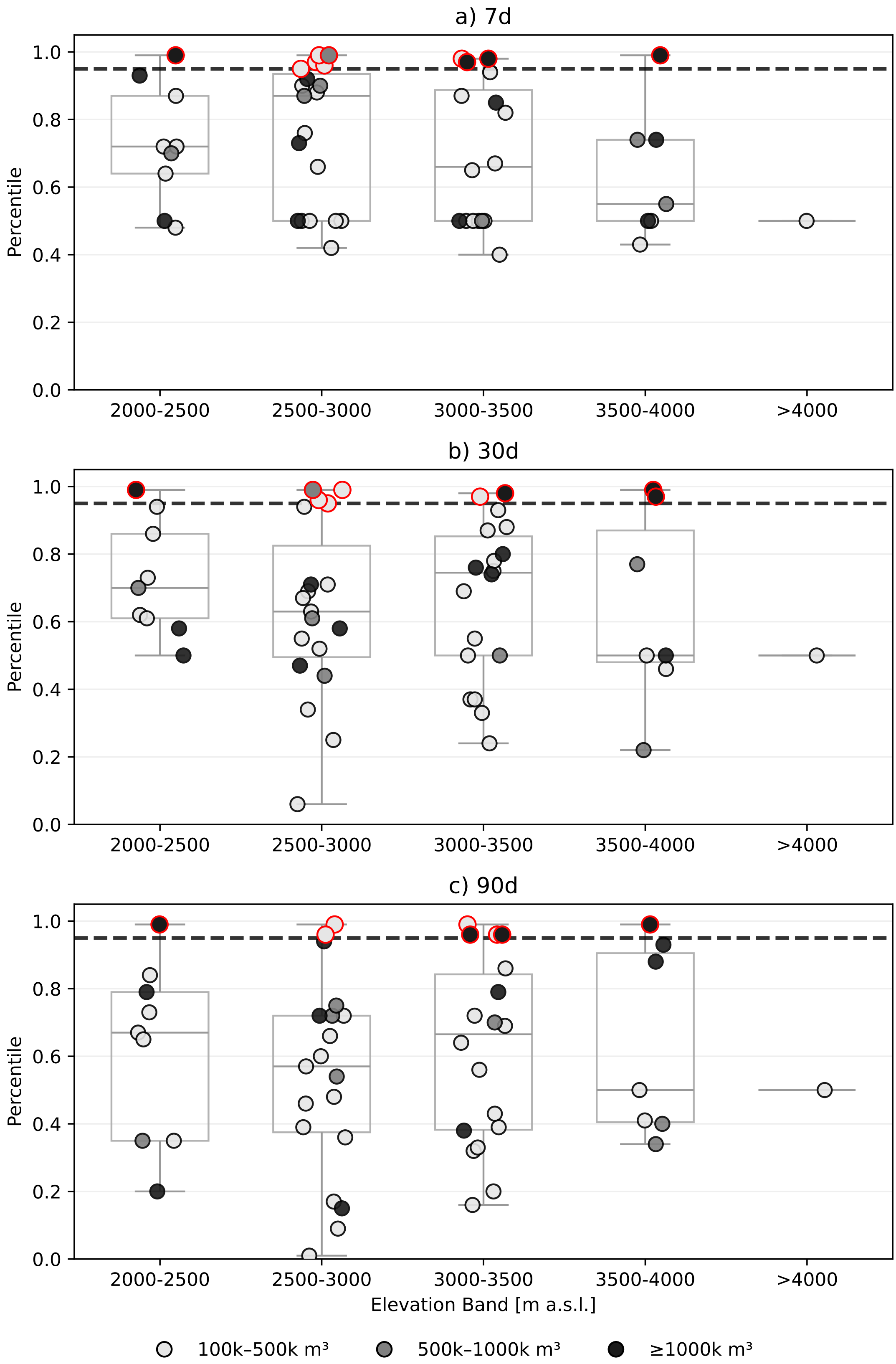

Figure 26: FTC percentile distribution preceding rock slope failures (7d, 30d, 90d windows) across different elevation bands. Dashed lines denote threshold ($p<0.05$) and events exceeding it are highlighted in red.

Overall, FTC extremes preceding failures show only a slight rise above climatological expectations (15-19% vs <10% expected), with suggestive patterns of post-2000 increase, spring/autumn short-window peaks, concentration near the permafrost boundary, and possible association with largest-volume failures. The 43% 1-day FTC rate provides the strongest evidence that short-term thermal cycling contributes to final destabilization. However, all these patterns are subject to substantial uncertainty due to the limited sample size (N=51-54) and small numbers per category. These results position FTCs as one modulator among several controlling factors rather than a primary driver of rock slope failure timing in this dataset.

4.6.3 Precipitation

Precipitation is a known trigger for many types of rock slope failures. Analysis of antecedent precipitation preceding documented rock slope failures reveals only a weak signal of extreme precipitation events. Across all time windows, consistently around 5% of failures (ranging from 1 to 5 events depending on the window length), experienced precipitation totals at or above the 95th percentile relative to the overall climatological baseline. Furthermore, only four failures (<4%) experienced an extraordinary number of days with heavy rainfall across all time scales. The temporal distribution of precipitation extremes (Figure 27) shows that no extreme precipitation events were recorded prior to 1980. Most of the few extreme events that were identified occurred after 2010. The proportion of failures experiencing precipitation extremes remains below 5% for all time windows before 2000, increasing modestly to up to 10% after 2000. However, given the very low number of extreme events identified, it is not possible to draw statistically robust conclusions about this temporal pattern.
When examining the relationship between precipitation extremes and failure volume, distinct patterns emerge across different time windows. For the shortest time windows (1-day and 7-day), precipitation extremes are limited exclusively to failures of the lowest volumetric class. Specifically, 1 out of 18 events (∼6%) of small-volume failures experienced extreme precipitation in the 1-day window preceding failure, while this proportion rises to 4 out of 33 events (∼12%) for the 7-day window. In contrast, for the longer time windows of 30 days and 90 days, precipitation extremes affect both small and large volume failures. Among the largest volume class (>1000k m^3), approximately 12% of events (2 out of 16 failures) experienced precipitation extremes in these longer windows. While this pattern is consistent with physical expectations where small-volume rock slope failures can be directly triggered by short, intense precipitation events through rapid pore pressure generation, while larger failures require sustained periods of elevated precipitation to saturate extensive fracture networks, the small number of events prevents drawing firm conclusions.
The seasonal distribution of precipitation extremes (Figure 28) shows only minor variation between seasons. In spring, summer, and autumn, between 1 and 2 failures experienced precipitation extremes across all time windows longer than 1 day. No precipitation extremes were recorded preceding any winter failures across all examined time windows. This complete absence of precipitation extremes before winter failures suggests that precipitation does not play a significant role in cold-season rock slope failures. Possibly because winter precipitation is predominantly snow rather than rain. Snow accumulation may instead influence slope stability through melting with a temporal lag during the subsequent spring transition.
Analysis of precipitation percentiles across different elevation bands (Figure 29) reveals that precipitation extremes occurred in failures across all elevation bands. Each elevation band contains between 1 and 2 failures with extreme precipitation, though the very low number of

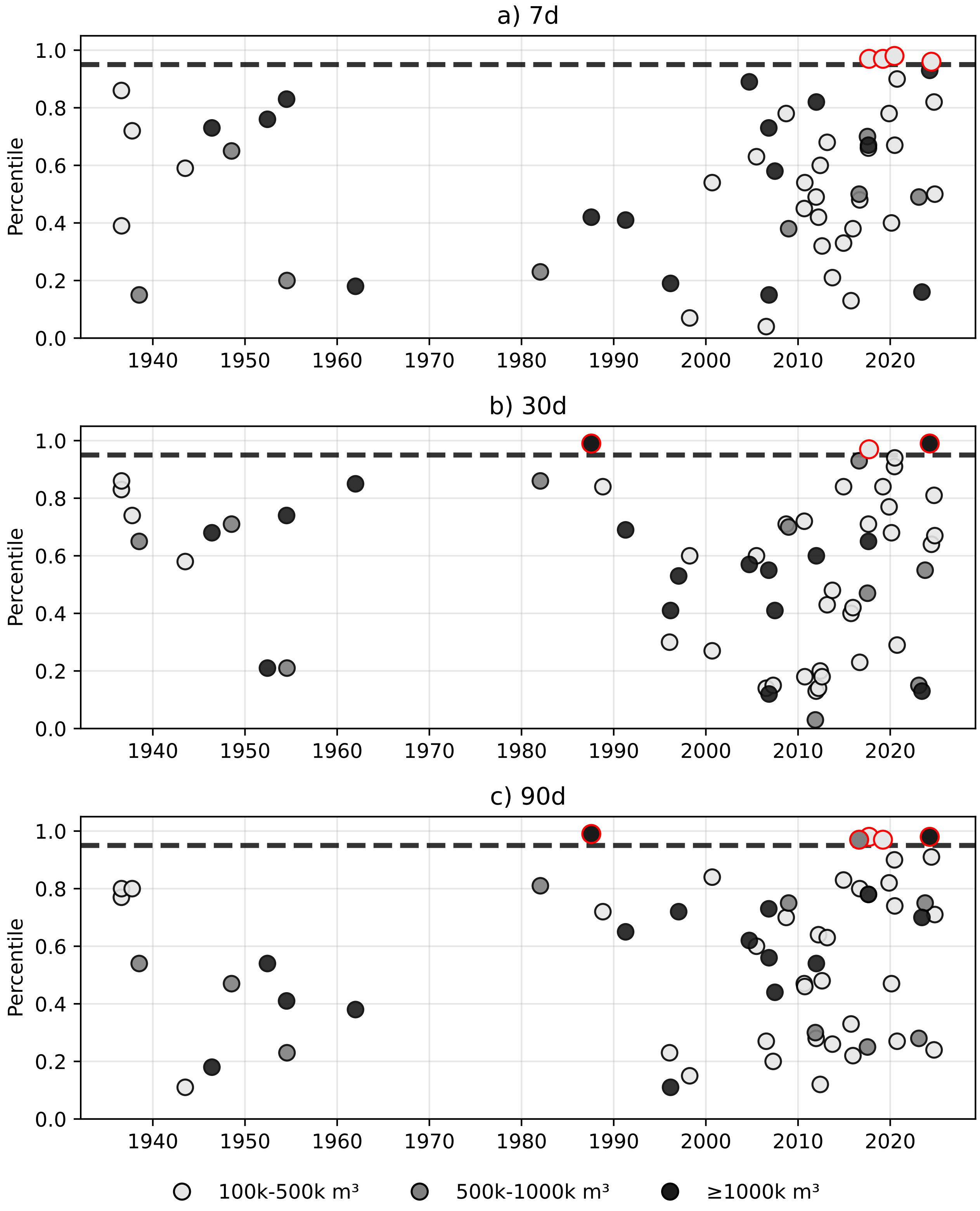

Figure 27: Temporal distribution of precipitation percentiles preceding rock slope failures (7d, 30d, 90d windows). Dashed lines denote threshold (p<0.05) and events exceeding it are highlighted in red.

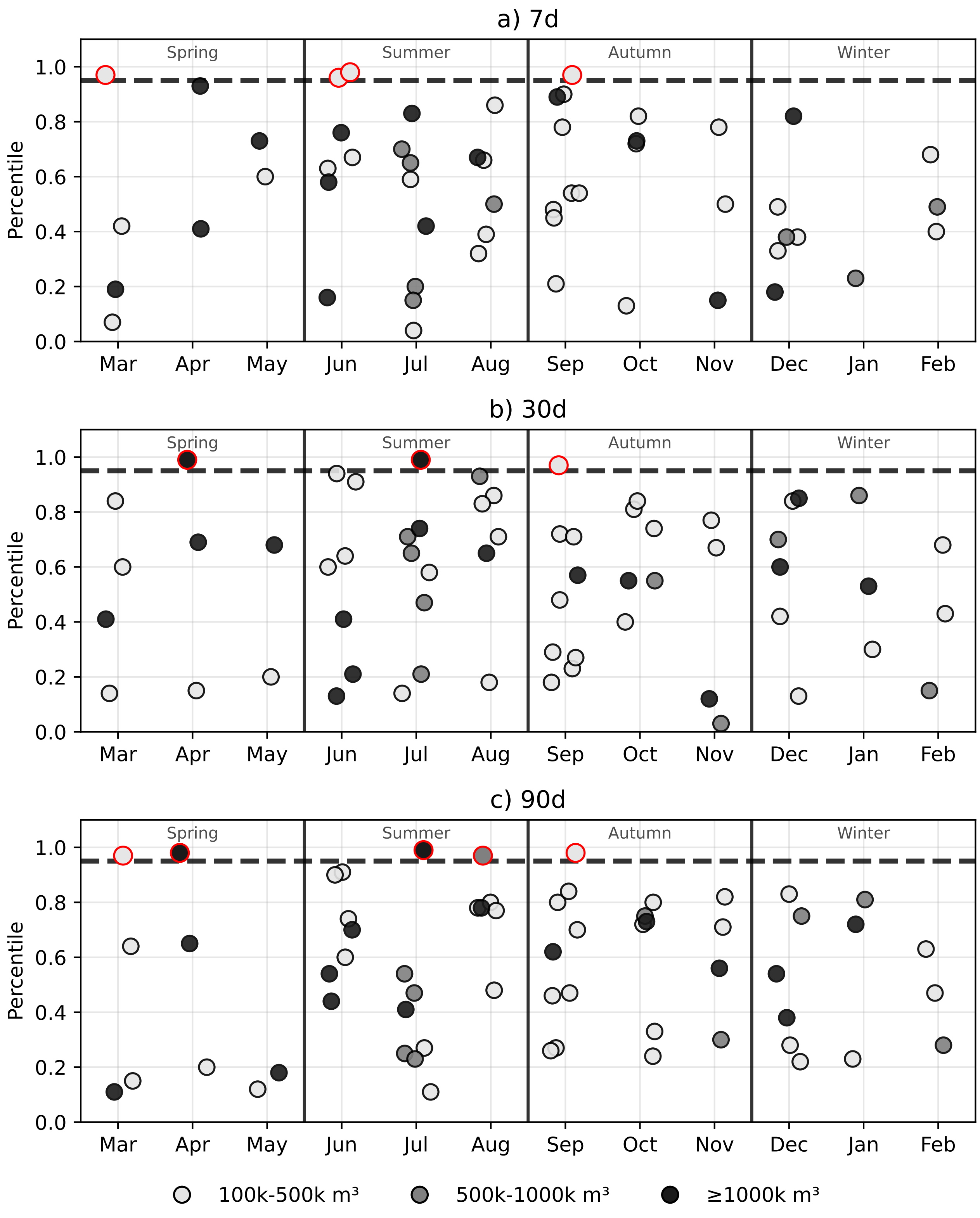

Figure 28: Seasonal distribution of precipitation percentiles preceding rock slope failures (7d, 30d, 90d windows). Dashed lines denote threshold ($p<0.05$) and events exceeding it are highlighted in red.

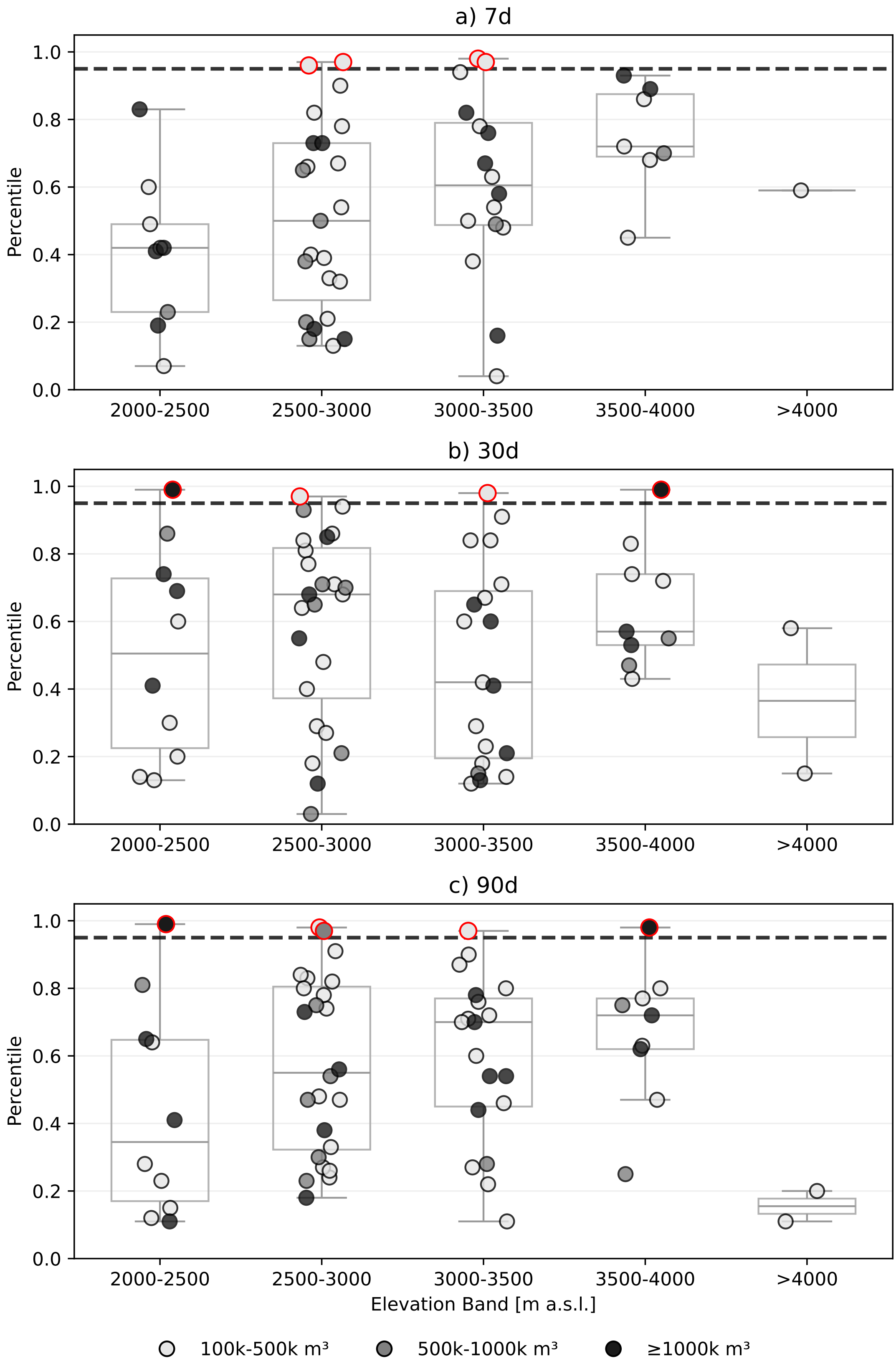

Figure 29: Precipitation percentile distribution preceding rock slope failures (7d, 30d, 90d windows) across different elevation bands. Dashed lines denote threshold ($p<0.05$) and events exceeding it are highlighted in red.

extremes per band prevents robust statistical analysis. Notably, no precipitation extremes were recorded above 4000 m, but only 2 failures occurred in this elevation range. An interesting pattern emerges in the 7-day window, where the median precipitation percentile shows a clear trend toward higher values with increasing elevation. This elevational trend becomes less pronounced in the 30-day window but reappears, albeit less strongly, in the 90-day window.
Overall, antecedent precipitation preceding rock slope failures in this dataset show only a consistently weak signal, with approximately 5% of events experiencing extreme precipitation across all metrics and time scales. This precipitation signal is substantially less prominent than the antecedent air temperature anomalies and freeze-thaw cycle patterns documented in the preceding sections. The modest indication of a post-2000 temporal increase, the concentration of short-window extremes among smaller volume failures, and the complete absence of winter precipitation extremes preceding failures all position precipitation primarily as an occasional acute trigger rather than as a dominant preconditioning or controlling factor for the large-scale instabilities examined in this study.

5 Discussion

5.1 Spatial distribution

The spatial distribution of large rock slope failures in the European Alps reveals a notable absence of activity in two main regions: the southwestern Alps and the eastern Austrian Alps. Several factors could help explain this pattern, including geomorphological, lithological, and climatic controls, as well as potential biases in data accessibility and documentation.

Topography plays an important role in determining rock slope failure potential. The southwestern Alps and eastern Austrian Alps generally exhibit lower overall elevations compared to the central Alps with large areas below 3000 m. Gentle summit plateaus and low-relief landscapes, particularly in the eastern Austrian Alps (Gradwohl et al., 2024), reduce slope height and gravitational stress, thereby lowering the potential for large slope instabilities. Nonetheless, these regions also include prominent massifs such as Barre des Écrins, Monviso, and Grossglockner. This suggests that while topographic conditions make large failures more likely in the steeper and higher-relief central Alps, similar events could still occur in the southwestern and eastern regions where sufficient slope height and relief are present.

Lithology could also influence the distribution of failures. The eastern Alps, for example, contain extensive carbonate rock domains (limestone and dolomite), especially in the northern and southern sectors (Gradwohl et al., 2024; Kellerer-Pirklbauer et al., 2022). These rocks often show pronounced karstification and efficient internal drainage, which reduce surface water pressures and pore water accumulation. As a result, slopes in these lithologies tend to be well-drained and mechanically segmented, potentially favoring smaller-scale rockfalls over large failures (Krautblatter et al., 2012). In contrast, the central Alps are largely composed of crystalline rocks, such as granites and gneisses, that may be more susceptible to deep-seated instabilities (Donnini et al., 2020). Similarly, the high proportion of carbonate rocks (∼70%) in the southwestern Alps (Kellerer-Pirklbauer et al., 2022) may explain the relative scarcity of large rock slope failures in that region. However, other studies suggest that small-volume failures are more dominant in crystalline rocks, while carbonate rocks favor larger instabilities (Abele, 1974). As literature on lithological controls is not entirely consistent, these interpretations have to be taken with caution.

Large rock slope failures in the Alps are often associated with permafrost areas and zones undergoing permafrost degradation. Given that permafrost occurs mainly at high elevations, its extent is considerably smaller in the lower-elevation eastern Alps and southwestern Alps. Consequently, these regions offer fewer environments where permafrost degradation could promote major slope failures. Furthermore, glaciation during the Last Glacial Maximum (LGM) was less extensive in these sectors, leading to lower ice thicknesses and less pronounced oversteepening, compared to the central Alps (Kellerer-Pirklbauer et al., 2022). Present-day glacier coverage confirms this tendency: only about 3.6% (∼66 km^2) of the total glaciated area in the European Alps lies within the southwestern Alps (Kellerer-Pirklbauer et al., 2022; Paul et al., 2020) and around 10.8% (∼201 km^2) in the eastern Austrian Alps (Paul et al., 2020). These geomorphic settings could lead to more stable slopes and smaller volumes of unstable rock.

The observed spatial gaps may not only result from genuine geomorphological differences but also from biases in data availability and documentation. Switzerland benefits from a centralized and well-maintained rockfall and permafrost monitoring network (PERMOS, 2025). In contrast, neighboring countries rely on decentralized or less accessible databases. For instance, the Italian Landslide Inventory (IFFI) contains over 600’000 entries but does not allow filtering by failure size, mechanism, or region (Trigila et al., 2007). Other national or regional datasets exist (Nigrelli et al., 2024; Bonometti et al., 2026) but often lack detailed data at the event scale. Similarly, the French BDMVT and C2ROP-INRAE databases contain relevant information but are either incomplete (lacking volume data) or not publicly accessible (Eckert et al., 2020). In Austria, Geosphere Austria maintains a national-scale inventory, yet data on failure size is missing, and it does not allow filtering by type (Geosphere Austria, 2025b). German datasets, such as those from the Bavarian Environment Agency (BLfU, 2025), face similar constraints. However, even well-maintained rockfall databases may not be comprehensive. An example, would be a large rock slope failure occurring at Sandgipfel in 1964, which was only very recently (after data acquisition for this inventory concluded) added to the PERMOS database, after it was rediscovered, despite records of it being in the cantonal archive (PERMOS, 2025). These inconsistencies hinder cross-border comparisons and likely contribute to apparent gaps in spatial distribution patterns and cause some events to remain undocumented in this inventory.

Finally, language barriers and the absence of a harmonized pan-Alpine inventory likely further affect data completeness. While the present inventory is likely complete for large rock slope failure (≥500'000 m^3), events with volumes closer to 100'000 m^3 could easily be underrepresented, as they are more likely to remain undetected or unreported, particularly in remote areas. Developing a unified, standardized, and publicly accessible Alpine-wide inventory could greatly improve the accuracy and comparability of future analyses, helping to distinguish between genuine spatial trends and documentation artefacts.

Overall, spatial variations in failure occurrence across the European Alps likely reflect a combination of geomorphological predisposition, lithological contrasts, and incomplete regional documentation, rather than a single dominant control.

5.2 Temporal distribution

The temporal evolution of rock slope failures suggests that long term variations in failure activity are linked to climatic phases affecting glacier extent and permafrost conditions. Periods of low activity coincide with colder phases in the twentieth century, whereas increasing failure frequency corresponds to phases of atmospheric warming and accelerated cryospheric change.

The near absence of failures during the 1960s and 1970s coincides with a period of slight atmospheric cooling in the Northern Hemisphere (Beniston, 2006). This cooling phase has been associated with glacier advances and likely with reduced degradation of near surface permafrost. Glacier advances during the 1970s and early 1980s have been documented for many smaller Alpine glaciers (Zemp et al., 2008). Cooler conditions during this period likely limited meltwater production and maintained frozen conditions in high elevation rock masses, thereby reducing progressive weakening. The temporal correspondence between this cold phase and the minimum in failure activity suggests that lower thermal forcing may have contributed to increased slope stability. A similar absence of failures during the same decades was also reported by Fischer et al. (2012), supporting the interpretation that this period reflects a regional signal rather than stochastic variability. The association between low failure activity and glacier advances is also evident for earlier periods. Glacier advances in the 1920s have been documented for smaller Alpine glaciers (Zemp et al., 2008) and coincide with a generally low number of failures in the early part of the record. In contrast, the increase in failures between the 1930s and 1950s occurs during a phase of pronounced warming in the 1940s, which has been linked to increased solar radiation (Beniston, 2006). In addition, in this phase glacier

retreat accelerated aswell (Zemp et al., 2008). This temporal correspondence further supports the interpretation that warmer conditions favor progressive slope destabilization.
The marked increase in failure frequency from the 1980s onward coincides with the transition to a phase of accelerated atmospheric warming in the Alpine region (Beniston, 2006; Auer et al., 2007; Gobiet et al., 2014; Dumont et al., 2025). Rising air temperatures during this period were accompanied by rapid glacier retreat and increasing permafrost degradation (Haeberli & Beniston, 1998; Haberkorn et al., 2021). Glacier retreat rates since 1985 have been reported to be up to seven times higher than during the period 1850 to 1973 (Paul et al., 2007). The loss of glacier ice modifies stress conditions and boundary conditions in steep headwalls, while warming permafrost leads to the degradation of ice within rock fractures and a reduction in rock mass strength (Kenner et al., 2021; Gruber & Haeberli, 2007; McColl, 2012). These processes act progressively over time and may precondition slopes for failure over decadal timescales.
The pronounced increase in failures after 2000 is consistent with a possible link between intensified warming and slope destabilization. Similar post 2000 increases have been documented in other Alpine inventories (Fischer et al., 2012), indicating that the observed trend reflects a broader regional development. The coincidence of increased failure activity with periods of enhanced warming, together with the correspondence between low activity phases and colder periods with glacier advances, suggests that long term thermal forcing plays a key role in controlling temporal variability in rock slope failures.
The seasonal distribution indicates that hydrological and thermal conditions exert an important control on failure timing, although the observed patterns differ partly from previous inventories. The concentration of events in summer and autumn suggests that increased water availability plays a central role. Snowmelt during spring and early summer and intense rainfall in late summer and autumn can enhance infiltration and temporarily raise pore water pressures, thereby reducing effective normal stress along discontinuities (Kenner et al., 2021; McColl, 2012). Cyclic pore pressure variations, with seasonal peaks during snowmelt and heavy rainfall, may trigger rock slope failures (Preisig et al., 2016). These mechanisms induce progressive damage and fatigue within the rock mass, such that failure may occur after sustained seasonal forcing rather than immediately following peak pore pressure conditions (Eberhardt et al., 2004).
The autumn peak of smaller volume failures likely reflects cumulative weakening processes during the warm season. Elevated rock temperatures and repeated thermal cycles can promote thermal cracking, ice segregation, and progressive permafrost degradation, allowing instabilities to propagate gradually before reaching critical conditions (Kenner et al., 2021; Draebing & Mayer, 2021a). In contrast, the clustering of larger failures in summer and spring suggests that short term increases in meltwater input may be particularly effective in triggering large detachments in slopes that are already critically stressed.
Comparison with previous studies highlights both similarities and differences. Paranunzio et al. (2016) reported a summer clustering of small rockfalls ($<10^4$ m^3) and a more homogeneous distribution for larger events. Fischer et al. (2012) similarly observed summer clustering for small volumes ($<10^4$ m^3) but no clear seasonal signal for larger classes. While smaller failures in the present dataset also show seasonal concentration, larger volume classes exhibit a distinct summer peak rather than a uniform distribution. Furthermore, Fischer et al. (2012) documented only one winter event, whereas a comparatively high number of winter failures is recorded here. This contrast suggests that seasonal patterns of large rock slope failures may be more variable between inventories than previously assumed, although long term preconditioning likely enables failures to occur in all seasons.

Several potential biases must also be considered when interpreting these temporal and seasonal patterns. Before 1980, documentation relied primarily on eyewitness reports, newspaper archives, and limited scientific observations. The absence of systematic remote sensing and the lower research focus on rock slope processes in high mountain environments likely resulted in incomplete records, particularly for smaller events. Although failures larger than approximately 100'000 m^3 are considered unlikely to go unnoticed (Fischer et al., 2012), the example of the Birghorn failure, which was detected through seismic monitoring (Dammeier et al., 2016), illustrates that even significant events may have remained undocumented in earlier decades when such monitoring was not available. Improved detection after 2000 is also related to digitization and expanded availability of remote sensing data, increased scientific attention to permafrost and rock slope instability, and growing human presence and infrastructure in Alpine regions. A seasonal observation bias is also possible, as mountain areas are more frequently visited during summer. While these factors likely contribute to the apparent increase in event frequency, the consistency of the temporal pattern with climatic phases and the agreement with other inventories suggest that the observed trends cannot be explained by reporting effects alone.

5.3 Topography

The topographic analysis reveals clear preferences in elevation, slope gradient and aspect. The strong concentration of detachment zones between 2600 and 3600 m appears to be a robust feature and is consistent with earlier inventories that report a clear mismatch between the elevation distribution of failures and that of the surrounding terrain (Fischer et al., 2012). The overrepresentation of failures in this band likely reflects its proximity to the lower limit of Alpine permafrost (Boeckli et al., 2012a) and its broad correspondence with the elevation range where glacier retreat and deglaciation are most pronounced (Sommer et al., 2020). Below roughly 2600 m, permafrost is much less probable and present-day glacier coverage is limited, while relief and slope steepness are generally less extreme (Boeckli et al., 2012a; Paul et al., 2020). At elevations above ~3600 m, glacier- and snow-covered terrain becomes increasingly dominant, and extensive bare rockwalls are less common, while low mean annual temperatures limit thermal cycling and hydrologically driven destabilization compared to mid-elevation bands (Paul et al., 2020; Gruber & Haeberli, 2007). This interpretation is supported by studies showing that steep slopes are proportionally more abundant at higher elevations, enhancing gravitational stress and the likelihood of failure (Fischer et al., 2012; McColl, 2012). In addition, frost cracking has been shown to be particularly effective around 3000 m and to decline at higher elevations due to limited liquid water availability (Draebing et al., 2022). Overall, elevation acts as a conditioning factor that modulates processes such as frost weathering, permafrost occurrence and glacier dynamics rather than serving as a direct mechanical driver.

Slope gradient clearly emerges as a primary topographic control. The dominance of failures on slopes between approximately 40 and 60° and the absence of events below 30° suggest a threshold around 35° for large rock slope failures in this setting. Similar threshold angles between about 35 and 45° have been reported in other Alpine inventories (Fischer et al., 2012; Noetzli et al., 2003). The scarcity of failures on slopes steeper than 60° in this dataset may partly reflect the coarseness of the 30 m terrain model, which tends to smooth extreme gradients. In addition, steep rock faces may already be strongly depleted or tend to fail through frequent, small-volume rockfalls that are not captured in this inventory (Matasci et al., 2018; Frattini et al., 2008), as seen by the higher proportion of very steep events in studies including smaller volume classes (Fischer et al., 2012). Conversely, moderately steep slopes around 30-40° may require larger failure volumes to reach instability (McColl, 2012). The apparent absence of a systematic relationship between slope gradient and failure volume in this dataset should therefore be interpreted with caution, given the small sample size and the smoothing effects of the terrain model.

Aspect effects are more subtle but nonetheless suggestive. The pronounced clustering of failures on slopes with a northerly component, and the relative scarcity of failures on south- and south-west-facing slopes, point to the importance of radiation-controlled thermal and hydrological conditions. While the 30 m model provides reliable information on general orientation (for example, north versus northeast), it is less precise for exact aspect values, and these should therefore be interpreted with caution. North-facing slopes in the Alps are generally colder, sustain permafrost over a wider elevation range and tend to retain more snow and moisture, which enhances the potential for frost cracking and ice-related weakening (Boeckli et al., 2012a; Phillips et al., 2017b). Frost cracking efficacy has been shown to be higher on cold, north-facing slopes than on warmer south-facing slopes, where temperatures more frequently exceed freezing and thus restrict frost weathering (Draebing & Krautblatter, 2019; Mayer et al., 2023; Draebing & Mayer, 2021a). In this sense, aspect does not directly control failure but modulates temperature and moisture regimes that govern permafrost occurrence, snow cover and frost weathering, which in turn influence slope stability.

These patterns must be interpreted in light of several methodological limitations. The 30 m resolution of the digital terrain model inevitably smooths the rugged morphology of steep Alpine terrain, so that narrow rockwalls, sharp breaks in slope and small detachment zones are not fully resolved. As each cell represents an average over 30 × 30 m, maximum slope angles are likely underestimated and some very steep rock faces may be mapped as moderately inclined terrain, which biases the analysis towards intermediate slope gradients. Similar uncertainties apply to elevation and aspect, particularly where detachment coordinates from the literature do not unambiguously refer to the top, middle or bottom of the source zone. These limitations do not invalidate the observed trends, but they imply that relationships between failure occurrence and topography are somewhat smoothed. Furthermore, topographic values for individual failures should be treated with caution, as they may not fully represent the exact conditions at the detachment zones.

Overall, the topographic patterns observed here are consistent with previous work and support the interpretation that steep, high-elevation slopes with a northerly component are particularly susceptible to large rock slope failures. At the same time, the use of a 30 m terrain model and uncertainties in detachment localization introduce a bias towards more moderate gradients and smoothed conditions. Topography in this dataset therefore acts primarily as a proxy for process domains shaped by cryospheric and hydrological factors, a point that is explored further in the subsequent sections on glaciers and permafrost.

5.4 Lithology

The lithological analysis reveals systematic differences in the frequency of rock slope failures among rock types. Several trends emerge that are consistent with both the geological context of the Alps and previous rock slope failure inventories. *Granit/diorit* failures are clearly overrepresented relative to their areal extent, while *limestone/dolomite* and *schist* are underrepresented. This pattern likely reflects a combination of spatial and mechanical controls. *Granit/diorit* is widespread at high elevations where steep slopes and cryospheric forcing coincide (Fischer et al., 2012), but its mechanical properties may also favor large failures. Crystalline rocks exhibit brittle fracture sets and anisotropic foliations that form persistent failure planes, enabling deep-seated slides (Crosta et al., 2013). Carbonates, by contrast, show intense karstification and blocky jointing with efficient drainage, which dissipates pore pressures and may favor smaller, frequent rockfalls over massive instabilities (Krautblatter et al., 2012; Crosta et al., 2013). In the central Alps, where most failures are documented, the proportion of crystalline rocks is highest, which may amplify this signal (Donnini et al., 2020). In the eastern and south-western Alps, the fraction of carbonate-rocks is higher, as mentioned in the section about the spatial distribution (Kellerer-Pirklbauer et al., 2022). In summary, the overrepresentation of crystalline rocks reflects both their high-elevation concentration and mechanical predisposition for large-scale instabilities, while carbonate underrepresentation aligns with drainage-limited failure potential.

Comparison with other studies reinforces these interpretations. Fischer et al. (2012) report broadly similar lithological failure distributions from their Swiss-centered inventory, though their fraction of failures in *granit/diorit* is higher than in this study. This may reflect their inclusion of smaller-volume events down to 10^4 m^3 as well as a stronger focus on central Alpine crystalline massifs. Paranunzio et al. (2016) found *limestone/dolomite* dominating the eastern Italian failures versus *gneiss* and *schist* in western sectors. This confirms that regional geological zonation strongly influences the apparent lithological preferences of failures. The lack of clear volume dependence across lithologies here, with only weak tendencies for *mafic metamorphic* and *limestone/dolomite* to host larger events, aligns with Fischer et al. (2012), who noted similar ambiguity despite including smaller volumes. Lithological analysis of extremely large rock slope failures ($>10^7$ m^3) reveals that small-volume failures are more frequent in crystalline rocks, while carbonate rocks may favor larger instabilities (Abele, 1974; Gruner, 2006). As there are only two failures in this inventory with such extreme volumes, this distinction cannot be tested. Overall, these comparisons confirm lithology influences failure frequency through regional geology and mechanical behavior rather than a universal volume control.

Fault analysis further highlights the role of structural preconditioning. Over half of documented failures coincide with mapped tectonic faults/fractures, particularly in *granit/diorit* and *limestone/dolomite*. This pattern is consistent with the role of major discontinuities, shear zones and fault-related damage belts as weak planes that can act as basal sliding surfaces and facilitate large rock slope failures (Fischer & Huggel, 2008; Stoffel et al., 2014; Stead & Wolter, 2015). Fault zones can also serve as preferential pathways for water infiltration, increasing pore pressures during periods of snowmelt or intense rainfall and thus promoting hydro-mechanical weakening (McColl, 2012). At the same time, the apparent correlation between failures and faults in certain lithologies must be interpreted cautiously. Fault mapping density and resolution are likely highest in Switzerland, where detailed geological maps exist, and lower in other regions, so faults may simply be underrepresented in some parts of the study area. Moreover, the assessment of "proximity" was qualitative, without a defined distance threshold, and each case would require detailed structural analysis to quantify the contribution of faults to failure. It is also plausible that competent rocks such as granite or limestone require prominent structural weaknesses to fail, whereas more foliated lithologies such as gneiss already contain pervasive planes of weakness and therefore show a less marked dependence on mapped faults.

These patterns must be interpreted with caution due to several methodological limitations. The underlying geological information is partially derived from maps of differing scale and quality, ranging from 1:25'000 to 1:200'000, which implies that smaller units, minor faults, and local heterogeneities are likely better captured in some parts than others. In addition, national mapping agencies may apply different lithostratigraphic schemes and grouping criteria, so lithological classes are not strictly harmonized across borders. The subsequent simplification into six broad lithological classes, following Fischer et al. (2012), facilitates comparison but inevitably masks important intra-class variability. Furthermore, the areal reference for lithology is based on the Fischer et al. (2012) study area, which does not cover the entire Alpine region considered in this work, so no consistent lithological baseline exists for the full inventory. Similar constraints apply to the analysis of tectonic faults, as no homogeneous fault map is available for the European Alps and mapping criteria likely differ between countries. Combined with the relatively small number of failures in some lithological classes, such as *conglomerate* or *schist*, these issues limit the statistical robustness and spatial representativeness of lithology-related patterns.

Overall, the results underscore the importance of lithology-structure interactions. Susceptibility rarely stems from lithology alone but arises where mechanically weak units coincide with unfavorable structural orientation (Blondeau et al., 2021; Crosta et al., 2013). Crystalline rocks with structural weaknesses appear most susceptible to large failures, while carbonates favor stability or smaller events. These patterns reinforce the central Alpine focus but are limited by mapping heterogeneity and sample size. The interaction with glacier proximity and permafrost, explored next, likely amplifies lithological predisposition under recent climate forcing (Stoffel et al., 2014).

5.5 Cryosphere

5.5.1 Glaciers

The glacier analysis reveals that a majority of documented rock slope failures are influenced by past or present glaciation, despite glaciers occupying only a small fraction of the study area. This pattern is consistent with the established role of glaciers as key preconditioning agents in alpine landscapes (Kenner et al., 2021).

Several robust trends emerge, relating to glaciation. Glaciers in the European Alps have lost more than half of their area since the LIA, with especially strong relative and absolute losses below 3000 m (Paul et al., 2020), yet the elevation distribution of failures is evenly split between slopes below and above this threshold. This indicates that glacier loss alone does not directly control the occurrence of rock slope failures. Rather, it suggests that the response of slopes to deglaciation is strongly modulated by where steep, permafrost-affected, and structurally predisposed slopes occur. At lower elevations (2000-3000 m), glacier loss has been extensive in area, but slopes are generally less steep and permafrost is less prevalent (Boeckli et al., 2012a), reducing the predisposition to large rock slope failure. At higher elevations (>3000 m), absolute glacier area loss is smaller (Paul et al., 2020), but it affects steep headwalls where high relief, persistent permafrost, and intense frost weathering coincide (Draebing et al., 2022). This is consistent with paraglacial concepts, where slope response to unloading can be delayed by decades to centuries as fractures propagate, rock bridges fail, and shear strength gradually decreases (McColl, 2012). This temporal lag implies that slopes currently adjusting to LIA-scale retreat may produce a surge in failures over coming decades as they simultaneously respond to recent glacier loss, suggesting heightened rock slope instability ahead (Kenner et al., 2021).

These patterns explain why 63% of failures are classified as glacier-influenced. This aligns with other results, e.g. Fischer et al. (2012) who found 44% of failures glacier-influenced. Glaciation class distribution further shows preconditioning mechanisms. Glaciers within slopes (19% of failures) provided thermal buffering and limited water infiltration during presence but expose bedrock to intense freeze-thaw upon retreat (Grämiger et al., 2017; Haeberli & Beniston, 1998; Kenner et al., 2021). Glaciers at the base of slopes (38% of failures) provide structural support and affect rock slope stability via stress redistribution and basal erosion during glacial cycles (Kenner et al., 2021; Grämiger et al., 2017). The small group of failures (6% of failures) classified as recently deglaciated, all belonging to the smallest volume class, may represent an early paraglacial adjustment stage in which initial response is dominated by smaller rockfalls and localized failures from thermally and mechanically shocked bedrock. Larger failures may require more time to develop, as fracture networks coalesce and rock bridges are progressively degraded (Kenner et al., 2021). Although glaciation classes are unequally represented and no baseline exists for their distribution across all steep rockwalls, each class corresponds to distinct preconditioning mechanisms.

The strong association between glacier-proximal conditions and failures in crystalline lithologies, such as *gneiss* and *granit/diorit*, is consistent with the lithological patterns discussed in section 5.4. Crystalline rocks dominate high elevation, glacier-proximal terrain (Fischer et al., 2012), and respond strongly to thermo-hydro-mechanical forcing during glacial cycles (Grämiger et al., 2017). Combining these characteristics with glacial oversteepening and permafrost degradation likely explains why glacier-adjacent failures are especially frequent in these lithologies. Fischer et al. (2012) also found a strong association between glacier-proximal conditions and failures in *gneiss* lithology. For *granit/diorit* however they found that most failures were not glacier influenced, opposing the results found here. However the high fraction of glacier-proximal area covered by *granit/diorit* lithology (38%), suggests that the results found here are more plausible, and that the differences potentially arise due to the different volumes.

The absence of a systematic relationship between failure volume and glacier influence in this dataset suggests that glaciation primarily affects the likelihood of failure occurrence rather than failure magnitude. Large failures occur in both glacier-affected and glacier-free settings, indicating that available rock mass, internal structure, and slope geometry are more important in determining volume than the simple presence or absence of ice. This is in line with findings from other inventories, which also report increased failure frequencies in glacier-influenced terrain but no clear volume control (Fischer et al., 2012).

The trends need to be interpreted with care given several methodological limitations. Glacier inventories differ in spatial resolution, temporal coverage, and data sources between countries, with Swiss and Austrian datasets generally more detailed. Consequently, glacial influence can be assessed more reliably in some regions than in others. In addition, the reconstruction of LIA glacier extent is based on historical maps, photographs, and geomorphic evidence and thus contains inherent uncertainties (Reinthaler & Paul, 2025). The four qualitative glaciation classes used here (no glaciation, glacier within the slope, glacier at the base of the slope, recently deglaciated) further introduce subjectivity, as classifications may vary depending on how strictly the classes are interpreted. Limited sample sizes in some classes, especially the recently deglaciated class, also restrict robust inference. Finally, comparing failure proportions to total areal glacier cover (11% LIA, 5% present) exaggerates the difference. A fairer baseline would be 'fraction of steep rockwalls that are glacier-adjacent'.

Overall, the results support the view that glaciers and glacier retreat act less as a single trigger and more as a set of boundary-condition shifts that accelerate damage in slopes already predisposed by their lithology, structure, and topography (McColl, 2012; Grämiger et al., 2017; Kenner et al., 2021). The higher proportion of glacier-influenced failures compared to earlier inventories, such as Fischer et al. (2012), likely reflects both differences in study area and the progressive exposure of steep crystalline rockwalls as glaciers continue to shrink. As glacier retreat proceeds and more high-elevation terrain transitions from glacial to paraglacial conditions, a further increase in rockfall and rock slope failure activity can be expected in glacier-proximal regions, even if individual failures may occur long after the ice has disappeared.

5.5.2 Permafrost

The strong overrepresentation of failures in permafrost terrain supports the interpretation that permafrost is an important conditioning factor for rock slope stability in the study area. Approximately 80% of documented failures occurred in slopes classified as permafrost affected, whereas only 37% of the total study area is modeled as permafrost. This imbalance indicates a non-random spatial association between failures and permafrost terrain. However, this pattern must be interpreted with caution because permafrost probability increases systematically with elevation and therefore covaries with other factors such as slope steepness and glacier proximity. High elevation zones are characterized by steep rockwalls and intense glacial and periglacial preconditioning, so the elevated failure density likely reflects a combination of structural, topographic and cryospheric controls rather than permafrost alone exerting a purely thermal effect.

From a process perspective, the observed clustering is consistent with the idea that warming permafrost reduces effective rock mass strength. Ice filled fractures can stabilize steep slopes under cold conditions, but warming promotes ice loss, increases hydraulic conductivity and facilitates water infiltration, thereby reducing shear resistance at rock-ice and rock-rock interfaces (Kenner et al., 2021; Gruber & Haeberli, 2007). Enhanced frost cracking intensity in permafrost rockwalls further accelerates fracture propagation and damage accumulation, particularly where water supply is sufficient (Draebing & Mayer, 2021a). In this sense, permafrost degradation likely acts as a preparatory factor that amplifies pre-existing geological weaknesses rather than acting as a sole trigger, in line with conceptual models of slope failure in high mountain environments (McColl, 2012; Kenner et al., 2021).

The clustering of failures near the lower permafrost boundary is particularly noteworthy. Transitional permafrost zones combine the presence of ground ice with frequent freeze-thaw cycles, variable pore water pressures and strong seasonal contrasts (Gruber & Haeberli, 2007). Small increases in temperature at this thermal margin can lead to thaw of ice-rich zones and rapid strength loss (Krautblatter et al., 2013). Previous studies also reported a concentration of failures close to the lower permafrost limit, especially for smaller volumes (Fischer et al., 2012). This supports the hypothesis that degrading permafrost at its lower boundary represents a zone of enhanced sensitivity. Nevertheless, the present dataset is too limited to demonstrate causality. Furthermore, the estimated lower boundary for 1850 is based solely on mean annual air temperature shifts without accounting for changes in snow cover or local microclimate.

The absence of a clear relationship between permafrost presence and failure volume suggests that permafrost primarily influences failure probability rather than magnitude. Large volumes occur both within and outside permafrost terrain. Failure size is likely more strongly controlled by structural domains, joint persistence and overall slope geometry than by thermal state alone. This partly contrasts with findings that, in their regional dataset, larger events are predominantly associated with permafrost conditions (Paranunzio et al., 2016), although other

work also shows a weaker volume dependence (Fischer et al., 2012). The discrepancy may reflect regional differences or the limited sample size.
Aspect related patterns provide additional insight. Failures without permafrost are predominantly located on east and southeast facing slopes. These aspects receive strong radiation but are not necessarily associated with long lasting permafrost (Gruber & Haeberli, 2007). In contrast, north facing slopes show clustering near the permafrost boundary. Fischer et al. (2012) found a similar pattern. An additional aspect-related effect not examined here involves cross-slope thermal and hydrological interactions. It is plausible that south facing slopes without permafrost may still influence adjacent north facing permafrost slopes by allowing enhanced warming and water infiltration into the mountain massif, thereby weakening perennially frozen detachment zones at depth (Haeberli et al., 2025). Such cross-slope thermal and hydrological interactions are not captured by surface based index models.
Several limitations constrain the interpretation. Both APIM and PERMAKART are statistical or empirical models rather than direct observations. APIM is based on mean annual air temperature, potential solar radiation and precipitation (Boeckli et al., 2012a), whereas PERMAKART relies primarily on elevation, aspect and slope (Keller, 1992). False positive and false negative classifications are therefore unavoidable. The k-means reclassification introduces an additional abstraction step, and the resulting classes do not correspond to sharp physical boundaries. Steep rockwalls, which dominate the failure dataset, are among the most constrained environments in model calibration (Boeckli et al., 2012a). Moreover, several studies demonstrate that permafrost, especially ice-rich forms, can occur well below modeled lower limits under favorable local conditions (Kenner et al., 2019; Kneisel et al., 2001). This heterogeneity is also reflected in the validation, where some low elevation failures show independent evidence of permafrost despite being classified otherwise.
Temporal aspects further complicate interpretation. Available datasets represent snapshots around 1980 and 2012, while permafrost is currently in a transient state and still adjusting to post-Little Ice Age warming. Temperature changes at depth are not resolved by surface based models, yet warm but still frozen permafrost can significantly affect stability (Noetzli & Gruber, 2009). Steep topography enhances thermal perturbation propagation, and future warming is expected to produce deep and long lasting changes in rockwall temperature fields (Haeberli & Beniston, 1998; Kenner et al., 2021). Consequently, slopes currently classified as non-permafrost may still be responding to past frozen conditions.
Overall, the results reinforce the view that permafrost degradation is a key conditioning factor for rock slope failures in high alpine terrain. At the same time, the strong covariance with elevation, relief and glacial history highlights that instability emerges from the interaction of cryospheric, structural and topographic controls. Disentangling these effects requires site specific investigations that integrate thermal monitoring, structural mapping and hydromechanical modeling beyond what regional scale index maps can provide and will be crucial for anticipating how continued permafrost warming will translate into future slope instabilities.

5.6 Climatology

5.6.1 Air temperature

The results of the air temperature analysis indicate a clear progression toward warmer conditions with increasing antecedent window length, supporting the concept of progressive thermal preconditioning. While short windows of one to seven days show largely random distributions, 30 and especially 90 day windows are distinctly shifted toward high percentiles. This pattern suggests that sustained warmth over weeks to months contributes to destabilization, consistent with the idea that temperature primarily acts as a preparatory factor (Allen & Huggel, 2013; Kenner et al., 2021). Prolonged positive anomalies can deepen the active layer, enhance permafrost degradation, accelerate glacier retreat and promote meltwater infiltration, gradually reducing rock mass strength (Kenner et al., 2021; Draebing & Mayer, 2021a). Nonetheless, short-term anomalies could still be relevant, and act as immediate triggers for failures in critically preconditioned slopes.

The weak short-term signal, however, suggests that acute heat is rarely sufficient to trigger large failures. Stronger clustering would be expected in the one and seven days windows. Instead, the data imply that single hot days or short heat pulses are generally insufficient unless slopes are already critically weakened. This interpretation aligns with observations that extreme heat can trigger collapse where long-term thermal weakening has reduced cohesion along discontinuities or for smaller failures (Allen & Huggel, 2013; Fischer et al., 2012). In this dataset, the cumulative signal over 30 to 90 days appears more relevant than isolated daily extremes, reinforcing the dual role of temperature as both long-term preconditioner and short-term modulator.

Seasonally, the high exceedance rate in spring is striking. Elevated exceedances rates in spring likely reflect the combined influence of antecedent warming, snowmelt and renewed hydrological connectivity. During this period, thawing snowpacks and ice filled fractures can generate sustained meltwater input into rockwalls, raising pore pressures and reducing effective stress (Kenner et al., 2021; Scherler et al., 2010). Spring conditions thus combine thermal weakening with enhanced water availability, amplifying destabilization potential. In contrast, winter temperatures remain largely below freezing, limiting effective thaw and meltwater production despite occasional anomalies. Summer and autumn show intermediate patterns, suggesting that while high temperatures can contribute to instability, the presence of seasonal snow and active melt processes in spring provides an additional destabilizing mechanism.

The clustering of extreme antecedent warmth in recent decades further supports a climatic interpretation. Exceedance rates increase markedly after 2000, consistent with documented acceleration of Alpine warming since the late twentieth century (Gobiet et al., 2014; Auer et al., 2007). The rise in extremely hot days across Switzerland since 1900 and particularly after 1980 provides a broader climatic backdrop (Scherrer et al., 2016), which is also apparent in the data here. Although part of the apparent increase may reflect improved event detection and reporting in recent decades, the temporal coincidence with intensifying regional warming suggests that climatic change is contributing to enhanced thermal preconditioning.

No systematic relationship between antecedent temperature anomalies and failure volume is evident. Both small and very large failures occur following warm periods, and exceedance rates do not scale consistently with magnitude. This implies that air temperature modulates overall slope readiness rather than directly controlling failure size. Failure volume is more likely governed by structural and geometric factors such as joint persistence and slope morphology, whereas temperature influences the probability that critically stressed slopes reach failure. This interpretation is compatible with inventories that report associations between warm periods and failure but do not demonstrate strong magnitude dependence (Paranunzio et al., 2016).

These findings correspond partly but not entirely to earlier studies. Allen & Huggel (2013) found that a majority of Swiss/French rockfalls were preceded by at least one very warm day in the week before failure, particularly for smaller volumes ($<10^5$ m^3). In the present

dataset, short-term exceedances are less frequent, possibly because the inventory focuses on larger events that may require longer preparatory phases. Paranunzio et al. (2016) reported that roughly half of high elevation rockfalls were linked to short-term warm anomalies, broadly comparable to the proportions observed here. However, for long-term windows (30 and 90 days) they report a much lower proportion of anomalies (∼15%). The differing spatial focus, inclusion of smaller rockfalls, and different climatological reference period could explain this difference. Their analysis also emphasized potential roles of cold anomalies and rapid cooling, which were not examined in this study. Freeze-thaw cycles and thermal contraction during abrupt cooling can generate additional mechanical stresses (Draebing et al., 2021b), suggesting that temperature variability, not only warmth, may influence stability.
Several limitations must be acknowledged. Weather stations at high elevations are rare and only those in Switzerland provide long-term continuous measurements, while for example those in Italy started continuous measurements only around 2000 (Paranunzio et al., 2015). Thus all used weather stations are located in Switzerland and therefore sometimes located kilometers from some detachment zones and often at different elevations. Although lapse rate corrections were applied, fixed literature values cannot capture potential local inversions, radiation contrasts or rockwall specific heat fluxes. Microclimatic variability near steep faces, particularly sun exposed walls, may therefore be underestimated. Maximum temperature records are not available before 1960, limiting long-term comparison. The reference period 1961 to 1990 represents a cooler baseline relative to present day conditions, meaning percentile based extremes are more frequently exceeded in recent decades. While this inflates the count of modern extremes, it simultaneously reflects the magnitude of climatic warming relative to historical norms. Finally, the modest sample size and possible temporal clustering of events reduce statistical power and limit inference.
Overall, the findings reinforce the conceptual framework that rising air temperature exerts a dual influence on alpine rock slope stability. Sustained warming over weeks to months promotes progressive thermal and hydrological weakening of cryosphere influenced slopes, while short lived extremes may provide the final perturbation, once critical thresholds are approached. As projections indicate continued increases in mean temperature and more frequent heatwaves across the Alps (Gobiet et al., 2014), the background level of thermal preconditioning is likely to intensify. This may expand the spatial range of thermally sensitive slopes and increase the probability that extreme warm periods coincide with critically weakened rock masses, thereby elevating future hazard potential.

5.6.2 Freeze-thaw cycles

The long-term evolution of freeze-thaw cycles (FTCs) reveals an elevation-dependent response to recent warming in the European Alps. At the highest site, Jungfraujoch (3571 m), annual FTC counts increase markedly, driven primarily by strong summer gains. This pattern is consistent with the conceptual understanding that warming shifts mean temperatures into the 0 °C range at formerly very cold sites, thereby creating more days that oscillate around freezing (Appenzeller et al., 2008; Migała et al., 2025). In contrast, the other three stations (2286-2691 m) show decreasing summer FTCs, reflecting temperatures that now remain more persistently above 0 °C. At the same time, slight winter and spring increases at these elevations indicate that more days cross the freezing threshold from below. Together, these findings illustrate an upward migration of the "optimal" freeze-thaw belt: altitudinal bands that were previously too cold gain FTCs, while lower belts progressively lose them. Such a redistribution aligns with projections of upward-shifting frost-cracking activity under continued warming (Appenzeller et al., 2008; Migała et al., 2025).

Seasonally, the implications for rock slope stability are nuanced. Spring emerges as a particularly relevant period, as increasing FTC counts coincide with snowmelt and high water availability. Theoretical considerations suggest that frost cracking is most efficient where temperatures oscillate around 0 °C and liquid water is present (McColl, 2012; Draebing & Mayer, 2021a). Thus, enhanced spring FTCs may disproportionately promote fracture propagation and progressive rock mass weakening. In summer, the divergence between elevations is striking: increasing FTCs at very high altitudes imply intensified frost weathering in cold permafrost walls, whereas decreasing FTCs at lower elevations suggest a relative shift toward other drivers such as thermal expansion or rainfall-related pore-pressure changes. Autumn stability in FTC counts likely indicates comparatively limited change in preparatory frost weathering, while slight winter increases at lower elevations indicate marginally elevated frost weathering. Overall, the seasonal redistribution of FTCs reinforces the interpretation of freeze-thaw processes as preparatory mechanisms that progressively reduce stability thresholds rather than acting as isolated triggers (Kenner et al., 2021).

The event-based analysis supports this interpretation. Across 7-, 30-, and 90-day windows, only a modest proportion of failures coincide with FTC counts above the 95th percentile. This limited excess suggests that anomalously high FTC activity is not a dominant standalone trigger. Instead, FTCs appear to modulate the timing of failure within already weakened rock masses. In contrast, the high proportion of failures (43%) preceded by a freeze-thaw crossing on the immediately previous day points to a potential short-term destabilizing effect. The rate substantially exceeds climatological expectations (∼25%), indicating that immediate 0 °C crossings may increase the likelihood of failure timing on already critically stressed slopes. A temperature transition across 0 °C may induce rapid ice melt, water redistribution, or transient stress changes within fractures, thereby acting as the final perturbation on slopes that have undergone longer-term degradation (Draebing & Mayer, 2021a). This distinction between long-term preparation and short-term triggering is consistent with conceptual models of frost-related slope instability (McColl, 2012; Kenner et al., 2021).

The concentration of short-window FTC extremes around 2500-3000 m further aligns with theoretical expectations. This elevation range broadly corresponds to the lower permafrost boundary, where rock temperatures are sufficiently low to sustain freezing but sufficiently warm to allow frequent oscillations. In this transitional zone, repeated freezing and thawing may coincide with progressive permafrost warming, reducing ice-bonded cohesion while simultaneously enhancing frost cracking efficiency. Such transitional thermal regimes are considered especially conductive to frost cracking (Kellerer-Pirklbauer, 2017). The observed increase in post-2000 FTC extremes around failures mirrors the station-based trend of rising FTC counts at high elevations, suggesting that ongoing climatic warming may be enhancing the relevance of freeze-thaw processes in specific altitudinal belts. However, spatial heterogeneity between stations of similar elevation highlights the importance of local climatic and topographic controls, cautioning against overly generalized conclusions.

Volume-dependent patterns provide an additional, though tentative, insight. The largest failure class shows a comparatively high fraction of FTC extremes. While the small sample size precludes firm conclusions, this pattern is compatible with a compound-process hypothesis: large rock slope failures may require prolonged structural weakening, potentially supported by repeated freeze–thaw damage, followed by a short-term perturbation such as an FTC event to mobilize the full volume. In contrast, smaller failures may occur under a wider range of immediate triggers, making them less clearly associated with FTC anomalies. If substantiated by larger datasets, this would imply that freeze–thaw processes play a disproportionate role in preparing and releasing high-magnitude events.

To date, few regional-scale inventories have systematically evaluated freeze–thaw cycle statistics preceding large rock slope failures, limiting direct comparison of percentile-based metrics. However, multiple studies exist that highlight the potential effect of freeze-thaw cycles on large rock slope failures in general and specifically for individual events (e.g. Huggel et al., 2010; Bertle et al., 2012; Paranunzio et al., 2016; Fritzmann et al., 2017).

Several limitations must be acknowledged. FTCs were derived from daily air temperature data rather than in situ rock-surface or fracture temperatures. Rockwalls, particularly in permafrost terrain, can exhibit thermal regimes that deviate substantially from free-air conditions due to radiation, snow insulation, and internal heat transfer (Kellerer-Pirklbauer, 2017). The binary "0 °C crossing" definition cannot distinguish between brief threshold crossings and prolonged freeze-thaw phases, nor can it capture multiple sub-daily cycles. Furthermore, the limited number of high-elevation stations restricts spatial representativeness, and the relatively small number of documented failures reduces statistical power.

In summary, the results suggest that freeze-thaw cycles act primarily as progressive preparatory mechanisms whose spatial and seasonal relevance is being reshaped by climate warming. Their direct triggering role appears limited but potentially significant on very short timescales and for large, already conditioned rock masses. The upward shift and seasonal redistribution of FTC activity imply that intermediate to high-alpine belts may experience intensified frost-related weakening in coming decades, even as lower elevations transition toward alternative dominant instability processes.

5.6.3 Precipitation

In contrast to the clear temperature and freeze-thaw signals, antecedent precipitation exhibits only a weak and inconsistent association with the documented rock slope failures. Across all time windows, roughly 5% of events exceed the 95th percentile of precipitation totals or show climatologically extreme numbers of heavy-rain days. This limited signal suggests that precipitation is not a systematic controlling factor for the large-scale instabilities analysed here. Instead, the results support the conceptual view that, in high-alpine rock slopes, long-term thermal and permafrost-related degradation often dominates preconditioning, while rainfall acts as an occasional acute trigger (McColl, 2012; Allen & Huggel, 2013).

The volume-dependent patterns align with established hydromechanical concepts. Short-window extremes (1-7 days) occur exclusively in the smallest volume class, consistent with shallow or limited failures responding rapidly to intense rainfall through transient pore-pressure spikes in near-surface fractures (McColl, 2012). In contrast, longer windows (30-90 days) show precipitation extremes in both small and large failures. This pattern accords with the expectation that larger failures require sustained wet conditions to progressively saturate extensive fracture networks and generate sufficient hydrostatic pressures to reduce shear strength (Fischer et al., 2010; Kenner et al., 2021). Although the small number of extreme cases precludes firm conclusions, the differentiation between short, high-intensity rainfall and prolonged wet periods reflects physically plausible triggering pathways rather than random variability.

Seasonally, the absence of precipitation extremes preceding winter failures is notable. This finding suggests that cold-season instabilities are primarily governed by thermal and mechanical processes rather than direct rainfall input. In the Alpine context, winter precipitation falls predominantly as snow, limiting immediate infiltration into rock discontinuities (Frei & Schär, 1998). Destabilizing hydrological effects may therefore occur with a temporal lag during subsequent melt periods, when liquid water becomes available and can infiltrate thawing fracture systems. Snowmelt-driven pore-pressure increases have been associated with rock slope failures in other studies (Huggel et al., 2012; Kenner et al., 2021), implying that the current daily rainfall-based approach may underestimate indirect winter contributions.

Elevationally, precipitation extremes occur across nearly all bands, indicating that rainfall-triggered failures are not confined to a narrow altitude range. The tendency toward higher median 7-day percentiles at higher elevations may point to an increased relevance of short-term wet periods in steep, glaciated, or permafrost-influenced terrain. In such settings, thawing ice layers and evolving fracture permeability can enhance hydrological connectivity, making slopes more responsive to rainfall inputs (Phillips et al., 2016; Kenner et al., 2021). However, given the very low number of extreme cases per elevation band, this pattern must be interpreted cautiously and may partly reflect stochastic variability.

Temporally, the absence of precipitation extremes before 1980 and the slight post-2000 increase in extreme antecedent conditions are suggestive but not statistically robust. An increase in heavy precipitation intensity has been documented in parts of the Alps, particularly in summer and autumn (Scherrer et al., 2016; Schmidli & Frei, 2005), and projections indicate further intensification of extreme events, especially at high elevations (Gobiet et al., 2014; Estermann et al., 2025). The modest post-2000 signal could therefore reflect emerging hydro-meteorological changes. At the same time, improved detection and documentation of rock slope failures in recent decades likely contribute to this pattern, complicating attribution. As with temperature-related trends, the precipitation signal is indicative rather than conclusive.

Comparison with previous studies underscores both consistencies and methodological differences. Paranunzio et al. (2016) identified precipitation anomalies in approximately 15% of analysed rockfalls, often in combination with temperature anomalies, and only rarely as a sole driver. This mixed forcing pattern aligns with the present results, where precipitation extremes are infrequent and rarely act in isolation. Allen & Huggel (2013) similarly noted elevated rainfall in the week preceding a minority of events without identifying precipitation as a dominant regional control. Differences in time periods, station networks, and anomaly definition likely explain discrepancies in the absolute percentages, highlighting the sensitivity of precipitation-failure relationships to methodological choices.

Several limitations constrain the interpretation. Daily totals may obscure short-duration convective peaks, which are projected to become more intense even if less frequent in summer (Estermann et al., 2025). A highly localized thunderstorm could generate critical pore-pressure responses without exceeding a 25 mm daily threshold. Furthermore, the analysis does not distinguish between rain and snow; solid precipitation is treated equivalently to liquid input, despite fundamentally different hydrological impacts. The fixed heavy-precipitation threshold and percentile approach are generic and may not reflect slope-specific triggering thresholds, which depends on lithology, fracture geometry, and antecedent moisture conditions (McColl, 2012). The binomial null model further assumes independent daily probabilities, an assumption that may be violated during clustered storm sequences. Finally, station precipitation may not accurately represent conditions at high-elevation detachment zones due to strong orographic gradients and the localized nature of convective storms (Frei & Schär, 1998).

Overall, the results position precipitation primarily as an episodic trigger rather than a dominant preparatory driver for the large rock slope failures examined here. While intense or prolonged wet periods can locally reduce stability through pore-pressure increases and hydrostatic loading, their statistical signal is substantially weaker than that of thermal anomalies and freeze–thaw dynamics. Under projected climate change, intensifying precipitation extremes may locally increase the likelihood of rainfall-triggered failures, particularly where slopes are already thermally degraded. However, in the present dataset, hydrological forcing appears secondary to long-term temperature-driven weakening processes in shaping large-scale alpine rock slope instability.

6 Conclusion

This thesis investigated the spatial and temporal patterns of large rock slope failures in the European Alps and examined the relative importance of topographic, geological, cryospheric, and climatic controls on their occurrence. By developing an expanded Alps-wide inventory of large rock slope failures (>10^5 m^3) spanning the period from 1925 to the present, this study aimed to improve the empirical basis for understanding these events in the context of ongoing environmental change. The results contribute to closing an important gap in Alpine hazard research, where previous inventories were limited in spatial extent, time coverage, or event size threshold.

The first research question addressed how the frequency and spatial distribution of large rock slope failures have evolved over the past century. The compiled inventory demonstrates that these events are widely distributed across the Alpine arc but show clustering in specific high-relief regions characterized by steep topography and active cryospheric processes. The temporal distribution suggests that large rock slope failures have occurred throughout the entire study period, but the increased documentation of events in recent decades likely reflects both improved observation and a possible influence of accelerating environmental change. While the available data do not allow an unequivocal attribution of increasing event frequency to climate change alone, the results are consistent with observations that destabilization processes in high alpine terrain may be intensifying as glaciers retreat and permafrost warms.

The second research question examined the role of topographic and geological controls. The analysis confirms that these static factors remain the primary determinants of large rock slope failure susceptibility. Elevation, slope angle, and aspect exert strong controls on the spatial distribution of detachment zones. Most failures occur on steep slopes exceeding roughly 30–35°, where gravitational stresses are high and structural discontinuities can facilitate planar or wedge failures. Elevation also plays a key role, with a concentration of events occurring in the high alpine zone where steep relief coincides with permafrost occurrence and glacier coverage. Lithology and structural features further influence failure likelihood by determining rock mass strength and the orientation of potential failure planes. These findings reinforce the interpretation that geological and geomorphological conditions establish the baseline susceptibility of slopes to failure.

The third research question explored whether signatures of climate-driven processes can be identified in the environmental context and timing of failures. The results provide multiple lines of evidence suggesting that cryospheric change acts as an important conditioning factor. Many failures occur in recently deglaciated terrain, highlighting the role of glacial debuttressing in reducing lateral support for steep rockwalls. In addition, the clustering of events near the lower boundary of permafrost suggests that warming and degradation of frozen ground may weaken rock masses and promote instability. Freeze–thaw cycles, temperature extremes, and precipitation events may further contribute as short-term triggers, although the statistical relationships remain complex. Overall, the findings support the growing body of evidence that climate-related processes interact with pre-existing geological and topographic controls to influence slope stability in the Alps.

Beyond addressing these research questions, an important outcome of this thesis is the development of an updated and expanded inventory of large rock slope failures. By integrating recent events and previously undocumented cases, the dataset improves the spatial and temporal coverage available for Alpine-wide analysis. This expanded dataset enhances statistical robustness and provides a stronger empirical foundation for identifying large-scale patterns and trends. As such, it represents a valuable contribution for future research on slope stability, cryospheric change, and natural hazard assessment in mountain environments.

The research process itself involved several methodological challenges and limitations that should be acknowledged. Constructing a consistent inventory across the entire Alpine arc required integrating information from diverse sources, including scientific publications, reports, and different databases. Differences in reporting standards, data completeness, and event documentation inevitably introduce uncertainty. Additionally, the focus on large-volume failures was chosen to minimize historical reporting bias, yet even these events may remain underrepresented in earlier decades. Further limitations arise from the use of regional-scale datasets and proxy indicators, particularly for permafrost distribution and climatic variables. These datasets provide valuable insights into large-scale patterns but cannot fully capture the local conditions that ultimately control slope stability. Consequently, the results should be interpreted as identifying regional tendencies rather than deterministic relationships.

Despite these limitations, the findings highlight several important directions for future research. First, continued expansion and systematic updating of rock slope failure inventories across the Alps would further improve statistical analyses and enable more robust detection of long-term trends. Advances in remote sensing, automated landslide detection, and satellite monitoring offer promising opportunities for near-real-time event identification and inventory development. Second, improved characterization of permafrost conditions in steep rockwalls is essential for understanding the role of cryospheric change in slope destabilization. Integrating regional analyses with site-specific monitoring, such as thermal boreholes, geophysical surveys, and high-resolution temperature modeling, would help clarify the mechanisms linking permafrost warming to rock slope failures. Third, future studies should explore coupled hydro-mechanical and thermal processes in greater detail, particularly the interactions between water infiltration, freeze–thaw cycles, and structural rock properties. Finally, interdisciplinary approaches that integrate geomorphology, climate science, and hazard modeling will be critical for translating scientific understanding into practical risk management strategies.

In summary, this thesis demonstrates that large rock slope failures in the European Alps are controlled by a complex interplay of static geological factors and dynamic environmental processes. Topography, lithology, and structural features establish the fundamental susceptibility of slopes, while cryospheric and climatic changes increasingly influence their stability. The expanded Alps-wide inventory presented here provides new empirical evidence for these interactions and contributes to a more comprehensive understanding of slope processes in a rapidly changing mountain environment. As climate warming continues to reshape the Alpine cryosphere, improving our understanding of these processes will remain essential for anticipating future hazards and supporting sustainable development in high mountain regions.

7 References

Abele, G. (1974). Bergstürze in den Alpen; ihre Verbreitung, Morphologie und Folgeerscheinungen. Wissenschaftliche Alpenvereinshefte, 25.

Alean, J. (1984). Ice avalanches and a landslide on Grosser Aletschgletscher. Zeitschrift für Gletscherkunde und Glazialgeologie, 20, 9-25.

Allen, S. and Huggel, C. (2013). Extremely warm temperatures as a potential cause of recent high mountain rockfall. Global and Planetary Change, 107, 59-69.

Appenzeller, C., Begert, M., Zenklusen, E., Scherrer, S.C. (2008). Monitoring climate at Jungfraujoch in the high Swiss Alpine region. Science of the Total Environment, 391, 262-268.

Auer, I., Böhm, R., Jurkovic, A., Lipa, W., Orlik, A., Potzmann, R., Schöner, W., Ungersböck, M., Matulla, C., Briffa, K., Jones, P., Efthymiadis, D., Brunetti, M., Nanni, T., Maugeri, M., Mercalli, L., Mestre, O., Moisselin, J.-M., Begert, M., Müller-Westermeier, G., et al. (2007). HISTALP - historical instrumental climatological surface time series of the Greater Alpine Region. International Journal of Climatology, 27, 17-46.

Autonome Provinz Bozen - Südtirol (2025). Tageswerte Niederschlag und Temperatur. Agentur für Bevölkerungsschutz: Amt für Meteorologie und Lawinenwarnung. Accessed November 2025.

Bayerisches Landesamt für Umwelt (2025). Georisiken in Bayern - WMS. Accessed February 2026.

Begert, M., Schlegel, T., Kirchhofer, W. (2005). Homogeneous temperature and precipitation series of Switzerland from 1864 to 2000. International Journal of Climatology, 25, 65-80.

Beniston, M. (2006). Mountain weather and climate: A general overview and a focus on climatic change in the Alps. Hydrobiologia, 562, 3-16.

Beniston, M., Farinotti, D., Stoffel, M., Andreassen, L.M., Coppola, E., Eckert, N., Fantini, A., Giacona, F., Hauck, C., Huss, M., Huwald, H., Lehning, M., López-Moreno, J.-I., Magnusson, J., Marty, C., Morán-Tejéda, E., Morin, S., Naaim, M., Provenzale, A., Rabatel, A., et al. (2018). The European mountain cryosphere: a review of its current state, trends, and future challenges. The Cryosphere, 12, 759-794.

Bertle, H., Heißel, G., Nittel, P. (2012). Felssturz Alpl. 13. Geoforum Umhausen Tirol.

Blondeau, S., Gunnell, Y., Jarman, D. (2021). Rock slope failure in the Western Alps: A first comprehensive inventory and spatial analysis. Geomorphology, 380, 107622.

Boeckli, L., Brenning, A., Gruber, S., Noetzli, J. (2012a). Permafrost distribution in the European Alps: calculation and evaluation of an index map and summary statistics. The Cryosphere, 6, 807-820.

Boeckli, L., Brenning, A., Gruber, A., Noetzli, J. (2012b). Alpine permafrost index map [dataset]. PANGAEA.

Bonanomi, Y. (2012). Frana Cengalo: Kurzbericht und Zwischenauswertung nach dem

Heliflug vom 04.01.2012. Bonanomi AG.

Bonometti, F.N., Dattola, G., Frattini, P., Crosta, G.B. (2026). Rockfall triggering and meteorological variables in the Dolomites (Italian Eastern Alps). Natural Hazards and Earth System Sciences, 26, 187-213.

Bosellini, A., Castellarin, A., Dal Piaz, G.V., Nardin, M. (1999). Carta Litologica e dei lineamenti strutturali 1:200'000. Servizio Geologico della Provinicia Autonoma di Trento.

Bottino, G., Chiarle, M., Joly, A., Mortara, G. (2002). Modelling Rock Avalanches and Their Relation to Permafrost Degradation in Glacial Environments. Permafrost and Periglacial Processes, 13, 283-288.

Brönnimann, S., Rajczak, J., Fischer, E.M., Raible, C.C., Rohrer, M., Schär, C. (2018). Changing seasonality of moderate and extreme precipitation events in the Alps. Natural Hazards and Earth System Sciences, 18, 2047-2056.

Buckel, J., Otto, J. C., Prasicek, G., Keuschnig, M. (2018a). Glacial lakes in Austria - Distribution and formation since the Little Ice Age. Global and Planetary Change, 164, 39-51.

Buckel, J. and Otto, J. C. (2018b). The Austrian Glacier Inventory GI 4, 2015. PANGAEA.

Cathala, M., Bock, J., Magnin, F., Ravanel, L., Ben Asher, M., Astrade, L., Bodin, X., Chambon, G., Deline, P., Faug, T., Genuite, K., Jaillet, S., Josnin, J.-Y., Revil, A., Richard, J. (2024). Predisposing, triggering and runout processes at a permafrost-affected rock avalanche site in the French Alps (Étache, June 2020). Earth Surface Processes and Landforms, 49, 3221-3247.

Centro Funzionale Regione Autonoma Valle D'Aosta, CFVDA (2025). Dati stazioni meteo. Regione Autonoma Valle d'Aosta. Accessed November 2025.

Chiarle, M., Mortara, G., Tamburini, A., Martelli, D., Sergio, L., Cat Berro, D. (2016). Il crollo del 16-17 dicembre 2025 alla Punta Tre Amici (Macugnaga, Monte Rosa). Available at: https://www.nimbus.it/ghiacciai/2016/160119˙CrolloTreAmici.htm. Accessed December 2025.

Chiarle, M., Morino, C., Mortara, G., Alberto, W., Ravello, M., Franchino, A., Orombelli, G., Giardino, M., Perotti, L., Nigrelli, G. (2023). Christmas Mass Movements in the Italian Alps. Journal of Alpine research, 111(2).

Chicco, J.M., Frasca, M., Mandrone, G., Vacha, D., Kurilla L.J. (2021). Global Warming as a Predisposing Factor for Landslides in Glacial and Periglacial Areas: An Example from Western Alps (Aosta Valley, Italy). In: Vilímek, V., et al.: Understanding and Reducing Landslide Disaster Risk. WLF 2020. ICL Contribution to Landslide Disaster Risk Reduction, Springer, Cham.

Cicoira, A., Blatny, L., Li, X., Trottet, B., Gaume, J. (2022). Towards a predictive multi-phase model for alpine mass movements and process cascades. Engineering Geology, 310, 106866.

Crosta, G.B., Chen, H., Lee, C.F. (2004). Replay of the 1987 Val Pola Landslide, Italian Alps. Geomorphology, 60, 127-146.

Crosta, G.B., Frattini, P., Agliardi, F. (2013). Deep seated gravitational slope deformations in the European Alps. Tectonophysics, 605, 13-33.

Dammeier F., Moore, J.R., Hammer, C., Haslinger F., Loew, S. (2016). Automatic detection of alpine rockslides in continuous seismic data using hidden Markov models. Journal of Geophysical Research: Earth Surface, 121, 351-371.

De Giusti, F., Dal Piaz, G.V, Schiavo, A., Massironi, M. (2004). Carta geotettonica della Valle D'Aosta. Memorie di scienze geologiche, 55, 129-149.

Deline, P. (2009). Interactions between rock avalanches and glaciers in the Mont Blanc massif during the late Holocene. Quaternary Science Reviews, 28, 1070-1083.

Deline P., Chiarle, M., Curtaz, M., Kellerer-Pirklbauer, A., Lieb, G.K., Mayr, V., Mortara, G., Ravanel, L. (2011a). Chapter 3: Rockfalls. In: Schoeneich, P., et al.: Hazards related to permafrost and to permafrost degradation. PermaNET project, state-of-the-art report 6.2.

Deline, P., Alberto, W., Broccolato, M., Hungr, O., Noetzli, J., Ravanel, L., Tamburini, A. (2011b). The December 2008 Crammont rock avalanche, Mont Blanc massif area, Italy. Natural Hazards and Earth System Sciences, 11, 3307-3318.

Donnini, M., Marchesini, I., Zucchini, A. (2020). Geo-LiM: a new geo-lithological map for Central Europe (Germany, France, Switzerland, Austria, Slovenia, and Northern Italy) as a tool for the estimation of atmospheric CO_2 consumption. Journal of Maps, 16(2), 43-55.

Draebing, D. and Krautblatter, M. (2019). The Efficacy of Frost Weathering Processes in Alpine Rockwalls. Geophysical Research Letters, 46(12), 6516-6524.

Draebing, D. and Mayer, T. (2021a). Topographic and Geologic Controls on Frost Cracking in Alpine Rockwalls. Journal of Geophysical Research: Earth Surface, 126(6).

Draebing, D. (2021b). Identification of rock and fracture kinematics in high alpine rockwalls under the influence of elevation. Earth Surface Dynamics, 9, 977-994.

Draebing, D., Mayer, T., Jacobs, B., McColl, S.T. (2022). Alpine rockwall erosion patterns follow elevation-dependent climate trajectories. Communications Earth & Environment, 3, 21.

Dramis, F., Govi, M., Guglielmin, M., Mortara, G. (1995). Mountain Permafrost and Slope Instability in the Italian Alps: the Val Pola Landslide. Permafrost and Periglacial Processes, 6, 73-82.

Dumont, M., Monteiro, D., Filhol, S., Gascoin, S., Marty, C., Hagenmuller, P., Morin, S., Choler, P., Thuiller, W. (2025). The European Alps in a changing climate: physical trends and impacts. Comptes Rendus: Géoscience, 357, 25-42.

Durand, Y., Giraud, G., Laternser, M., Etchevers, P., Mérindol, L., Lesaffre, B. (2009). Reanalysis of 47 Years of Climate in the French Alps (1958-2005): Climatology and Trends for Snow Cover. Journal of Applied Meteorology and Climatology, 48(12), 2487-2512.

Dutto, F. and Mortara, G. (1991). Grandi frane storiche con percorso su ghiacciaio in Valle d'Aosta. Revue Valdôtaine d'Histoire Naturelle, 45, 21-35.

Eberhardt, E., Stead, D., Coggan, J.S. (2004). Numerical analysis of initiation and progressive failure in natural rock slopes - the 1991 Randa rockslide. International Journal of Rock Mechanics & Mining Sciences, 41, 69-87.

Eckert, N., Mainieri, R., Bourrier, F., Giacona, F., Corona, C., Bidan, V., Lescurier, A. (2020). Une base de données événementielle du risque rocheux dans les Alpes Françaises. Revue Française de Géotechnique, 3.

Elkadi, J., Lehmann, B., King, G.E., Steinemann, O., Ivy-Ochs, S., Christl, M., Herman, F. (2022). Quantification of post-glacier bedrock surface erosion in the European Alps using ^{10}Be and optically stimulated luminescence exposure dating. Earth Surface Dynamics, 10, 909-928.

Estermann, R., Rajczak, J., Velasquez, P., Lorenz, R., Schär, C. (2025). Projections of Heavy Precipitation Characteristics Over the Greater Alpine Region Using a Kilometer-Scale Climate Model Ensemble. Journal of Geophysical Research: Atmospheres, 130(2).

Fey, C., Wichmann, V., Zangerl, C. (2025). Influence of permafrost degradation and glacier retreat on recent high mountain rockfall distribution in the eastern European Alps. Earth Surface Processes and Landform, 50(5), e70063.

Fischer, L. and Huggel C. (2008). Methodical Design for Stability Assessments of Permafrost-Affected High-Mountain Rock Walls. In: 9th International Conference on Permafrost, Fairbanks, Alaska, 29 June 2008 - 3 July 2008, 439-444.

Fischer, L., Amann, F., Moore, J.R., Huggel, C. (2010). Assessment of periglacial slope stability for the 1988 Tschierva rock avalanche (Piz Morteratsch, Switzerland). Engineering Geology, 116, 32-43.

Fischer, L., Purves, R.S., Huggel, C., Noetzli, J., Haeberli, W. (2012). On the influence of topographic, geological and cryospheric factors on rock avalanches and rockfalls in high-mountain areas. Natural Hazards and Earth System Sciences, 12, 241-254.

Fischer, L., Huggel, C., Kääb, A., Haeberli, W. (2013). Slope failures and erosion rates on a glacierized high-mountain face under climatic changes. Earth Surface Processes and Landforms, 38, 836-846.

Fischer, M., Huss, M., Barboux, C., Hoelzle, M. (2014). The new Swiss Glacier Inventory SGI2010: relevance of using high-resolution source data in areas dominated by very small glaciers. Arctic, Antarctic, and Alpine Research, 46, 933-945.

Fischer, A., Seiser, B., Stocker-Waldhuber, M., Mitterer, C, Abermann, J. (2015a). Tracing glacier changes in Austria from the Little Ice Age to the present using a lidar-based high-resolution glacier inventory in Austria. The Cryosphere, 9(2), 753-766.

Fischer, A., Seiser, B., Stocker-Waldhuber, M., Mitter, C., Abermann, J. (2015b). The Austrian Glacier Inventories, GI 1 (1969), GI 2 (1998), GI 3 (2006), and GI LIA in ArcGIS format. PANGAEA.

Frasca, M., Vacha, D., Chicco, J., Troilo, F., Bertolo, D. (2020). Landslide on glaciers: an example from Western Alps (Cogne - Italy). Journal of Mountain Science, 17(5), 1161-1171.

Frattini, P., Crosta, G., Carrara, A., Agliardi, F. (2008). Assessment of rockfall susceptibility by integrating statistical and physically-based approaches. Geomorphology, 94, 419-437.

Frattini, P., Riva, F., Crosta, G.B., Scotti, R., Greggio, L., Brardinoni, F., Fusi, N. (2016). Rock-avalanche geomorphological and hydrological impact on an alpine watershed. Geomorphology, 262, 47-60.

Frei, C., and Schär, C. (1998). A precipitation climatology of the Alps from high-resolution rain-gauge observations. International Journal of Climatology, 18(8), 873-900.

Frei, C. and Schär, C. (2001). Detection Probability of Trends in Rare Events: Theory and Application to Heavy Precipitation in the Alpine Region. Journal of Climate, 15, 1568-1584.

Fritsche, S. and Fäh, D. (2009). The 1946 magnitude 6.1 earthquake in the Valais: site-effects as contributor to the damage. Swiss Journal of Geosciences, 102, 423-439.

Fritzmann, P., Nittel-Gärtner, P., Anegg, J. (2017). TLS-basiertes Geomonitoring am Schartlaskogel (Ötztal). 19. Geoforum Umhausen Tirol.

Fuchs, F., Lenhardt, W., Bokelmann, G. (2018). Seismic detection of rockslides at regional scale: examples from the Eastern Alps and feasibility of kurtosis-based event location. Earth Surface Dynamics, 6, 955-970.

Gardent, M., Rabatel, A., Dedieu, J. P., Deline, P. (2014). Multitemporal glacier inventory of the French Alps from the late 1960s to the late 2000s. Global and Planetary Change, 120, 24-37.

Geofast (2024). Zusammenstellung ausgewählter geologischer Archivunterlagen der Geologischen Bundesanstalt 1:50'000.

GeoSphere Austria (2025a). Messstationen Tagesdaten v2. GeoSphere Austria. Accessed November 2025.

GeoSphere Austria (2025b). Gravitative Massenbewegungen. GeoSphere Austria. Accessed January 2026.

Giani, G.P., Silvano, S., Zanon, G. (2001). Avalanche of 18 January 1997 on Brenva glacier, Mont Blanc Group, Western Italian Alps: an unusual process of formation. Annals of Glaciology, 32, 333-338.

Gobiet, A., Kotlarski, S., Beniston, M., Heinrich, G., Rajczak, J., Stoffel, M. (2014). 21st century climate change in the European Alps - A review. Science of the Total Environment, 493, 1138-1151.

Gradwohl, G., Stüwe, K., Liebl, M., Robl, J., Plan, L., Rummler, L. (2024). The elevated low-relief landscapes of the Eastern Alps. Geomorphology, 458, 109264.

Grämiger, L.M., Moore, J.R., Gischig, V.S., Ivy-Ochs, S., Loew, S. (2017). Beyond debuttressing: Mechanics of paraglacial rock slope damage during repeat glacial cycles. Journal of Geophysical Research: Earth Surface, 122(4), 1004-1036.

Gruber, S., Hoelzle, M., Haeberli, W. (2004a). Rock-wall Temperatures in the Alps: Modelling their Topographic Distribution and Regional Differences. Permafrost and Periglacial Processes, 15, 299-307.

Gruber, S., Hoelzle, M., Haeberli, W. (2004b). Permafrost thaw and destabilization of Alpine rock walls in the hot summer of 2003. Geophysical Research Letters, 31.

Gruber, S. and Haeberli, W. (2007). Permafrost in steep bedrock slopes and its temperature-related destabilization following climate change. Journal of Geophysical Research, 112, F02S18.

Gruner, U. (2006). Bergstürze und Klima in den Alpen - gibt es Zusammenhänge? Swiss Bulletin für angewandte Geologie, 11(2), 25-34.

Gruner, U., Louis, K., McArdell, B. (2018). Bergstürze - Begriff, Ursachen und Einflussfaktoren, Prozessauslösung, Häufigkeit, Prozesskette und Umgang mit Bergsturzproblematik (Beitrag AGN). Swiss Bulletin für angewandte Geologie, 23(1), 7-18.

Guerin, A., Ravanel, L., Matasci, B., Jaboyedoff, M., Deline, P. (2020). The three-stage rock failure dynamics of the Drus (Mont Blanc massif, France) since the June 2005 large event. Scientific Reports, 10, 17330.

Haberkorn, A., Kenner, R., Noetzli, J., Phillips, M. (2021). Changes in Ground Temperature and Dynamics in Mountain Permafrost in the Swiss Alps. Frontiers in Earth Science, 9, 626686.

Haeberli, W., Wegmann, M., Vonder Mühll, D. (1997). Slope stability problems related to glacier shrinkage and permafrost degradation in the Alps. Eclogae Geologicae Helvetiae, 90, 407-414.

Haeberli, W. and Beniston, M. (1998). Climate Change and Its Impacts on Glaciers and Permafrost in the Alps. Ambio, 27(4), 258-265.

Haeberli, W., Cohen, D., Arenson, L. (2025). On deep thermally induced stability changes in perennially frozen detachment zones of rock-ice avalanches: The 2025 Blatten event. Abstract, International Mountain Conference Innsbruck 2025.

Hählen, N., Keusen, H.R. (2022). Susten, Berner Oberland, Felsstürze Steigletscher 2019/2020. Bulletin für Angewandte Geologie, 26(2), 21-29.

Hartmeyer, I., Delleske, R., Keuschnig, M., Krautblatter, M., Lang, A., Schrott, L., Otto, J.-C. (2020). Current glacier recession causes significant rockfall increase: the immediate paraglacial response of deglaciating cirque walls. Earth Surface Dynamics, 8, 729-751.

Hasler, A., Gruber, S., Beutel, J. (2012). Kinematics of steep bedrock permafrost. Journal of Geophysical Research: Earth Surface, 117, F01016.

Hendrickx, H., Le Roy, G., Helmstetter, A., Pointner, E., Larose, E., Braillard, L., Nyssen, J., Delaloye, R., Frankl, A. (2022). Timing, volume and precursory indicators of rock- and cliff fall on a permafrost mountain ridge (Mattertal, Switzerland). Earth Surface Processes and Landforms, 47, 1532-1549.

Hengl, T., Leal Parente, L., Krizan, J., Bonannella, C. (2022). Continental Europe Digital Terrain Model. Distributed by OpenTopography. Accessed October 2025.

Hoelzle, M. and Haeberli, W. (1995). Simulating the effects of mean annual air-temperature changes on permafrost distribution and glacier size: an example from the Upper

Engadin, Swiss Alps. Annals of Glaciology, 21, 399-405.

Huggel, C., Salzmann, N., Caplan-Auerbach, J., Fischer, L., Haeberli, W., Larsen, C., Schneider, D., Wessels, R. (2010). Recent and future warm extreme events and high-mountain slope stability. Philos. Trans. R. Soc. A Math. Phys. Eng. Sci., 368, 2435–2459.

Huggel, C., Allen, S., Deline, P., Fischer, L., Noetzli, J., Ravanel, L. (2012). Ice thawing, mountains falling - are alpine rock slope failures increasing? Geology Today, 28(3), 82-120.

Hugonnet, R., McNabb, R., Berthier, E., Menounos, B., Nuth, C., Girod, L., Farinotti, D., Huss, M., Dussaillant, I., Brun, F., Kääb, A. (2021). Accelerated global glacier mass loss in the early twenty-first century. Nature, 592, 726-731.

Keller, F. (1992). Automated Mapping of Mountain Permafrost Using the Program PERMAKART within the Geographical Information System ARC/INFO. Permafrost and Periglacial Processes, 3, 133-138.

Kellerer-Pirklbauer, A. (2017). Potential weathering by freeze-thaw action in alpine rocks in the European Alps during a nine year monitoring period. Geomorphology, 296, 113-131.

Kellerer-Pirklbauer, A., Gärtner-Roer, I., Bodin, X., Paro, L. (2022). European Alps. In: Oliva, M., Nývlt, D., Fernández-Fernández, J.M.: Periglacial Landscapes of Europe. Springer, Cham.

Kenner, R. and Phillips, M. (2017). Fels- und Bergstürze in Permafrost Gebieten: Einflussfaktoren, Auslösemechanismen und Schlussfolgerungen für die Praxis. Schlussbericht Arge Alp Projekt: Einflussfaktoren von Permafrost auf Berg- und Felsstürze.

Kenner, R., Noetzli, J., Hoelzle, M., Raetzo, H., Phillips, M. (2019). Distinguishing ice-rich and ice-poor permafrost to map ground temperatures and ground ice occurrence in the Swiss Alps. The Cryosphere, 13, 1925-1941.

Kenner, R., Arenson, L.U., Grämiger, L. (2021). Mass Movement Processes Related to Permafrost and Glaciation. In: Schroder, J.F.: Treatise on Geomorphology, 2nd Edition, Amsterdam: Academic Press, Elsevier, 5, 283-303.

Kenner, R., Noetzli, J., Bazargan, M., Scherrer, S.C. (2024). Response of alpine ground temperatures to a rising atmospheric 0°C isotherm in the period 1955-2021. Science of the Total Environment, 924, 171446.

Keusen, H.R. (1998). Die Bergstürze auf der Sandalp 1996 - Risikobeurteilung und Gefahrenmanagement. Bulletin für angewandte Geologie, 3(1), 89-102.

Kneisel, C., Hauck, C., Vonder Mühll, D. (2001). Permafrost below the Timberline Confirmed and Characterized by Geoelectrical Resistivity Measurements, Bever Valley, Eastern Swiss Alps. Permafrost and Periglacial Processes, 11(4), 295-304.

Knoflach, B., Tussetschläger, H., Sailer, R., Meißl, G., Stötter, J. (2021). High mountain rockfall dynamics: rockfall activity and runout assessment under the aspect of a changing cryosphere. Geografiska Annaler: Series A, Physical Geography, 103, 83-102.

Krautblatter, M., Moser, M., Schrott, L., Wolf, J., Morche, D. (2012). Significance of rockfall magnitude and carbonate dissolution for rock slope erosion and geomorphic work on Alpine limestone cliffs (Reintal, German Alps). Geomorphology, 167-168, 21-34.

Krautblatter, M., Funk, D., Günzel, F.K. (2013). Why permafrost rocks become unstable: a rock-ice-mechanical model in time and space. Earth Surface Processes and Landforms, 38(8), 876-887.

Krautblatter, M., Weber, S., Dietze, M., Keuschnig, M., Stockinger, G., Brückner, L., Beutel, J., Figl, T., Trepmann, C., Hofmann, R., Rau, M., Pfluger, F., Meija, L.B., Siegert, F. (2024). The 2023 Fluchthorn massive permafrost rock slope failure analysed. EGU General Assembly 2024, Vienna, Austria, 14-19 April.

Lambiel, C., Robson, B., Magnin, F., Ravanel, L. (2025). On the contribution of permafrost and its degradation on the Blatten disaster (Swiss Alps). International Mountain Conference, Sep 2025, Innsbruck, Austria.

Lindner, F., Wassermann, J., Igel, H. (2021). Seasonal Freeze-Thaw Cycles and Permafrost Degradation on Mt. Zugspitze (German/Austrian Alps) Revealed by Single-Station Seismic Monitoring. Geophysical Research Letters, 48(18).

Linsbauer, A., Huss, M., Hodel, E., Bauder, A., Fischer, M., Weidmann, Y., Bärtschi, H., Schmassmann, E. (2021). The new Swiss Glacier Inventory SGI2016: From a topographical to a glaciological dataset. Frontiers in Earth Science, 22.

Maisch, M., Wipf, A., Denneler, B., Battaglia, J., Benz, C. (2000). Die Gletscher der Schweizer Alpen: Gletscherhochstand 1850, Aktuelle Vergletscherung, Gletscherschwund-Szenarien (Schlussbericht NFP 31). 2. Auflage. vdf Hochschulverlag an der ETH Zürich, 373 pp.

Mannerfelt, E. S., Dehecq, A., Hugonnet, R., Hodel, E., Huss, M., Bauder, A., Farinotti, D. (2022). Halving of Swiss glacier volume since 1931 observed from terrestrial image photogrammetry. The Cryosphere, 16, 3249-3268.

Mariétan, I. (1954). Phénomènes d'érosion dans le vallon de Zinal. Bulletin de la Murithienne, 71, 37-45.

Matasci, B., Stock, G.M., Jaboyedoff, M., Carrea, D., Collins, B.D., Guérin, A., Matasci, G., Ravanel, L. (2018). Assessing rockfall susceptibility in steep and overhanging slopes using three-dimensional analysis of failure mechanisms. Landslides, 15, 859-878.

Mayer, T., Eppes, M., Draebing, D. (2023). Influences Driving and Limiting the Efficacy of Ice Segregation in Alpine Rocks. Geophysical Research Letters, 50(13).

McColl, S.T. (2012). Paraglacial rock-slope stability. Geomorphology, 153-154, 1-16.

Mergili, M., Jaboyedoff, M., Pullarello, J., Pudasaini, S.P. (2020). Back calculation of the 2017 Piz Cengalo-Bondo landslide cascade with r.avaflow: what we can do and what we can learn. Natural Hazards and Earth System Sciences, 20, 505-520.

Météo-France (2025). Données climatologiques de base - quotidiennes. Météo-France. Accessed November 2025.

MeteoSwiss (2025a). Ground-based measurements and homogeneous data series from individual stations with explanatory metadata. Federal Office of Meteorology and Climatology MeteoSwiss. Accessed November 2025.

MeteoSwiss and ETH Zurich (2025b). Climate CH2025 - Scientific Report. Federal Office of Meteorology and Climatology MeteoSwiss, Zurich.

Meteotrentino (2025). Dati storici - Stazioni meteorologiche. Meteotrentino. Accessed November 2025.

Michoud, C., Derron, M.-H., Horton, P., Jaboyedoff, M., Baillifard, F.-J., Loye, A., Nicolet, P., Pedrazzini, A., Queyrel, A. (2012). Rockfall hazard and risk assessments along roads at a regional scale: example in Swiss Alps. Natural Hazards and Earth System Sciences, 12, 615-629.

Migała, K., Wieczorek, M., Kasprzak, M., Traczyk, A. (2025). Long-term trends of freeze-thaw cycles in the Northern Hemisphere. Climatic Change, 179, 7.

Moore, J.R., Gischig, V., Burjanek, J., Löw, S., Fäh, D. (2011). Site effects in unstable rock slopes: dynamic behaviour of the Randa instability (Switzerland). Bulletin of the Seismological Society of America, 101, 3110-3116.

Müller, F., Caflisch, T., Müller, G. (1976). Firn und Eis der Schweizer Alpen (Gletscherinventar). Publ. Nr. 57/57a. Geographisches Institut, ETH Zürich, 2 Vols.

Nigrelli, G., Paranunzio, R., Turconi, L., Luino, F., Mortara, G., Guerini, M., Giardino, M., Chiarle, M. (2024). First national inventory of high-elevation mass movements in the Italian Alps. Computers and Geosciences, 184, 105520.

Noetzli, J., Hoelzle, M., Haeberli, W. (2003). Mountain permafrost and recent Alpine rockfall events: a GIS-based approach to determine critical factors. Proceeding of the 8th International Conference on Permafrost, Zürich, Switzerland; 827-832.

Noetzli, J. and Gruber, S. (2009). Transient thermal effects in Alpine permafrost. The Cryosphere, 3, 85-99.

Offer, M., Weber, S., Krautblatter, M., Hartmeyer, I., Keuschnig, M. (2025). Pressurised water flow in fractured permafrost rocks revealed by borehole temperature, electrical resistivity tomography, and piezometric pressure. The Cryosphere, 19, 485-506.

Oswald, P., Strasser, M., Hammerl, C., Moernaut, J. (2021). Seismic control of large prehistoric rockslides in the Eastern Alps. Nature Communications, 12, 1059.

Paranunzio, R., Laio, F., Nigrelli, G., Chiarle, M. (2015). A method to reveal climatic variables triggering slope failures at high elevation. Natural Hazards, 76, 1039-1061.

Paranunzio, R., Laio, F., Chiarle, M., Nigrelli, G., Guzzetti, F. (2016). Climate anomalies associated with the occurrence of rockfalls at high-elevation in the Italian Alps. Natural Hazards and Earth System Sciences, 16, 2085-2106.

Paul, F. (2004). The new Swiss glacier inventory 2000 - application of remote sensing and GIS. PhD Thesis, Department of Geography, University of Zurich, Schriftenreihe Physische Geographie, 52, 210 pp.

Paul, F., Kääb, A., Haeberli, W. (2007). Recent glacier changes in the Alps observed by satellite: Consequences for future monitoring strategies. Global and Planetary Change, 56(1-2), 111-122.

Paul, F., Rastner, P., Azzoni, R.S., Diolaiuti, G., Fugazza, D., Le Bris, R., Nemec, J., Rabatel, A., Ramusovic, M., Schwaizer, G., Smiraglia, C. (2020). Glacier shrinkage in the Alps continues unabated as revealed by a new glacier inventory from Sentinel-2. Earth System Science Data, 12, 1805-1821.

Peleg, N., Koukoula, M., Rajczak, J., Kotlarski, S., Dallan, E., Marra, F. (2025). Hotter summers, heavier showers: Global warming and its impact on Swiss short-duration rainfall extremes. Weather and Climate Extremes, 50, 100829.

Pfluger, F., Weber, S., Steinhauser, J., Zangerl, C., Fey, C., Fürst, J., Krautblatter, M., (2025). Massive permafrost rock slide under a warming polythermal glacier deciphered through mechanical modeling (Bliggspitze, Austria). Earth Surface Dynamics, 13, 41-70.

Phillips, M., Haberkorn, A., Draebing, D., Krautblatter, M., Rhyner, H., Kenner, R. (2016). Seasonally intermittent water flow through deep fractures in an Alpine Rock Ridge: Gemsstock, Central Swiss Alps. Cold Regions Science and Technology, 125, 117-127.

Phillips, M., Wolter, A., Lüthi, R., Amann, F., Kenner, R., Bühler, Y. (2017a). Rock slope failure in a recently deglaciated permafrost rock wall at Piz Kesch (Eastern Swiss Alps), February 2014. Earth Surface Processes and Landforms, 42, 426-438.

Phillips, M., Haberkorn, A., Rhyner, H. (2017b). Snowpack characteristics on steep frozen rock slopes. Cold Regions Science and Technology, 141, 54-65.

Phillips, M., Kenner, R., Scandroglio, R. (2025). TASK 1.4 - Rockfall disposition. In: Bast, A., Bründl, M., Phillips, M.: WSL Berichte: Vol. 181. WSL research programme Climate Change Impacts on Alpine Mass Movements - CCAMM: project report, 33-38.

Pierhöfer, L., Bartelt, P., Bühler, Y., Hafner, E., Kenner, R., Walter, F., Phillips, M. (2024). Bergsturz vom 14. April 2024 am Piz Scerscen, Graubünden. WSL-Institut für Schnee- und Lawinenforschung SLF.

Pirulli, M. (2009). The Thurwieser rock avalanche (Italian Alps): Description and dynamic analysis. Engineering Geology, 109, 80-92.

Pollinger, R., Mair, V., Profanter, P. (2016). Report Pericoli naturali 2016 - Relazione Riassuntiva Documentazione Eventi. Autonome Provinz Bozen - Südtirol.

Preisig, G., Eberhardt, E., Smithyman, M., Preh, A., Bonzanigo, L. (2016). Hydromechanical Rock Mass Fatigue in Deep-Seated Landslides Accompanying Seasonal Variations in Pore Pressures. Rock Mechanics and Rock Engineering, 49, 2333-2351.

Rajczak, J., Pall, P., Schär, C. (2013). Projections of extreme precipitation events in regional climate simulations for Europe and the Alpine Region. Journal of Geophysical Research: Atmospheres, 118(9), 3425-3917.

Ravanel, L. and Deline, P. (2008). La face ouest des Drus (massif du Mont-Blanc): évolution de l'instabilité d'une paroi rocheuse dans la haute montagne alpine depuis la fin du petit âge glaciaire. Géomorphologie: relief, processus, environnement, 14(4), 261-272.

Ravanel, L., Allignol, F., Deline, P., Gruber, S., Ravello, M. (2010). Rock falls in the Mont Blanc Massif in 2007 and 2008. Landslides, 7, 493-501.

Reinthaler, J. and Paul, F. (2025). Reconstructed glacier area and volume changes in the European Alps since the Little Ice Age. The Cryosphere, 19, 753-767.

Rolland, C. (2003). Spatial and seasonal variations of air temperature lapse rates in Alpine regions. Journal of Climate, 16, 1032-1046.

Rottler, E., Kormann, C., Francke, T., Bronstert, A. (2018). Elevation-dependent warming in the Swiss Alps 1981-2017: Features, forcings and feedbacks. International Journal of Climatology, 39(5), 2556-2568.

Salvatore, M.C., Zanoner T., Baroni, C., Carton, A., Banchieri, F.A., Viani, C., Giardino, M., Perotti, L. (2015). The state of Italian glaciers: A snapshot of the 2006-2007 hydrological period. Geografia Fisica e Dinamica Quaternaria, 38(2), 175-198.

Sartori, M., Baillifard, F., Jaboyedoff, M., Rouiller, J.-D. (2003). Kinematics of the 1991 Randa rockslides (Valais, Switzerland). Natural Hazards and Earth System Sciences, 3, 423-433.

Scherler, M., Hauck, C., Hoelzle, M., Stähli, M., Völksch, I. (2010). Meltwater infiltration into the frozen active layer at an alpine permafrost site. Permafrost and Periglacial Processes, 21(4), 325-334.

Scherrer, S.C., Fischer, E.M., Posselt, R., Liniger, M.A., Croci-Maspoli, M., Knutti, R. (2016). Emerging trends in heavy precipitation and hot temperature extremes in Switzerland. Journal of Geophysical Research: Atmospheres, 121(6), 2626-2637.

Schindler, C., Cuénod, Y., Eisenlohr, T., Joris, C.-L. (1993). Die Ereignisse vom 18. April und 9. Mai 1991 bei Randa (VS) - ein atypischer Bergsturz in Raten. Eclogae Geologicae Helvetiae, 86(3), 643-665.

Schmidli, J. and Frei, C. (2005). Trends of heavy precipitation and wet and dry spells in Switzerland during the 20th century. International Journal of Climatology, 25(6), 753-771.

Smiraglia, C., Azzoni, R., D'Agata, C., Maragno, D., Fugazza, D., Diolaiuti, G. (2015). The New Italian Glacier Inventory: a didactic tool for a better knowledge of the natural Alpine environment. Journal of Research and Didactics in Geography, 1, 81-94.

Sommer, C., Malz, P., Seehaus, T.C., Lippl, S., Zemp, M., Braun, M.H. (2020). Rapid glacier retreat and downwasting throughout the European Alps in the early 21st century. Nature Communications, 11, 3209.

Sosio, R., Crosta, G.B., Hungr, O. (2008). Complete dynamic modeling calibration for the Thurwieser rock avalanche (Italian Central Alps). Engineering Geology, 100, 11-26.

Stead, D. and Wolter, A. (2015). A critical review of rock slope failure mechanisms: The importance of structural geology. Journal of Structural Geology, 74, 1-23.

Stoffel, M., Tiranti, D., Huggel, C. (2014). Climate change impacts on mass movements - Case studies from the European Alps. Science of the Total Environment, 493, 1255-1266.

Swiss Permafrost Monitoring Network (PERMOS) (2016). Permafrost in Switzerland 2010/2011 to 2013/2014, Glaciological Report Permafrost No. 12-15. Cryospheric Commission of the Swiss Academy of Sciences.

Swiss Permafrost Monitoring Network (PERMOS) (2025). PERMOS/SLF Rock Fall Database. Swiss Permafrost Monitoring Network, Davos and Fribourg, Switzerland.

Swisstopo (2024). Geologischer Atlas der Schweiz 1:25'000 (GA25). Bundesamt für Landestopografie.

Tamburini, A., Villa, F., Fischer, L., Hungr, O., Chiarle, M., Mortara, G. (2011). Slope instabilities in high-mountain rock walls. Recent events on the Monte Rosa east face (Macugnaga, NW Italy). Landslide Science and Practice, Springer, Berlin, 327-332.

Trigila, A., Iadanza, C., Guerrieri, L. (2007). The IFFI project (Italian landslide inventory): Methodology and results. In: Guidelines for mapping areas at risk of landslides in Europe. Joint Research Centre: Institute for Environment and Sustainability.

Unesco Sardona (2024). Felssturz beim Martinsloch am Grossen Tschingelhorn. Available at: https://unesco-sardona.ch/erlebnis/felssturz-martinsloch. Accessed December 2025.

Walter, F., Amann, F., Kos, A., Kenner, R., Phillips, M., Preux, A.D., Huss, M., Tognacca C., Clinton, J., Diehl, T., Bonanomi, Y. (2020). Direct observations of a three million cubic meter rock-slope collapse with almost immediate initiation of ensuing debris flows. Geomorphology, 351, 106933.

Weber, S., Beutel, J., Faillettaz, J., Hasler, A., Krautblatter, M., Vieli, A. (2017). Quantifying irreversible movement in steep, fractured bedrock permafrost on Matterhorn (CH). The Cryosphere, 11, 567-583.

Wegmann, M. (1998). Frostdynamik in hochalpinen Felswänden am Beispiel der Region Jungfraujoch - Aletsch. PhD thesis, ETH Zürich, Zürich.

Wilhelm, C., Feuerstein, G.C., Huwiler, A., Kühne, R. (2019). Bergsturz Cengalo und Murgänge Bondo: Erfahrungen der kantonalen Fachstelle. In: Bründl, M. & Schweizer, J.: WSL Berichte: Vol. 78. Lernen aus Extremereignissen, 53-66.

Zangerl, C., Fey, C., Prager, C. (2019). Deformation characteristics and multi-slab formation of a deep-seated rock slide in a high alpine environment (Bliggspitze, Austria). Bulletin of Engineering Geology and the Environment, 78, 6111-6130.

Zemp, M., Paul, F., Hoelzle, M., Haeberli, W. (2008). Glacier fluctuations in the European Alps, 1850-2000: an overview and spatio-temporal analysis of available data. In: Orlove, B., et al.: Darkening Peaks: Glacier retreat, Science, and Society. Berkeley, US, 152-167.

Zemp, M., Frey, H., Gärtner-Roer, I., Nussbaumer, S.U., Hoelzle, M., Paul, F., Haeberli, W., Denzinger, F., Ahlstrøm, A.P., Anderson, B., Bajracharya, S., Baroni, C., Braun, L.N., Cáceres, B.E., Casassa, G., Cobos, G., Dávila, L.R., Delgado Granados, H., Demuth, M.N., Espizua, L., et al. (2015). Historically unprecedented global glacier decline in the early 21st century. Journal of Glaciology, 61(228), 745-762.

8 Appendix

Table 3: List of documented large rock slope failures and their sources

No	Name	Source
1	Kleines Nesthorn (CH)	[PERMOS, 2025], [Lambiel et al., 2025]
2	Dent de Pro (CH)	[PERMOS, 2025]
3	Tschingelhorn (CH)	[PERMOS, 2025], [Unesco Sardona, 2024]
4	Portalet/Ravines Rousses (CH)	[PERMOS, 2025]
5	Piz Scerscen II (CH)	[PERMOS, 2025], [Pierhöfer et al., 2024]
6	Piz Scerscen I (CH)	[PERMOS, 2025], [Pierhöfer et al., 2024]
7	Fluchthorn (AT/CH)	[PERMOS, 2025], [Krautblatter et al., 2024]
8	Piz Umur (CH)	[Pierhöfer et al., 2024]
9	Ritzlihorn/Mattenlimmi (CH)	[PERMOS, 2025]
10	Grosser Graben St. Niklaus (CH)	[PERMOS, 2025], [Hendrickx et al., 2022]
11	Vallon d'Etache (FR)	[Cathala et al., 2024]
12	Steingletscher II (CH)	[PERMOS, 2025], [Hählen & Keusen, 2022]
13	Steingletscher I (CH)	[PERMOS, 2025], [Hählen & Keusen, 2022]
14	Flüela Wisshorn (CH)	[PERMOS, 2025], [Cicoira et al., 2022]
15	Cengalo VI (CH)	[PERMOS, 2025], [Wilhelm et al., 2019]
16	Cengalo V (CH)	[PERMOS, 2025], [Wilhelm et al., 2019], [Walter et al., 2020], [Mergili et al., 2020]
17	Cengalo IV (CH)	[PERMOS, 2025], [Walter et al., 2020]
18	Trajo Glacier (IT)	[Chicco et al., 2021], [Frasca et al., 2020]
19	Cengalo III (CH)	[PERMOS, 2025]
20	Picola Croda Rossa (IT)	[PERMOS, 2025], [Pollinger et al., 2016]
21	Punta Tre Amici II (IT)	[PERMOS, 2025], [Chiarle et al., 2016], [Chiarle et al., 2023]
22	Sölden/Schartlaskogel (AT)	[Fritzmann et al., 2017], [Fuchs et al., 2018]
23	Mulets de la Lia (CH)	[PERMOS, 2025]
24	Piz Kesch (CH)	[Phillips et al., 2017a], [Kenner & Phillips, 2017]
25	Cengalo II (CH)	[PERMOS, 2025]
26	Crast'Agüzza (IT)	[PERMOS, 2025]
27	Wasenhorn (CH)	[PERMOS, 2025]
28	Taschachtal (AT)	[Fuchs et al., 2018]
29	Hochwand/Alpl (AT)	[Fuchs et al., 2018], [Bertle et al., 2012]
30	Cengalo I (CH)	[PERMOS, 2025], [Wilhelm et al., 2019], [Walter et al., 2020], [Bonanomi, 2012]
31	Sass Maor (IT)	[Chiarle et al., 2023]
32	Birghorn (CH)	[PERMOS, 2025], [Dammeier et al., 2016]
33	Punta Tre Amici I (IT)	[Chiarle et al., 2023], [Fischer et al., 2013], [Paranunzio et al., 2016]
34	Punta Thurwieser II (IT)	[Frattini et al., 2016]
35	Mont Crammont (IT)	[PERMOS, 2025], [Chiarle et al., 2023], [Deline et al., 2011b], [Paranunzio et al., 2016]
36	Punta Patri Nord (IT)	[Deline et al., 2011a], [Paranunzio et al., 2016]
37	Bliggspitze (AT)	[Zangerl et al., 2019], [Pfluger et al., 2025]

No	Name	Source
38	Monte Rosa II (IT)	[PERMOS, 2025], [Fischer et al., 2013], [Paranunzio et al., 2016], [Tamburini et al., 2011], [Fischer et al., 2012]
39	Dents Blanches (CH)	[PERMOS, 2025], [Fischer et al., 2012]
40	Dent du Midi (CH)	[PERMOS, 2025], [Fischer et al., 2012]
41	Cima Dodici (IT)	[Paranunzio et al., 2016]
42	Drus (FR)	[PERMOS, 2025], [Guerin et al., 2020], [Ravanel & Deline, 2008], [Fischer et al., 2012]
43	Punta Thurwieser I (IT)	[PERMOS, 2025], [Frattini et al., 2016], [Paranunzio et al., 2016], [Pirulli, 2009], [Sosio et al., 2008], [Fischer et al., 2012]
44	Gruben (CH)	[Noetzli et al., 2003]
45	Mättenberg/Ankenbaelli (CH)	[PERMOS, 2025], [Noetzli et al., 2003], [Fischer et al., 2012]
46	Zuetribistock III (CH)	[PERMOS, 2025], [Keusen, 1998]
47	Brenva (FR)	[PERMOS, 2025], [Paranunzio et al., 2016], [Noetzli et al., 2003], [Giani et al., 2001], [Deline, 2009], [Fischer et al., 2012]
48	Zuetribistock II (CH)	[PERMOS, 2025], [Noetzli et al., 2003], [Keusen, 1998], [Fischer et al., 2012]
49	Zuetribistock I (CH)	[PERMOS, 2025], [Noetzli et al., 2003], [Keusen, 1998], [Fischer et al., 2012]
50	Miage III (IT)	[Noetzli et al., 2003], [Fischer et al., 2012]
51	Randa (CH)	[PERMOS, 2025], [Noetzli et al., 2003], [Schindler et al., 1993], [Sartori et al., 2003], [Eberhardt et al., 2004], [Fischer et al., 2012]
52	Piz Morteratsch/Tschierva (CH)	[PERMOS, 2025], [Noetzli et al., 2003], [Fischer et al., 2010], [Fischer et al., 2012]
53	Miage II (IT)	[Deline, 2009]
54	Val Pola (IT)	[PERMOS, 2025], [Noetzli et al., 2003], [Dramis et al., 1995], [Crosta et al., 2004], [Fischer et al., 2012]
55	Fiernaz (IT)	[Chiarle et al., 2023]
56	Monte Rosa I (IT)	[Fischer et al., 2012]
57	Chli Spannort (CH)	[PERMOS, 2025], [Abele, 1974]
58	Garde de Bordon II (CH)	[PERMOS, 2025], [Mariétan, 1954]
59	Feegletscher (CH)	[Fischer et al., 2012], [Abele, 1974], [Gruner et al., 2018]
60	Becca de Luseney (IT)	[PERMOS, 2025], [Noetzli et al., 2003], [Fischer et al., 2012], [Abele, 1974], [Dutto & Mortara, 1991]
61	Garde de Bordon I (CH)	[PERMOS, 2025], [Mariétan, 1954]
62	Rawilhorn (CH)	[PERMOS, 2025], [Fischer et al., 2012], [Gruner et al., 2018], [Moore et al., 2011], [Fritsche & Fäh, 2009]
63	Miage I (IT)	[Noetzli et al., 2003], [Deline, 2009], [Fischer et al., 2012]
64	Matterhorn (IT)	[PERMOS, 2025], [Noetzli et al., 2003], [Fischer et al., 2012]
65	Piz Beverin (CH)	[PERMOS, 2025]

No	Name	Source
66	Jungfrau (CH)	[PERMOS, 2025], [Noetzli et al., 2003], [Fischer et al., 2012], [Alean, 1984], [Wegmann, 1998]
67	Chli Windgällen (CH)	[PERMOS, 2025]
68	Felikhorn (IT)	[PERMOS, 2025], [Noetzli et al., 2003], [Fischer et al., 2012], [Dutto & Mortara, 1991], [Bottino et al., 2002]

Table 4: List of documented large rock slope failures and their topographic characteristics. Referenced sources are: [a] Pierhöfer et al. 2024, [b] Hendrickx et al., 2022, [c] Cathala et al., 2024, [d] Chicco et al., 2021, [e] Ravanel & Deline, 2008, [f] Noetzli et al., 2003. For variables without a source, the values were obtained from the digital elevation model.

No	Name	Mean Elevation [m]	Elevation Class [m]	Slope Gradient	Slope Class	Aspect	Aspect Class
1	Kleines Nesthorn (CH)	3260	3200-3400	40-50°	40-50°	10°	N
2	Dent de Pro (CH)	3487	3400-3600	50-60°	50-60°	343°	N
3	Tschingelhorn (CH)	2800	2800-3000	55-60°	50-60°	22°	N
4	Portalet/Ravines Rousses (CH)	2700	2600-2800	45-50°	40-50°	110°	E
5	Piz Scerscen II (CH)	3640	3600-3800	50°[a]	50-60°	285°	W
6	Piz Scerscen I (CH)	3535	3400-3600	50°[a]	50-60°	276°	W
7	Fluchthorn (AT/CH)	3396	3200-3400	45-50°	40-50°	251°	W
8	Piz Umur (CH)	3250	3200-3400	55-60°	50-60°	284°	W
9	Ritzlihorn/Mattenlimmi (CH)	2625	2600-2800	45-50°	40-50°	15°	N
10	Grosser Graben St. Niklaus (CH)	2680	2600-2800	20°[b]	20-30°	254°	W
11	Vallon d'Etache (FR)	3120	3000-3200	43°[c]	40-50°	316°	NW
12	Steingletscher II (CH)	2500	2400-2600	40-45°	40-50°	359°	N
13	Steingletscher I (CH)	2500	2400-2600	40-45°	40-50°	359°	N
14	Flüela Wisshorn (CH)	3022	3000-3200	40-45°	40-50°	302°	NW
15	Cengalo VI (CH)	2970	2800-3000	55-60°	50-60°	48°	NE
16	Cengalo V (CH)	3075	3000-3200	55-60°	50-60°	49°	NE
17	Cengalo IV (CH)	2900	2800-3000	55-60°	50-60°	35°	NE
18	Trajo Glacier (IT)	3500	3400-3600	60°[d]	60-70°	92°	E
19	Cengalo III (CH)	3020	3000-3200	55-60°	50-60°	350°	N
20	Picola Croda Rossa (IT)	2770	2600-2800	45-50°	40-50°	14°	N
21	Punta Tre Amici II (IT)	3400	3400-3600	55-60°	50-60°	76°	E
22	Sölden/Schartlaskogel (AT)	2720	2600-2800	45-50°	40-50°	6°	N
23	Mulets de la Lia (CH)	2677	2600-2800	50-55°	50-60°	1°	N
24	Piz Kesch (CH)	3107	3000-3200	45-50°	40-50°	351°	N
25	Cengalo II (CH)	2740	2600-2800	55-60°	50-60°	2°	N
26	Crast'Agüzza (IT)	3850	3800-4000	60-65°	60-70°	172°	S
27	Wasenhorn (CH)	2700	2600-2800	45-50°	40-50°	310°	NW
28	Taschachtal (AT)	2460	2400-2600	40-45°	40-50°	112°	E
29	Hochwand/Alpl (AT)	2250	2200-2400	55-60°	50-60°	191°	S
30	Cengalo I (CH)	3170	3000-3200	55-60°	50-60°	54°	NE
31	Sass Maor (IT)	2200	2200-2400	55-60°	50-60°	131°	SE
32	Birghorn (CH)	2996	2800-3000	40-45°	40-50°	322°	NW
33	Punta Tre Amici I (IT)	3200	3200-3400	45-50°	40-50°	72°	E
34	Punta Thurwieser II (IT)	3630	3600-3800	45-50°	40-50°	151°	SE
35	Mont Crammont (IT)	2600	2600-2800	45-50°	40-50°	17°	N
36	Punta Patri Nord (IT)	3330	3200-3400	55-60°	50-60°	121°	SE
37	Bliggspitze (AT)	3250	3200-3400	35-40°	30-40°	350°	N
38	Monte Rosa II (IT)	4130	4000-4200	45-50°	40-50°	44°	NE

No	Name	Mean Elevation [m]	Elevation Class [m]	Slope Gradient	Slope Class	Aspect	Aspect Class
39	Dents Blanches (CH)	2517	2400-2600	55-60°	50-60°	6°	N
40	Dent du Midi (CH)	2793	2600-2800	50-55°	50-60°	334°	NW
41	Cima Dodici (IT)	3094	3000-3200	55-60°	50-60°	259°	E
42	Drus (FR)	3410	3400-3600	75°[e]	≥70°	315°	NW
43	Punta Thurwieser I (IT)	3630	3600-3800	45-50°	40-50°	151°	SE
44	Gruben (CH)	3520	3400-3600	50°[f]	50-60°	294°	NW
45	Mättenberg/Ankenbaelli (CH)	2873	2800-3000	42°[f]	40-50°	267°	W
46	Zuetribistock III (CH)	2300	2200-2400	55-60°	50-60°	90°	E
47	Brenva (FR)	3872	3800-4000	48°[f]	40-50°	128°	SE
48	Zuetribistock II (CH)	2200	2200-2400	74°[f]	≥70°	122°	SE
49	Zuetribistock I (CH)	2300	2200-2400	64°[f]	60-70°	99°	E
50	Miage III (IT)	3000	3000-3200	53°[f]	50-60°	315°[f]	NW
51	Randa (CH)	2300	2200-2400	54°[f]	50-60°	143°	SE
52	Piz Morteratsch/Tschierva (CH)	3180	3000-3200	52°[f]	50-60°	261°	W
53	Miage II (IT)	3350	3200-3400	50-55°	50-60°	274°	W
54	Val Pola (IT)	2320	2200-2400	30°[f]	30-40°	61°	NE
55	Fiernaz (IT)	2000	2000-2400	40-45°	40-50°	138°	SE
56	Monte Rosa I (IT)	3940	3800-4000	50-55°	50-60°	67°	NE
57	Chli Spannort (CH)	2934	2800-3000	40-45°	40-50°	312°	NW
58	Garde de Bordon II (CH)	2900	2800-3000	55-60°	50-60°	86°	E
59	Feegletscher (CH)	2330	2200-2400	40-45°	40-50°	126°	SE
60	Becca de Luseney (IT)	3054	3000-3200	38°[f]	30-40°	245°	SW
61	Garde de Bordon I (CH)	2900	2800-3000	55-60°	50-60°	86°	E
62	Rawilhorn (CH)	2527	2400-2600	50-55°	50-60°	160°	S
63	Miage I (IT)	3400	3400-3600	44°[f]	40-50°	18°	N
64	Matterhorn (IT)	4150	4000-4200	75°[f]	≥70°	129°	SE
65	Piz Beverin (CH)	2797	2600-2800	50-55°	50-60°	356°	N
66	Jungfrau (CH)	3809	3800-4000	61°[f]	60-70°	107°	E
67	Chli Windgällen (CH)	2700	2600-2800	unkn.	unkn.	unkn.	SW
68	Felikhorn (IT)	3585	3400-3600	38°[f]	30-40°	273°	W

Table 5: List of documented large rock slope failures and their lithologic and geologic characteristics. Referenced sources are: [a] PERMOS, 2025, [b] Swisstopo, 2024, [c] Cathala et al., 2024, [d] De Giusti et al., 2004, [e] Chicco et al., 2021, [f] Pollinger et al., 2016, [g] Geofast, 2024, [h] Fritzmann et al., 2017, [i] Bertle et al., 2012, [j] Paranunzio et al., 2016, [k] Bosellini et al., 1999, [l] Sosio et al., 2008, [m] Deline et al., 2011b, [n] Zangerl et al., 2019, [o] Fischer et al., 2013, [p]Ravanel & Deline, 2008, [q] Keusen, 1998. Events marked with an '*' are located within the study area defined by Fischer et al., 2012.

No	Name	Lithology	Fault/ Fracture	Source
1*	Kleines Nesthorn (CH)	Gneiss	no/unknown	[a], [b]
2*	Dent de Pro (CH)	Gneiss	no/unknown	[b]
3*	Tschingelhorn (CH)	Gneiss	yes	[a], [b]
4*	Portalet/Ravines Rousses (CH)	Granit/Diorit	yes	[b]
5*	Piz Scerscen II (CH)	Granit/Diorit	yes	[a], [b]
6*	Piz Scerscen I (CH)	Granit/Diorit	yes	[a], [b]
7*	Fluchthorn (AT/CH)	Mafic Metamorphic	no/unknown	[a]
8*	Piz Umur (CH)	Granit/Diorit	no/unknown	[b]
9*	Ritzlihorn/Mattenlimmi (CH)	Gneiss	yes	[b]
10*	Grosser Graben St. Niklaus (CH)	Gneiss	yes	[a], [b]
11	Vallon d'Etache (FR)	Schist	yes	[c]

No	Name	Lithological Class	Presence of Fault/Fracture	Sources
12*	Steingletscher II (CH)	Gneiss	no/unknown	[b]
13*	Steingletscher I (CH)	Gneiss	no/unknown	[b]
14*	Flüela Wisshorn (CH)	Gneiss	yes	[a], [b]
15*	Cengalo VI (CH)	Gneiss	yes	[a], [b]
16*	Cengalo V (CH)	Gneiss	yes	[a], [b]
17*	Cengalo IV (CH)	Gneiss	yes	[a], [b]
18	Trajo Glacier (IT)	Mafic Metamorphic	yes	[d], [e]
19*	Cengalo III (CH)	Gneiss	yes	[a], [b]
20	Picola Croda Rossa (IT)	Limestone/Dolomite	yes	[f]
21*	Punta Tre Amici II (IT)	Gneiss	no/unknown	[b]
22	Sölden/Schartlaskogel (AT)	Mafic Metamorphic	no/unknown	[g], [h]
23*	Mulets de la Lia (CH)	Schist	no/unknown	[b]
24*	Piz Kesch (CH)	Gneiss	yes	[b]
25*	Cengalo II (CH)	Gneiss	yes	[b]
26*	Crast'Agüzza (IT)	Granit/Diorit	yes	[b]
27*	Wasenhorn (CH)	Gneiss	yes	[b]
28	Taschachtal (AT)	Gneiss	no/unknown	[g]
29	Hochwand/Alpl (AT)	Limestone/Dolomite	yes	[g], [i]
30*	Cengalo I (CH)	Gneiss	yes	[b]
31	Sass Maor (IT)	Limestone/Dolomite	no/unknown	[j], [k]
32*	Birghorn (CH)	Granit/Diorit	no/unknown	[b]
33*	Punta Tre Amici I (IT)	Gneiss	no/unknown	[b]
34	Punta Thurwieser II (IT)	Limestone/Dolomite	yes	[l]
35	Mont Crammont (IT)	Conglomerates	yes	[d], [m]
36	Punta Patri Nord (IT)	Gneiss	no/unknown	[d]
37	Bliggspitze (AT)	Gneiss	yes	[g], [n]
38*	Monte Rosa II (IT)	Gneiss	yes	[b], [o]
39*	Dents Blanches (CH)	Limestone/Dolomite	yes	[a], [b]
40*	Dent du Midi (CH)	Limestone/Dolomite	no/unknown	[b]
41	Cima Dodici (IT)	Limestone/Dolomite	no/unknown	[j]
42*	Drus (FR)	Granit/Diorit	yes	[p]
43	Punta Thurwieser I (IT)	Limestone/Dolomite	yes	[l]
44*	Gruben (CH)	Schist	no/unknown	[b]
45*	Mättenberg/Ankenbaelli (CH)	Granit/Diorit	no/unknown	[b]
46*	Zuetribistock III (CH)	Limestone/Dolomite	yes	[a], [q]
47*	Brenva (FR)	Granit/Diorit	no/unknown	[j]
48*	Zuetribistock II (CH)	Limestone/Dolomite	yes	[a], [q]
49*	Zuetribistock I (CH)	Limestone/Dolomite	yes	[a], [q]
50	Miage III (IT)	Gneiss	unknown	[d]
51*	Randa (CH)	Gneiss	no/unknown	[b]
52*	Piz Morteratsch/Tschierva (CH)	Granit/Diorit	yes	[a], [b]
53	Miage II (IT)	Gneiss	no/unknown	[d]
54*	Val Pola (IT)	Mafic Metamorphic	no/unknown	[a]
55*	Fiernaz (IT)	Mafic Metamorphic	no/unknown	[d]
56*	Monte Rosa I (IT)	Gneiss	yes	[b], [o]
57*	Chli Spannort (CH)	Limestone/Dolomite	no/unknown	[b]
58*	Garde de Bordon II (CH)	Mafic Metamorphic	yes	[a], [b]
59*	Feegletscher (CH)	Gneiss	no/unknown	[b]
60*	Becca de Luseney (IT)	Gneiss	no/unknown	[d]
61*	Garde de Bordon I (CH)	Mafic Metamorphic	yes	[a], [b]
62*	Rawilhorn (CH)	Limestone/Dolomite	yes	[a], [b]
63	Miage I (IT)	Gneiss	no/unknown	[d]
64*	Matterhorn (IT)	Gneiss	yes	[a], [b]
65*	Piz Beverin (CH)	Schist	yes	[a], [b]

No	Name	Lithological Class	Presence of Fault/Fracture	Sources
66*	Jungfrau (CH)	Gneiss	no/unknown	[a]
67*	Chli Windgällen (CH)	Schist	unknown	[b]
68*	Felikhorn (IT)	Gneiss	no/unknown	[d]

Table 6: List of documented large rock slope failures and their cryospheric characteristics

No	Name	Glacier	Permafrost
1	Kleines Nesthorn (CH)	base of slope	in nearly all conditions
2	Dent de Pro (CH)	base of slope	in nearly all conditions
3	Tschingelhorn (CH)	no	in nearly all conditions
4	Portalet/Ravines Rousses (CH)	base of slope	only in very favorable conditions
5	Piz Scerscen II (CH)	within slope	in nearly all conditions
6	Piz Scerscen I (CH)	within slope	in nearly all conditions
7	Fluchthorn (AT/CH)	base of slope	in nearly all conditions
8	Piz Umur (CH)	base of slope	in nearly all conditions
9	Ritzlihorn/Mattenlimmi (CH)	no	mostly in cold conditions
10	Grosser Graben St. Niklaus (CH)	no	only in very favorable conditions
11	Vallon d'Etache (FR)	no	in nearly all conditions
12	Steingletscher II (CH)	recently deglaciated	no/unknown
13	Steingletscher I (CH)	recently deglaciated	no/unknown
14	Flüela Wisshorn (CH)	base of slope	in nearly all conditions
15	Cengalo VI (CH)	base of slope	mostly in cold conditions
16	Cengalo V (CH)	base of slope	mostly in cold conditions
17	Cengalo IV (CH)	base of slope	mostly in cold conditions
18	Trajo Glacier (IT)	base of slope	in nearly all conditions
19	Cengalo III (CH)	base of slope	mostly in cold conditions
20	Picola Croda Rossa (IT)	no	in nearly all conditions
21	Punta Tre Amici II (IT)	within slope	in nearly all conditions
22	Sölden/Schartlaskogel (AT)	no	mostly in cold conditions
23	Mulets de la Lia (CH)	no	in nearly all conditions
24	Piz Kesch (CH)	recently deglaciated	in nearly all conditions
25	Cengalo II (CH)	base of slope	in nearly all conditions
26	Crast'Agüzza (IT)	base of slope	mostly in cold conditions
27	Wasenhorn (CH)	base of slope	in nearly all conditions
28	Taschachtal (AT)	base of slope	no
29	Hochwand/Alpl (AT)	no	no
30	Cengalo I (CH)	base of slope	in nearly all conditions
31	Sass Maor (IT)	no	no
32	Birghorn (CH)	within slope	in nearly all conditions
33	Punta Tre Amici I (IT)	within slope	in nearly all conditions
34	Punta Thurwieser II (IT)	base of slope	in nearly all conditions
35	Mont Crammont (IT)	no	mostly in cold conditions
36	Punta Patri Nord (IT)	no	in nearly all conditions
37	Bliggspitze (AT)	within slope	in nearly all conditions
38	Monte Rosa II (IT)	within slope	in nearly all conditions
39	Dents Blanches (CH)	base of slope	in nearly all conditions
40	Dent du Midi (CH)	base of slope	in nearly all conditions
41	Cima Dodici (IT)	no	mostly in cold conditions
42	Drus (FR)	base of slope	in nearly all conditions
43	Punta Thurwieser I (IT)	base of slope	in nearly all conditions
44	Gruben (CH)	within slope	in nearly all conditions
45	Mättenberg/Ankenbaelli (CH)	no	mostly in cold conditions
46	Zuetribistock III (CH)	no	no

No	Name	Glacier	Permafrost
47	Brenva (FR)	within slope	in nearly all conditions
48	Zuetribistock II (CH)	no	no
49	Zuetribistock I (CH)	no	no
50	Miage III (IT)	base of slope	unknown
51	Randa (CH)	no	no
52	Piz Morteratsch/Tschierva (CH)	within slope	mostly in cold conditions
53	Miage II (IT)	within slope	in nearly all conditions
54	Val Pola (IT)	no	no
55	Fiernaz (IT)	no	no
56	Monte Rosa I (IT)	within slope	in nearly all conditions
57	Chli Spannort (CH)	base of slope	in nearly all conditions
58	Garde de Bordon II (CH)	no	in nearly all conditions
59	Feegletscher (CH)	base of slope	no
60	Becca de Luseney (IT)	no	in nearly all conditions
61	Garde de Bordon I (CH)	no	in nearly all conditions
62	Rawilhorn (CH)	no	no
63	Miage I (IT)	within slope	in nearly all conditions
64	Matterhorn (IT)	base of slope	in nearly all conditions
65	Piz Beverin (CH)	no	in nearly all conditions
66	Jungfrau (CH)	base of slope	in nearly all conditions
67	Chli Windgällen (CH)	no	unknown
68	Felikhorn (IT)	recently deglaciated	in nearly all conditions

Table 7: List of weather stations used in climatological analyses

Name	Elevation	Latitude	Longitude	Period	Variables
Jungfraujoch	3571	46.547556	7.985444	1933-2024	T, FTC
Col du Grand St-Bernard	2472	45.869092	7.170683	1865-2024	T, FTC, P
Weissfluhjoch	2691	46.833325	9.806394	1959-2024	T, FTC
Andermatt Gütsch	2286	46.652475	8.615531	1954-2024	T, FTC
Elm	958	46.923742	9.175347	1878-2024	P
Galtür	1587	46.96806	10.18556	1938-2025	P
Grimsel Hospiz	1980	46.571689	8.333256	1932-2024	P
Grächen	1605	46.195314	7.836822	1864-2024	P
Avrieux	1104	45.214	6.716833	1950-2025	P
Göschenen	950	46.692678	8.595364	1895-2024	P
Davos	1594	46.812969	9.843558	1867-2024	P
Altdorf	438	46.887069	8.621894	1864-2024	P
Cogne - Valnontey	1682	45.5855	7.33708	2001-2025	P
Toblach	1219	46.729978	12.219159	1981-2024	P
St. Leonhard im Pitztal	1454	47.02722	10.86556	1967-2025	P
Samedan	1709	46.526247	9.879469	1980-2024	P
Ehrwald	982	47.40417	10.92	1973-2025	P
Passo Rolle	2012	46.297919	11.787124	1991-2025	P
Adelboden	1321	46.491703	7.560703	1901-2024	P
Engelberg	1036	46.821639	8.410514	1864-2024	P
Sta. Maria, Val Müstair	1386	46.602256	10.426314	1900-2024	P
La Thuile - Les Granges	1637	45.7297	6.96684	1996-2025	P
Gets (Les)	1172	46.158667	6.670333	1948-2025	P
Sexten	1322	46.69154	12.357687	1981-2024	P
Chamonix	1042	45.9295	6.8775	1934-2025	P
Grindelwald	1107	46.619056	8.0067	1961-2024	P
Linthal/Tierfehd	810	46.879211	8.983717	1969-2024	P
Montana	1423	46.298806	7.460814	1931-2024	P

Name	Elevation	Latitude	Longitude	Period	Variables
Zermatt	1638	46.029272	7.752433	1892-2024	P
Arosa	1878	46.792661	9.679014	1900-2024	P
Lauterbrunnen	815	46.592917	7.906464	1899-2024	P
Simplon-Dorf	1465	46.196825	8.056336	1961-2024	P
Brusio	856	46.264358	10.117231	1900-2024	P
Kandersteg	1178	46.493842	7.677167	1899-2025	P

Table 8: List of documented large rock slope failures and the weather stations used for their climatological analyses

No	Name	Temperature station	Precipitation station
1	Kleines Nesthorn (CH)	Jungfraujoch	Kandersteg
2	Dent de Pro (CH)	Col du Grand St-Bernard	Col du Grand St-Bernard
3	Tschingelhorn (CH)	Weissfluhjoch	Elm
4	Portalet/Ravines Rousses (CH)	Col du Grand St-Bernard	Col du Grand St-Bernard
5	Piz Scerscen II (CH)	Weissfluhjoch	Piz Corvatsch
6	Piz Scerscen I (CH)	Weissfluhjoch	Piz Corvatsch
7	Fluchthorn (AT/CH)	Weissfluhjoch	Galtür
8	Piz Umur (CH)	Weissfluhjoch	Piz Corvatsch
9	Ritzlihorn/Mattenlimmi (CH)	Jungfraujoch	Grimsel Hospiz
10	Grosser Graben St. Niklaus (CH)	Jungfraujoch	Grächen
11	Vallon d'Etache (FR)	Col du Grand St-Bernard	Avrieux
12	Steingletscher II (CH)	Andermatt Gütsch	Göschenen
13	Steingletscher I (CH)	Andermatt Gütsch	Göschenen
14	Flüela Wisshorn (CH)	Weissfluhjoch	Davos
15	Cengalo VI (CH)	Weissfluhjoch	Piz Corvatsch
16	Cengalo V (CH)	Weissfluhjoch	Piz Corvatsch
17	Cengalo IV (CH)	Weissfluhjoch	Piz Corvatsch
18	Trajo Glacier (IT)	Col du Grand St-Bernard	Cogne - Valnontey
19	Cengalo III (CH)	Weissfluhjoch	Piz Corvatsch
20	Picola Croda Rossa (IT)	Weissfluhjoch	Toblach
21	Punta Tre Amici II (IT)	Jungfraujoch	Zermatt
22	Sölden/Schartlaskogel (AT)	Weissfluhjoch	St. Leonhard im Pitztal
23	Mulets de la Lia (CH)	Col du Grand St-Bernard	Col du Grand St-Bernard
24	Piz Kesch (CH)	Weissfluhjoch	Samedan
25	Cengalo II (CH)	Weissfluhjoch	Piz Corvatsch
26	Crast'Agüzza (IT)	Weissfluhjoch	Piz Corvatsch
27	Wasenhorn (CH)	Andermatt Gütsch	Engelberg
28	Taschachtal (AT)	Weissfluhjoch	St. Leonhard im Pitztal
29	Hochwand/Alpl (AT)	Weissfluhjoch	Ehrwald
30	Cengalo I (CH)	Weissfluhjoch	Piz Corvatsch
31	Sass Maor (IT)	Weissfluhjoch	Passo Rolle
32	Birghorn (CH)	Jungfraujoch	Adelboden
33	Punta Tre Amici I (IT)	Jungfraujoch	Zermatt
34	Punta Thurwieser II (IT)	Weissfluhjoch	Sta. Maria, Val Müstair
35	Mont Crammont (IT)	Col du Grand St-Bernard	La Thuile - Les Granges
36	Punta Patri Nord (IT)	Col du Grand St-Bernard	Cogne - Valnontey
37	Bliggspitze (AT)	Weissfluhjoch	St. Leonhard im Pitztal
38	Monte Rosa II (IT)	Jungfraujoch	Zermatt
39	Dents Blanches (CH)	Col du Grand St-Bernard	Gets (Les)
40	Dent du Midi (CH)	Col du Grand St-Bernard	Gets (Les)
41	Cima Dodici (IT)	Weissfluhjoch	Sexten
42	Drus (FR)	Col du Grand St-Bernard	Chamonix

No	Name	Temperature station	Precipitation station
43	Punta Thurwieser I (IT)	Weissfluhjoch	Sta. Maria, Val Müstair
44	Gruben (CH)	Jungfraujoch	Simplon-Dorf
45	Mättenberg/Ankenbaelli (CH)	Jungfraujoch	Grindelwald
46	Zuetribistock III (CH)	Andermatt Gütsch	Linthal/Tierfehd
47	Brenva (FR)	Col du Grand St-Bernard	La Thuile - Les Granges
48	Zuetribistock II (CH)	Andermatt Gütsch	Linthal/Tierfehd
49	Zuetribistock I (CH)	Andermatt Gütsch	Linthal/Tierfehd
50	Miage III (IT)	Col du Grand St-Bernard	Chamonix
51	Randa (CH)	Jungfraujoch	Grächen
52	Piz Morteratsch/Tschierva (CH)	Weissfluhjoch	Piz Corvatsch
53	Miage II (IT)	Col du Grand St-Bernard	Chamonix
54	Val Pola (IT)	Weissfluhjoch	Brusio
55	Fiernaz (IT)	Col du Grand St-Bernard	Zermatt
56	Monte Rosa I (IT)	Jungfraujoch	Zermatt
57	Chli Spannort (CH)	Andermatt Gütsch	Engelberg
58	Garde de Bordon II (CH)	Col du Grand St-Bernard	Grächen
59	Feegletscher (CH)	Jungfraujoch	Grächen
60	Becca de Luseney (IT)	Col du Grand St-Bernard	Col du Grand St-Bernard
61	Garde de Bordon I (CH)	Col du Grand St-Bernard	Grächen
62	Rawilhorn (CH)	Col du Grand St-Bernard	Montana
63	Miage I (IT)	Col du Grand St-Bernard	Chamonix
64	Matterhorn (IT)	Col du Grand St-Bernard	Zermatt
65	Piz Beverin (CH)	Jungfraujoch	Arosa
66	Jungfrau (CH)	Jungfraujoch	Lauterbrunnen
67	Chli Windgällen (CH)	Jungfraujoch	Altdorf
68	Felikhorn (IT)	Col du Grand St-Bernard	Zermatt

Table 9: List of documented large rock slope failures and the average mean temperatures [°C] and associated percentiles in the windows preceding failure. Variables in bold are above the 95th percentile. For extrapolated values the symbols ">"/"<" were used.

No	Name	Mean 1d	Mean 7d	Mean 30d	Mean 90d	Perc. 1d	Perc. 7d	Perc. 30d	Perc. 90d
1	Kleines Nesthorn (CH)	-	-	-	-	-	-	-	-
2	Dent de Pro (CH)	−1.09	−2.10	−3.27	−0.38	0.94	0.94	0.83	0.91
3	Tschingelhorn (CH)	−1.46	−0.43	0.84	6.25	0.24	0.24	0.18	>**0.99**
4	Portalet/Ravines Rousses (CH)	6.43	5.26	2.62	−1.17	0.74	0.78	0.72	0.81
5	Piz Scerscen II (CH)	0.21	−3.32	−7.66	−9.70	>**0.99**	>**0.99**	**0.99**	>**0.99**
6	Piz Scerscen I (CH)	−1.96	1.81	1.22	2.36	0.69	**0.99**	>**0.99**	>**0.99**
7	Fluchthorn (AT/CH)	0.67	−0.57	−2.46	−6.41	0.79	0.75	0.88	0.93
8	Piz Umur (CH)	−13.35	−13.67	−13.85	−10.16	0.44	0.31	0.21	0.82
9	Ritzlihorn/Mattenlimmi (CH)	1.78	−1.97	4.37	6.14	0.35	0.07	0.77	>**0.99**
10	Grosser Graben St. Niklaus (CH)	7.35	7.07	2.66	1.04	0.87	0.94	0.73	>**0.99**
11	Vallon d'Etache (FR)	−1.69	−1.49	−0.39	−2.86	0.25	0.29	0.69	**0.95**
12	Steingletscher II (CH)	−3.98	−3.84	−4.42	−4.06	0.89	**0.95**	**0.95**	**0.98**
13	Steingletscher I (CH)	−6.98	−7.20	−1.24	3.09	0.29	0.15	0.55	0.86
14	Flüela Wisshorn (CH)	−14.69	−9.16	−6.53	−9.42	0.12	0.58	**0.96**	0.82
15	Cengalo VI (CH)	−0.87	−0.40	3.18	4.73	0.26	0.23	0.74	>**0.99**
16	Cengalo V (CH)	3.90	3.45	4.63	4.41	0.66	0.63	0.80	>**0.99**
17	Cengalo IV (CH)	−0.65	5.75	5.92	5.42	0.15	0.77	0.84	>**0.99**
18	Trajo Glacier (IT)	1.93	4.49	3.65	−1.83	0.51	0.89	**0.97**	**0.97**
19	Cengalo III (CH)	5.93	4.24	5.68	4.24	0.86	0.86	**0.99**	>**0.99**

No	Name	Mean 1d	Mean 7d	Mean 30d	Mean 90d	Perc. 1d	Perc. 7d	Perc. 30d	Perc. 90d
20	Picola Croda Rossa (IT)	4.83	5.25	6.00	4.19	0.50	0.56	0.67	0.91
21	Punta Tre Amici II (IT)	−7.37	−6.87	−8.20	−4.96	0.80	0.89	0.86	0.94
22	Sölden/Schartlaskogel (AT)	−0.87	0.03	1.09	6.13	0.24	0.24	0.15	>**0.99**
23	Mulets de la Lia (CH)	−9.23	−5.84	−3.13	0.24	0.29	0.64	**0.99**	**0.95**
24	Piz Kesch (CH)	-	−8.98	−9.59	−8.47	-	0.73	0.80	0.91
25	Cengalo II (CH)	7.21	1.18	2.46	5.26	0.87	0.30	0.32	0.89
26	Crast'Agüzza (IT)	−13.05	−20.43	−19.31	−17.27	0.73	0.11	0.12	0.16
27	Wasenhorn (CH)	6.42	6.43	6.16	4.57	0.53	0.57	0.62	**0.99**
28	Taschachtal (AT)	1.39	3.20	1.50	−1.57	0.47	0.78	0.78	**0.99**
29	Hochwand/Alpl (AT)	−0.05	−0.77	−2.23	−6.14	0.88	0.91	**0.95**	0.53
30	Cengalo I (CH)	−5.87	−11.00	−9.35	−4.49	0.83	0.50	0.65	**0.99**
31	Sass Maor (IT)	−12.25	−6.17	−1.45	2.59	0.08	0.38	0.88	**0.99**
32	Birghorn (CH)	−2.55	−0.64	−1.85	1.58	0.82	**0.98**	0.89	>**0.99**
33	Punta Tre Amici I (IT)	−6.97	−0.32	−0.67	1.86	0.09	0.47	0.33	0.89
34	Punta Thurwieser II (IT)	−3.43	−5.59	−1.00	−0.22	0.31	0.08	0.49	0.94
35	Mont Crammont (IT)	−1.67	−5.14	−8.62	−3.77	0.87	0.74	0.21	0.25
36	Punta Patri Nord (IT)	0.25	−2.28	1.57	2.83	0.45	0.20	0.69	**0.95**
37	Bliggspitze (AT)	−2.75	−0.58	0.82	−1.46	0.21	0.43	0.94	>**0.99**
38	Monte Rosa II (IT)	−6.85	−8.01	−13.03	−14.08	**0.98**	**0.98**	0.89	0.91
39	Dents Blanches (CH)	4.53	−3.18	1.87	3.84	**0.98**	0.36	0.85	0.61
40	Dent du Midi (CH)	4.27	1.97	1.56	2.80	**0.96**	0.90	0.83	0.43
41	Cima Dodici (IT)	10.18	7.85	6.29	0.56	>**0.99**	**0.99**	>**0.99**	**0.99**
42	Drus (FR)	9.17	7.03	1.63	−3.58	>**0.99**	>**0.99**	**0.98**	0.93
43	Punta Thurwieser I (IT)	−1.23	−2.19	−0.44	−0.26	0.54	0.47	0.82	0.82
44	Gruben (CH)	-	-	-	-	-	-	-	-
45	Mättenberg/Ankenbaelli (CH)	−1.11	−1.01	4.15	2.86	0.17	0.10	0.87	0.53
46	Zuetribistock III (CH)	2.42	−2.33	−5.09	−3.95	**0.98**	0.81	0.70	0.92
47	Brenva (FR)	−12.80	−12.63	−16.27	−13.40	0.77	0.88	0.46	0.49
48	Zuetribistock II (CH)	−13.40	−6.74	−9.18	−5.97	0.09	0.45	0.16	0.54
49	Zuetribistock I (CH)	−4.98	−4.07	−4.31	−3.90	0.66	0.84	0.75	0.74
50	Miage III (IT)	-	-	−6.17	−7.24	-	-	<0.01	0.27
51	Randa (CH)	−8.37	−1.99	−1.88	−3.74	0.15	0.70	0.91	0.87
52	Piz Morteratsch/Tschierva (CH)	2.87	−0.88	−0.44	0.85	**0.97**	0.82	0.84	0.75
53	Miage II (IT)	-	-	−4.06	−8.55	-	-	0.62	0.47
54	Val Pola (IT)	1.93	4.94	8.11	2.92	0.09	0.21	0.74	0.18
55	Fiernaz (IT)	−1.47	−3.00	−4.75	−3.30	0.78	0.72	0.49	0.16
56	Monte Rosa I (IT)	-	-	-	-	-	-	-	-
57	Chli Spannort (CH)	−9.59	−9.03	−8.44	−5.50	0.46	0.58	0.62	0.52
58	Garde de Bordon II (CH)	6.33	3.42	1.40	−0.82	0.58	0.29	0.03	0.07
59	Feegletscher (CH)	2.25	2.73	5.24	0.66	0.15	0.13	0.65	0.34
60	Becca de Luseney (IT)	−0.29	1.19	−1.18	−4.49	0.48	0.76	0.68	0.89
61	Garde de Bordon I (CH)	−3.17	−0.34	−1.24	−0.89	0.02	0.01	<0.01	0.20
62	Rawilhorn (CH)	0.87	1.07	0.05	−2.11	0.39	0.41	0.51	0.91
63	Miage I (IT)	-	-	-	-	-	-	-	-
64	Matterhorn (IT)	−10.37	−4.40	−5.03	−7.30	0.02	0.33	0.37	0.86
65	Piz Beverin (CH)	−4.96	0.16	2.37	−2.18	0.01	0.12	0.49	0.20
66	Jungfrau (CH)	−5.93	−3.87	−5.46	−3.06	0.34	0.60	0.20	0.39
67	Chli Windgällen (CH)	6.83	4.18	4.15	3.00	0.70	0.36	0.39	0.74
68	Felikhorn (IT)	1.52	−3.12	−0.32	−3.05	0.43	0.02	0.16	0.14

Table 10: List of documented large rock slope failures and the average maximum air temperatures [°C] and associated percentiles in the windows preceding failure. Variables in bold are above the 95th percentile. For extrapolated values the symbols ">"/"<" were used.

No	Name	Mean 1d	Mean 7d	Mean 30d	Mean 90d	Perc. 1d	Perc. 7d	Perc. 30d	Perc. 90d
1	Kleines Nesthorn (CH)	-	-	-	-	-	-	-	-
2	Dent de Pro (CH)	2.81	0.18	−1.31	2.16	**0.98**	0.92	0.68	0.77
3	Tschingelhorn (CH)	2.15	2.42	4.00	10.06	0.30	0.26	0.20	>**0.99**
4	Portalet/Ravines Rousses (CH)	7.53	8.10	5.32	1.32	0.56	0.75	0.69	0.79
5	Piz Scerscen II (CH)	2.00	−0.45	−4.98	−7.33	>**0.99**	>**0.99**	**0.99**	**0.95**
6	Piz Scerscen I (CH)	2.04	5.58	5.06	6.20	0.76	**0.97**	**0.98**	>**0.99**
7	Fluchthorn (AT/CH)	3.57	2.34	0.04	−3.97	0.76	0.73	0.70	0.79
8	Piz Umur (CH)	−11.75	−10.98	−11.27	−7.74	0.26	0.23	0.13	0.59
9	Ritzlihorn/Mattenlimmi (CH)	3.38	0.88	6.71	8.41	0.32	0.08	0.73	**0.99**
10	Grosser Graben St. Niklaus (CH)	10.05	9.60	5.30	3.62	0.90	**0.96**	0.78	**0.97**
11	Vallon d'Etache (FR)	0.81	0.85	2.49	−0.18	0.25	0.25	0.69	**0.95**
12	Steingletscher II (CH)	−0.68	−0.78	−1.73	−1.64	0.88	**0.95**	0.94	0.94
13	Steingletscher I (CH)	−5.78	−5.70	0.83	6.40	0.20	0.10	0.36	0.74
14	Flüela Wisshorn (CH)	−13.39	−5.24	−3.74	−6.65	0.05	0.70	**0.95**	0.79
15	Cengalo VI (CH)	3.63	2.98	6.87	8.67	0.35	0.23	0.62	>**0.99**
16	Cengalo V (CH)	7.70	7.05	8.58	8.30	0.60	0.51	0.73	>**0.99**
17	Cengalo IV (CH)	1.95	9.56	9.95	9.27	0.15	0.58	0.76	>**0.99**
18	Trajo Glacier (IT)	5.73	8.03	7.20	1.45	0.50	0.89	**0.98**	**0.98**
19	Cengalo III (CH)	11.23	8.54	9.78	8.01	0.91	0.92	>**0.99**	**0.95**
20	Picola Croda Rossa (IT)	7.63	9.04	9.80	7.56	0.38	0.46	0.62	0.84
21	Punta Tre Amici II (IT)	−5.47	−4.63	−5.37	−2.08	0.73	0.88	0.91	**0.99**
22	Sölden/Schartlaskogel (AT)	4.03	4.93	4.80	10.50	0.36	0.42	0.22	>**0.99**
23	Mulets de la Lia (CH)	−7.83	−4.29	−1.70	2.36	0.19	0.54	0.93	0.83
24	Piz Kesch (CH)	-	−6.64	−7.27	−6.00	-	0.61	0.68	0.80
25	Cengalo II (CH)	12.21	4.26	5.64	9.12	0.86	0.31	0.22	0.81
26	Crast'Agüzza (IT)	−10.65	−17.87	−16.96	−14.73	0.70	0.10	0.01	0.02
27	Wasenhorn (CH)	10.42	10.16	10.10	8.21	0.52	0.55	0.65	0.93
28	Taschachtal (AT)	2.69	5.79	4.22	1.02	0.30	0.70	0.71	>**0.99**
29	Hochwand/Alpl (AT)	2.55	1.26	0.60	−3.25	0.81	0.80	0.94	0.44
30	Cengalo I (CH)	−0.87	−6.70	−6.38	−1.46	0.90	0.55	0.59	0.94
31	Sass Maor (IT)	−11.35	−3.91	1.31	5.57	0.02	0.22	0.83	0.94
32	Birghorn (CH)	1.05	2.86	0.89	4.49	0.90	>**0.99**	**0.97**	>**0.99**
33	Punta Tre Amici I (IT)	−6.07	2.93	2.14	4.99	0.04	0.64	0.44	**0.98**
34	Punta Thurwieser II (IT)	−1.93	−2.78	2.53	3.35	0.20	0.04	0.35	0.86
35	Mont Crammont (IT)	0.23	−1.48	−6.01	−1.16	0.83	0.78	0.21	0.25
36	Punta Patri Nord (IT)	2.95	0.51	4.60	6.29	0.45	0.20	0.68	**0.99**
37	Bliggspitze (AT)	2.45	3.79	4.62	1.83	0.44	0.65	**0.99**	>**0.99**
38	Monte Rosa II (IT)	−1.25	−4.33	−9.77	−10.92	>**0.99**	**0.98**	0.94	**0.96**
39	Dents Blanches (CH)	7.63	−0.13	4.51	6.57	**0.98**	0.43	0.85	0.55
40	Dent du Midi (CH)	6.57	4.12	4.07	5.50	**0.95**	0.86	0.81	0.37
41	Cima Dodici (IT)	14.98	12.61	10.52	3.71	**0.97**	**0.98**	>**0.99**	**0.98**
42	Drus (FR)	12.67	10.61	4.93	−0.78	>**0.99**	>**0.99**	**0.98**	0.94
43	Punta Thurwieser I (IT)	4.67	1.24	3.45	3.41	0.69	0.43	0.82	0.70
44	Gruben (CH)	-	-	-	-	-	-	-	-
45	Mättenberg/Ankenbaelli (CH)	4.59	1.59	7.06	5.77	0.49	0.12	0.92	0.79
46	Zuetribistock III (CH)	5.62	0.66	−2.22	−1.35	**0.99**	0.81	0.66	0.92
47	Brenva (FR)	−11.30	−10.09	−14.27	−10.92	0.69	0.87	0.40	0.47
48	Zuetribistock II (CH)	−11.38	−4.60	−6.52	−3.73	0.07	0.40	0.15	0.40
49	Zuetribistock I (CH)	−3.48	−2.11	−2.45	−1.54	0.55	0.75	0.66	0.55

No	Name	Mean 1d	Mean 7d	Mean 30d	Mean 90d	Perc. 1d	Perc. 7d	Perc. 30d	Perc. 90d
50	Miage III (IT)	-	-	-3.68	-4.85	-	-	<0.01	0.26
51	Randa (CH)	0.53	3.25	1.72	-0.17	0.59	0.93	**0.96**	**0.96**
52	Piz Morteratsch/Tschierva (CH)	6.77	3.12	3.37	4.92	**0.96**	0.83	0.85	0.75
53	Miage II (IT)	-	-	-1.90	-6.26	-	-	0.54	0.44
54	Val Pola (IT)	6.03	9.03	11.64	5.67	0.18	0.30	0.74	0.17
55	Fiernaz (IT)	0.23	-1.08	-2.27	-0.58	0.72	0.67	0.50	0.23
56	Monte Rosa I (IT)	-	-	-	-	-	-	-	-
57	Chli Spannort (CH)	-6.19	-5.77	-5.45	-2.57	0.53	0.64	0.63	0.47
58	Garde de Bordon II (CH)	-	-	-	-	-	-	-	-
59	Feegletscher (CH)	-	-	-	-	-	-	-	-
60	Becca de Luseney (IT)	-	-	-	-	-	-	-	-
61	Garde de Bordon I (CH)	-	-	-	-	-	-	-	-
62	Rawilhorn (CH)	-	-	-	-	-	-	-	-
63	Miage I (IT)	-	-	-	-	-	-	-	-
64	Matterhorn (IT)	-	-	-	-	-	-	-	-
65	Piz Beverin (CH)	-	-	-	-	-	-	-	-
66	Jungfrau (CH)	-	-	-	-	-	-	-	-
67	Chli Windgällen (CH)	-	-	-	-	-	-	-	-
68	Felikhorn (IT)	-	-	-	-	-	-	-	-

Table 11: List of documented large rock slope failures and their number of extremely warm days (mean/max. temperature) in the windows preceding failures. Variables in bold are above the defined threshold.

No	Name	Mean 1d	Mean 7d	Mean 30d	Mean 90d	Max. 1d	Max. 7d	Max. 30d	Max. 90d
1	Kleines Nesthorn (CH)	-	-	-	-	-	-	-	-
2	Dent de Pro (CH)	0	0	0	**11**	**1**	1	1	**14**
3	Tschingelhorn (CH)	0	0	0	**24**	0	0	0	**15**
4	Portalet/Ravines Rousses (CH)	0	0	0	**9**	0	0	0	**9**
5	Piz Scerscen II (CH)	**1**	**5**	**9**	**22**	**1**	**6**	**10**	**17**
6	Piz Scerscen I (CH)	0	**3**	**8**	**29**	0	**2**	**5**	**27**
7	Fluchthorn (AT/CH)	0	0	0	5	0	0	0	6
8	Piz Umur (CH)	0	0	0	8	0	0	0	6
9	Ritzlihorn/Mattenlimmi (CH)	0	0	**6**	**19**	0	0	**5**	**10**
10	Grosser Graben St. Niklaus (CH)	0	1	1	**14**	0	1	1	**12**
11	Vallon d'Etache (FR)	0	0	2	**9**	0	0	3	**14**
12	Steingletscher II (CH)	0	**3**	**8**	**14**	0	**3**	**5**	**11**
13	Steingletscher I (CH)	0	0	1	**9**	0	0	1	8
14	Flüela Wisshorn (CH)	0	0	**7**	**10**	0	**2**	**9**	**11**
15	Cengalo VI (CH)	0	0	**6**	**19**	0	0	**5**	**20**
16	Cengalo V (CH)	0	0	**4**	**25**	0	0	**4**	**24**
17	Cengalo IV (CH)	0	0	**4**	**25**	0	0	**4**	**24**
18	Trajo Glacier (IT)	0	**2**	**11**	**22**	0	**2**	**12**	**25**
19	Cengalo III (CH)	0	0	**6**	**12**	0	1	**6**	**11**
20	Picola Croda Rossa (IT)	0	0	1	8	0	0	0	5
21	Punta Tre Amici II (IT)	0	0	2	**11**	0	0	**4**	**15**
22	Sölden/Schartlaskogel (AT)	0	0	0	**22**	0	0	0	**22**
23	Mulets de la Lia (CH)	0	0	**4**	7	0	0	2	5
24	Piz Kesch (CH)	-	0	2	6	-	0	2	6
25	Cengalo II (CH)	0	0	2	**11**	0	0	**4**	**12**
26	Crast'Agüzza (IT)	0	0	1	4	0	0	1	2

No	Name	Mean 1d	Mean 7d	Mean 30d	Mean 90d	Max. 1d	Max. 7d	Max. 30d	Max. 90d
27	Wasenhorn (CH)	0	0	1	**11**	0	0	1	**10**
28	Taschachtal (AT)	0	0	2	**10**	0	0	3	**9**
29	Hochwand/Alpl (AT)	0	**2**	**6**	8	0	**2**	**4**	5
30	Cengalo I (CH)	0	0	1	7	0	0	1	5
31	Sass Maor (IT)	0	0	1	7	0	0	1	5
32	Birghorn (CH)	0	**3**	3	**14**	0	**4**	**5**	**23**
33	Punta Tre Amici I (IT)	0	0	0	**16**	0	**2**	3	**25**
34	Punta Thurwieser II (IT)	0	0	3	**16**	0	0	2	**14**
35	Mont Crammont (IT)	0	0	0	1	0	0	0	2
36	Punta Patri Nord (IT)	0	0	2	8	0	0	**4**	**12**
37	Bliggspitze (AT)	0	0	2	**23**	0	1	**5**	**30**
38	Monte Rosa II (IT)	**1**	**4**	**6**	**12**	**1**	**4**	**8**	**16**
39	Dents Blanches (CH)	**1**	1	3	6	**1**	1	2	5
40	Dent du Midi (CH)	**1**	**2**	2	5	0	1	1	4
41	Cima Dodici (IT)	**1**	**2**	**9**	**14**	**1**	**2**	**10**	**15**
42	Drus (FR)	**1**	**6**	**10**	**20**	**1**	**6**	**11**	**23**
43	Punta Thurwieser I (IT)	0	0	0	1	0	0	2	3
44	Gruben (CH)	-	-	-	-	-	-	-	-
45	Mättenberg/Ankenbaelli (CH)	0	0	3	7	0	0	**8**	**16**
46	Zuetribistock III (CH)	**1**	**3**	3	**21**	**1**	**3**	**4**	**19**
47	Brenva (FR)	0	0	0	2	0	1	1	2
48	Zuetribistock II (CH)	0	0	0	0	0	0	0	0
49	Zuetribistock I (CH)	0	0	0	0	0	0	0	0
50	Miage III (IT)	-	-	0	1	-	-	0	0
51	Randa (CH)	0	0	3	**12**	0	1	**7**	**24**
52	Piz Morteratsch/Tschierva (CH)	**1**	**2**	**5**	6	**1**	**2**	**4**	4
53	Miage II (IT)	-	-	0	1	-	-	0	1
54	Val Pola (IT)	0	0	1	3	0	0	0	1
55	Fiernaz (IT)	0	0	1	4	0	0	2	3
56	Monte Rosa I (IT)	-	-	-	-	-	-	-	-
57	Chli Spannort (CH)	0	0	1	1	0	0	1	2
58	Garde de Bordon II (CH)	0	0	0	0	-	-	-	-
59	Feegletscher (CH)	0	0	0	0	-	-	-	-
60	Becca de Luseney (IT)	0	0	0	4	-	-	-	-
61	Garde de Bordon I (CH)	0	0	0	0	-	-	-	-
62	Rawilhorn (CH)	0	0	0	2	-	-	-	-
63	Miage I (IT)	-	-	-	-	-	-	-	-
64	Matterhorn (IT)	0	0	0	7	-	-	-	-
65	Piz Beverin (CH)	0	0	1	3	-	-	-	-
66	Jungfrau (CH)	0	0	0	1	-	-	-	-
67	Chli Windgällen (CH)	0	0	0	2	-	-	-	-
68	Felikhorn (IT)	0	0	0	0	-	-	-	-

Table 12: List of documented large rock slope failures and the absolute FTC count and associated percentiles in the windows preceding failure. Variables in bold are above the 95th percentile. For extrapolated values the symbols ”>”/”<” were used

No	Name	FTC 1d	FTC 7d	FTC 30d	FTC 90d	Perc. 7d	Perc. 30d	Perc. 90d
1	Kleines Nesthorn (CH)	-	-	-	-	-	-	-
2	Dent de Pro (CH)	1	5	10	22	**0.98**	0.69	0.16
3	Tschingelhorn (CH)	1	4	14	14	0.88	**0.95**	0.36

No	Name	FTC 1d	FTC 7d	FTC 30d	FTC 90d	Perc. 7d	Perc. 30d	Perc. 90d
4	Portalet/Ravines Rousses (CH)	0	1	14	33	0.42	0.69	0.72
5	Piz Scerscen II (CH)	1	3	4	4	>**0.99**	>**0.99**	>**0.99**
6	Piz Scerscen I (CH)	1	3	17	32	0.74	0.77	0.34
7	Fluchthorn (AT/CH)	1	6	19	25	**0.97**	**0.98**	**0.96**
8	Piz Umur (CH)	0	0	0	4	0.50	0.50	0.70
9	Ritzlihorn/Mattenlimmi (CH)	1	2	6	11	0.66	0.34	0.01
10	Grosser Graben St. Niklaus (CH)	0	0	14	54	0.50	0.67	>**0.99**
11	Vallon d'Etache (FR)	1	5	22	47	0.87	0.93	>**0.99**
12	Steingletscher II (CH)	0	4	13	34	**0.97**	**0.96**	**0.96**
13	Steingletscher I (CH)	0	0	5	23	0.50	0.06	0.17
14	Flüela Wisshorn (CH)	0	1	7	9	0.94	**0.97**	**0.96**
15	Cengalo VI (CH)	1	5	12	27	**0.96**	0.71	0.48
16	Cengalo V (CH)	0	3	10	29	0.85	0.74	0.38
17	Cengalo IV (CH)	1	2	6	23	0.76	0.63	0.39
18	Trajo Glacier (IT)	1	3	10	27	0.55	0.22	0.40
19	Cengalo III (CH)	0	3	6	25	0.67	0.37	0.39
20	Picola Croda Rossa (IT)	0	2	5	33	0.87	0.61	0.72
21	Punta Tre Amici II (IT)	0	0	1	22	0.50	0.75	0.86
22	Sölden/Schartlaskogel (AT)	1	7	19	21	>**0.99**	>**0.99**	0.57
23	Mulets de la Lia (CH)	0	0	5	27	0.50	0.55	0.60
24	Piz Kesch (CH)	-	0	1	6	0.50	0.87	0.72
25	Cengalo II (CH)	0	4	13	18	**0.95**	0.94	0.46
26	Crast'Agüzza (IT)	0	0	0	0	0.50	0.50	0.50
27	Wasenhorn (CH)	0	0	6	24	0.50	0.52	0.09
28	Taschachtal (AT)	0	1	13	32	0.48	0.62	0.67
29	Hochwand/Alpl (AT)	1	4	15	25	0.87	0.94	0.84
30	Cengalo I (CH)	0	0	2	25	0.50	0.80	0.79
31	Sass Maor (IT)	0	2	15	29	0.72	0.86	0.65
32	Birghorn (CH)	1	6	17	33	>**0.99**	>**0.99**	0.54
33	Punta Tre Amici I (IT)	0	3	19	39	0.65	0.88	0.64
34	Punta Thurwieser II (IT)	0	2	15	41	0.43	0.46	0.41
35	Mont Crammont (IT)	1	3	3	27	0.90	0.44	0.75
36	Punta Patri Nord (IT)	1	2	15	36	0.40	0.55	0.32
37	Bliggspitze (AT)	1	6	16	41	**0.98**	0.76	**0.96**
38	Monte Rosa II (IT)	0	0	0	0	0.50	0.50	0.50
39	Dents Blanches (CH)	0	3	10	25	0.73	0.47	0.72
40	Dent du Midi (CH)	0	5	13	34	0.92	0.71	0.94
41	Cima Dodici (IT)	0	0	1	21	0.50	0.33	0.33
42	Drus (FR)	0	0	13	24	0.50	0.37	0.56
43	Punta Thurwieser I (IT)	1	4	21	54	0.74	**0.97**	0.93
44	Gruben (CH)	-	-	-	-	-	-	-
45	Mättenberg/Ankenbaelli (CH)	1	4	7	31	0.90	0.25	0.66
46	Zuetribistock III (CH)	0	2	9	21	0.64	0.73	0.73
47	Brenva (FR)	0	0	0	2	0.50	0.50	0.88
48	Zuetribistock II (CH)	0	0	0	14	0.50	0.50	0.20
49	Zuetribistock I (CH)	0	1	5	21	0.72	0.61	0.35
50	Miage III (IT)	-	-	6	7	-	0.24	0.20
51	Randa (CH)	1	7	19	48	>**0.99**	>**0.99**	>**0.99**
52	Piz Morteratsch/Tschierva (CH)	1	4	17	41	0.82	0.78	0.69
53	Miage II (IT)	-	-	6	6	-	0.50	0.43
54	Val Pola (IT)	1	2	2	32	0.93	0.58	0.79
55	Fiernaz (IT)	1	2	9	20	0.70	0.70	0.35
56	Monte Rosa I (IT)	-	-	-	-	-	-	-
57	Chli Spannort (CH)	0	0	2	15	0.50	0.58	0.15

No	Name	FTC 1d	FTC 7d	FTC 30d	FTC 90d	Perc. 7d	Perc. 30d	Perc. 90d
58	Garde de Bordon II (CH)	-	-	-	-	-	-	-
59	Feegletscher (CH)	-	-	-	-	-	-	-
60	Becca de Luseney (IT)	-	-	-	-	-	-	-
61	Garde de Bordon I (CH)	-	-	-	-	-	-	-
62	Rawilhorn (CH)	-	-	-	-	-	-	-
63	Miage I (IT)	-	-	-	-	-	-	-
64	Matterhorn (IT)	-	-	-	-	-	-	-
65	Piz Beverin (CH)	-	-	-	-	-	-	-
66	Jungfrau (CH)	-	-	-	-	-	-	-
67	Chli Windgällen (CH)	-	-	-	-	-	-	-
68	Felikhorn (IT)	-	-	-	-	-	-	-

Table 13: List of documented large rock slope failures and the precipitation [mm] and associated percentiles in the windows preceding failure. Variables in bold are above the 95th percentile. For extrapolated values the symbols ">"/"<" were used

No	Name	Sum 1d	Sum 7d	Sum 30d	Sum 90d	Perc. 1d	Perc. 7d	Perc. 30d	Perc. 90d
1	Kleines Nesthorn (CH)	-	-	-	-	-	-	-	-
2	Dent de Pro (CH)	0.0	28.1	203.7	514.2	-	0.50	0.67	0.71
3	Tschingelhorn (CH)	0.4	54.9	200.1	394.9	0.60	0.82	0.81	0.24
4	Portalet/Ravines Rousses (CH)	37.1	94.6	156.9	701.9	**0.99**	**0.96**	0.64	0.91
5	Piz Scerscen II (CH)	0.0	51.7	249.4	496.5	-	0.93	**0.99**	**0.98**
6	Piz Scerscen I (CH)	0.0	0.0	92.6	353.0	-	-	0.55	0.75
7	Fluchthorn (AT/CH)	0.3	7.1	46.4	238.6	0.46	0.16	0.13	0.70
8	Piz Umur (CH)	0.0	5.5	15.5	121.0	-	0.49	0.15	0.28
9	Ritzlihorn/Mattenlimmi (CH)	6.7	79.1	96.7	340.5	0.79	0.90	0.29	0.27
10	Grosser Graben St. Niklaus (CH)	6.6	13.7	105.4	178.6	0.91	0.67	0.94	0.74
11	Vallon d'Etache (FR)	0.1	43.7	84.6	196.9	0.67	**0.98**	0.91	0.90
12	Steingletscher II (CH)	0.0	9.9	125.2	303.0	-	0.40	0.68	0.47
13	Steingletscher I (CH)	5.0	44.5	166.6	448.9	0.79	0.78	0.77	0.82
14	Flüela Wisshorn (CH)	0.9	55.3	92.9	371.4	0.71	**0.97**	0.84	**0.97**
15	Cengalo VI (CH)	6.3	81.8	201.0	454.1	0.85	**0.97**	**0.97**	**0.98**
16	Cengalo V (CH)	0.0	26.5	116.5	372.0	-	0.67	0.65	0.78
17	Cengalo IV (CH)	0.0	26.5	125.0	372.1	-	0.66	0.71	0.78
18	Trajo Glacier (IT)	0.0	18.0	58.8	147.6	-	0.70	0.47	0.25
19	Cengalo III (CH)	10.1	14.1	58.1	372.1	0.90	0.48	0.23	0.80
20	Picola Croda Rossa (IT)	0.0	20.5	176.9	447.9	-	0.50	0.93	**0.97**
21	Punta Tre Amici II (IT)	2.1	2.4	36.3	105.8	0.83	0.38	0.42	0.22
22	Sölden/Schartlaskogel (AT)	0.0	0.2	72.9	299.1	-	0.13	0.40	0.33
23	Mulets de la Lia (CH)	10.2	13.4	282.7	692.7	0.81	0.33	0.84	0.83
24	Piz Kesch (CH)	-	23.3	90.7	170.4	-	0.94	**0.98**	0.87
25	Cengalo II (CH)	0.0	2.6	91.5	254.2	-	0.21	0.48	0.26
26	Crast'Agüzza (IT)	0.0	12.9	39.6	175.5	-	0.68	0.43	0.63
27	Wasenhorn (CH)	0.0	25.9	131.4	523.3	-	0.32	0.18	0.48
28	Taschachtal (AT)	0.2	22.9	47.5	109.2	0.49	0.60	0.20	0.12
29	Hochwand/Alpl (AT)	0.0	9.5	28.4	245.4	-	0.42	0.14	0.64
30	Cengalo I (CH)	0.0	23.0	60.7	236.7	-	0.82	0.60	0.54
31	Sass Maor (IT)	0.2	3.6	10.6	299.0	0.69	0.49	0.13	0.28
32	Birghorn (CH)	0.0	0.0	11.6	244.8	-	-	0.03	0.30
33	Punta Tre Amici I (IT)	0.0	8.8	27.3	169.5	-	0.54	0.18	0.46
34	Punta Thurwieser II (IT)	0.4	10.8	109.9	252.2	0.67	0.45	0.72	0.47

No	Name	Sum 1d	Sum 7d	Sum 30d	Sum 90d	Perc. 1d	Perc. 7d	Perc. 30d	Perc. 90d
35	Mont Crammont (IT)	0.0	3.8	96.2	342.8	-	0.38	0.70	0.75
36	Punta Patri Nord (IT)	0.0	19.8	66.6	218.0	-	0.78	0.71	0.70
37	Bliggspitze (AT)	0.0	29.5	100.3	237.9	-	0.58	0.41	0.44
38	Monte Rosa II (IT)	0.0	0.0	16.5	82.7	-	-	0.15	0.20
39	Dents Blanches (CH)	0.1	0.7	55.2	426.4	0.51	0.15	0.12	0.56
40	Dent du Midi (CH)	0.1	46.0	131.5	493.4	0.52	0.73	0.55	0.73
41	Cima Dodici (IT)	0.0	0.4	72.0	251.0	-	0.04	0.14	0.27
42	Drus (FR)	1.0	32.6	126.6	322.2	0.61	0.63	0.60	0.60
43	Punta Thurwieser I (IT)	0.0	47.1	88.3	283.1	-	0.89	0.57	0.62
44	Gruben (CH)	-	-	-	-	-	-	-	-
45	Mättenberg/Ankenbaelli (CH)	3.9	26.0	98.7	514.6	0.74	0.54	0.27	0.84
46	Zuetribistock III (CH)	0.0	0.1	138.1	259.6	-	0.07	0.60	0.15
47	Brenva (FR)	0.0	0.0	63.2	289.2	-	-	0.53	0.72
48	Zuetribistock II (CH)	0.1	3.8	98.2	241.1	0.51	0.19	0.41	0.11
49	Zuetribistock I (CH)	0.0	0.0	84.3	296.6	-	-	0.30	0.23
50	Miage III (IT)	-	-	55.3	169.6	-	-	0.12	0.11
51	Randa (CH)	2.1	2.3	48.4	122.3	0.85	0.41	0.69	0.65
52	Piz Morteratsch/Tschierva (CH)	0.0	0.0	154.7	348.3	-	-	0.84	0.72
53	Miage II (IT)	-	-	76.2	329.5	-	-	0.29	0.76
54	Val Pola (IT)	0.0	15.0	271.0	545.9	-	0.42	>**0.99**	>**0.99**
55	Fiernaz (IT)	0.0	0.1	87.6	235.8	-	0.23	0.86	0.81
56	Monte Rosa I (IT)	-	-	-	-	-	-	-	-
57	Chli Spannort (CH)	0.0	1.4	155.3	278.5	-	0.18	0.85	0.38
58	Garde de Bordon II (CH)	0.0	1.6	29.0	111.5	-	0.20	0.21	0.23
59	Feegletscher (CH)	0.0	21.6	66.0	130.5	0.34	0.83	0.74	0.41
60	Becca de Luseney (IT)	20.1	48.9	96.6	485.0	0.93	0.76	0.21	0.54
61	Garde de Bordon I (CH)	0.1	12.5	62.3	140.4	0.70	0.65	0.71	0.47
62	Rawilhorn (CH)	0.0	22.1	76.2	128.5	-	0.73	0.68	0.18
63	Miage I (IT)	-	-	-	-	-	-	-	-
64	Matterhorn (IT)	3.0	13.3	64.0	121.2	0.81	0.59	0.58	0.11
65	Piz Beverin (CH)	0.6	9.7	168.1	375.9	0.49	0.15	0.65	0.54
66	Jungfrau (CH)	7.9	26.7	116.4	411.1	0.88	0.72	0.74	0.80
67	Chli Windgällen (CH)	0.0	22.3	195.6	470.8	-	0.39	0.86	0.80
68	Felikhorn (IT)	0.0	28.7	90.7	231.3	-	0.86	0.83	0.77

Table 14: List of documented large rock slope failures and number of days with heavy rainfall in the windows preceding failure. Variables in bold are above the defined threshold.

No	Name	Count 1d	Count 7d	Count 30d	Count 90d
1	Kleines Nesthorn (CH)	-	-	-	-
2	Dent de Pro (CH)	0	1	3	**9**
3	Tschingelhorn (CH)	0	0	3	3
4	Portalet/Ravines Rousses (CH)	**1**	**2**	2	**9**
5	Piz Scerscen II (CH)	0	1	**4**	5
6	Piz Scerscen I (CH)	0	0	2	5
7	Fluchthorn (AT/CH)	0	0	0	1
8	Piz Umur (CH)	0	0	0	0
9	Ritzlihorn/Mattenlimmi (CH)	0	1	1	3
10	Grosser Graben St. Niklaus (CH)	0	0	0	0
11	Vallon d'Etache (FR)	0	1	1	2
12	Steingletscher II (CH)	0	0	1	3
13	Steingletscher I (CH)	0	1	2	5

No	Name	Count 1d	Count 7d	Count 30d	Count 90d
14	Flüela Wisshorn (CH)	0	0	0	3
15	Cengalo VI (CH)	0	1	3	5
16	Cengalo V (CH)	0	0	0	4
17	Cengalo IV (CH)	0	0	0	4
18	Trajo Glacier (IT)	0	0	0	0
19	Cengalo III (CH)	0	0	0	3
20	Picola Croda Rossa (IT)	0	0	2	3
21	Punta Tre Amici II (IT)	0	0	1	1
22	Sölden/Schartlaskogel (AT)	0	0	0	0
23	Mulets de la Lia (CH)	0	0	**5**	**9**
24	Piz Kesch (CH)	-	0	0	1
25	Cengalo II (CH)	0	0	1	3
26	Crast'Agüzza (IT)	0	0	0	0
27	Wasenhorn (CH)	0	0	0	3
28	Taschachtal (AT)	0	0	0	0
29	Hochwand/Alpl (AT)	0	0	0	1
30	Cengalo I (CH)	0	0	0	2
31	Sass Maor (IT)	0	0	0	4
32	Birghorn (CH)	0	0	0	4
33	Punta Tre Amici I (IT)	0	0	0	1
34	Punta Thurwieser II (IT)	0	0	0	1
35	Mont Crammont (IT)	0	0	0	3
36	Punta Patri Nord (IT)	0	0	0	0
37	Bliggspitze (AT)	0	0	0	0
38	Monte Rosa II (IT)	0	0	0	0
39	Dents Blanches (CH)	0	0	1	6
40	Dent du Midi (CH)	0	1	3	7
41	Cima Dodici (IT)	0	0	0	1
42	Drus (FR)	0	0	1	2
43	Punta Thurwieser I (IT)	0	1	1	3
44	Gruben (CH)	-	-	-	-
45	Mättenberg/Ankenbaelli (CH)	0	0	1	4
46	Zuetribistock III (CH)	0	0	0	1
47	Brenva (FR)	0	0	0	2
48	Zuetribistock II (CH)	0	0	0	2
49	Zuetribistock I (CH)	0	0	1	4
50	Miage III (IT)	-	-	0	0
51	Randa (CH)	0	0	0	1
52	Piz Morteratsch/Tschierva (CH)	0	0	2	6
53	Miage II (IT)	-	-	0	0
54	Val Pola (IT)	0	0	3	5
55	Fiernaz (IT)	0	0	1	1
56	Monte Rosa I (IT)	-	-	-	-
57	Chli Spannort (CH)	0	0	1	1
58	Garde de Bordon II (CH)	0	0	0	0
59	Feegletscher (CH)	0	0	0	0
60	Becca de Luseney (IT)	0	0	1	4
61	Garde de Bordon I (CH)	0	0	0	0
62	Rawilhorn (CH)	0	0	0	0
63	Miage I (IT)	-	-	-	-
64	Matterhorn (IT)	0	0	0	0
65	Piz Beverin (CH)	0	0	2	4
66	Jungfrau (CH)	0	0	0	1
67	Chli Windgällen (CH)	0	0	1	1

No	Name	Count 1d	Count 7d	Count 30d	Count 90d
68	Felikhorn (IT)	0	0	0	0

Declaration of the usage of AI: I hereby declare that I have composed this work with the use of artificial intelligence, namely ChatGPT-5. Its use was limited to: code generation, in particular to assist with data analysis and plot creation, paraphrasing and linguistic revision of own phrasing, and grammatical correction of texts to improve readability and precision.

Personal declaration: I hereby declare that the material contained in this thesis is my own original work. Any quotation or paraphrase in this thesis from the published or unpublished work of another individual or institution has been duly acknowledged. I have not submitted this thesis, or any part of it, previously to any institution for assessment purposes.

Zürich, 16.03.2026